Using Stokes flow equations for the geomechanical restoration of geological structural models

Melchior Schuh-Senlis

Using Stokes flow equations for the geomechanical restoration of geological structural models

ou

Applicabilité des équations de Stokes pour la gestion des grandes déformations en restauration de modèles géologiques

THÈSE

présentée en vue de l'obtention du grade de

Docteur de l'Université de Lorraine

Spécialité Géosciences

par

Melchior Schuh-Senlis

et soutenue le 23/03/2021

Composition du jury:

Rapporteurs:	Prof. Laetitia Le Pourhiet	ISTeP, France
	Prof. John H. Shaw	Harvard University, USA
Examinateurs:	Prof. Susanne Buiter	RWTH Aachen University, Germany
	Dr. Fanny Garel	Université de Montpellier, France
Directeur de thèse:	Prof. Guillaume Caumon	Université de Lorraine, France
Co-directeur de thèse:	Dr. Paul Cupillard	Université de Lorraine, France
Invité:	Dr. Cedric Thieulot	Utrecht University, Netherlands

GeoRessources - UMR 7359
Université de Lorraine – CNRS
École Nationale Supérieure de Géologie
2 rue du Doyen Marcel Roubault - BP 10162
54505 Vandœuvre-lès-Nancy, FRANCE

Contents

List of Figures

List of Tables

Remerciements

Je tiens en premier lieu à remercier ma famille, à laquelle je dédie cette thèse, et sans laquelle je ne serais jamais arrivé où je suis actuellement: mes parents et grand-parents qui m'ont élevé, soutenu et conseillé au cours de mes études et dans tous mes projets; mes trois soeurs avec lesquelles j'ai grandi aussi bien en age qu'en maturité et en sens critique, et sur lesquelles j'ai toujours pu compter; ma marraine et mes oncles et cousins, également, qui m'ont apporté des points de vue différents et de l'aide sur de nombreux aspects de ma vie.

Je tiens également à remercier mes amis et collègues (qui souvent sont les deux): Bastien et Yann et leur présence (souvent immatérielle vu la distance) tout au long de Géol et de ma thèse, jusqu'à la fin du manuscrit (qui a permis de bien remplir ma bibliothèque Steam, à défaut de ma bibliographie de thèse); Robin et JB, qui m'ont ancré et encré à Saint-Nazaire et donné de l'inspiration sur tous mes projets artistiques; les 'anciens' thésards Jon, Antoine, Modeste, Pierre, Margaux, Gaby, qui m'ont acceuilli au labo et dans l'équipe, avec une mention spéciale à Benjamin dont la thèse m'a beaucoup inspiré pendant l'écriture du manuscrit; les thésards plus récents, Nico, Coco, Paul B., Yves, Zoé, Capu, et toutes les soirées aux Docks, au Delirium, et un peu partout dans Nancy; Fifi (et Julie et Thomas et Arthur) pour les nombreux conseils et l'accueil toujours chaleureux; Guillaume et Paul C. pour leur encadrement que ce soit dans la thèse, pour aller courir dans le parc de brabois ou pour faire une partie de tarot; et bien sûr tous les autres membres de l'équipe, Pauline, Mustapha, Christine, Christophe, sans lesquels le labo RING et surtout son ambiance chaleureuse ne seraient pas ce qu'il sont.

Je voudrais également remercier le consortium RING-Gocad pour m'avoir permis de mener à bout ce travail de recherche en acceptant de financer ma thèse, ainsi que l'équipe administrative de l'ASGA et particulièrement Armelle et Maryse.

Enfin, je voudrais remercier les membres de la communauté scientifiques et de mon jury qui m'ont aidé: Jean pour son aide dès le début de la thèse et lors des comités de suivis; Cedric pour toute l'aide apportée aussi bien pendant les comités de suivi que pendant ma visite à Utrecht, et sans lequel FAIStokes n'aurait sans doute pas atteint un niveau de rigueur suffisant pour obtenir les résultats présents; Laetitia et John pour avoir accepté de relire ma thèse et pour les remarques pertinentes aussi bien sur le manuscrit que pendant la soutenance; et Susanne et Fanny pour leur présence et pour avoir animé la discussion scientifique durant la soutenance.

Résumé étendu

Introduction

L'intérieur de la Terre est le résultat de milliards d'années de déformation. Afin de l'étudier et de trouver les ressources potentielles en son sein, il est nécessaire de comprendre ses changements au cours du temps. La géologie est l'art d'essayer de retrouver ces changements à partir du peu de données disponibles. La géologie structurale, notamment, s'intéresse aux structures qu'il est possible de trouver dans le sous-sol, telles que les horizons et interfaces géologiques et les failles, et à leur déformation depuis leur création. Ces informations et connaissances sur une zone sont souvent condensées en un représentation géométrique permettant de synthétiser et analyser la zone en question. Cette représentation, appelée modèle structural, recense la position théorique des différents objets géologiques importants, tels que les failles et les interfaces entre les différentes couches géologiques.

La restauration structurale intervient sur les modèles structuraux pour faire remonter le temps aux objets géologiques présents. De nombreuses méthodes existent, chacune utilisant des hypothèses différentes, mais les objectifs sont les mêmes:

- étude de la déformation du modèle au cours du temps;
- validation du modèle structural en vérifiant si sa déformation correspond aux hypothèse faites lors de sa création.

Parmi les méthodes de restauration structurale, nous nous intéressons à celles qui visent les bassins sédimentaires d'une taille allant de quelques centaines de mètres à quelques dizaines de kilomètres. Ces bassins sont généralement constitués de couches de roches sédimentaires déformées par des plis et des failles. Les premières méthodes de restauration les visant utilisaient des méthodes principalement géométriques, telles que la conservation de la longueur des horizons, pour aplanir les structures. La restauration géomécanique a été développée comme une méthode de simulations mécanique considérant les roches comme des matériaux élastiques, afin d'introduire des considérations plus physiques dans le processus. Les conditions permettant la restauration restent cependant géométriques (aplatissement de la surface supérieure, failles considérées comme des surfaces sans friction). Dans le domaine de l'étude des bassins évaporitiques, la restauration géométrique ne permet pas la restauration des structures salifères, formées par des phénomènes de fluage, et à la géométrie compliquée. Une méthode de restauration a donc été développée en utilisant les équations de Stokes pour les

fluides très visqueux, associées à une advection en pas de temps négatifs. Cette méthode de restauration n'a cependant été appliquée qu'à des modèles ne présentant pas de failles, et où la surface supérieure est considérée comme aplanie à chaque pas de temps par l'érosion et la sédimentation.

Dans ce manuscrit, j'étudie l'application de la méthode de restauration utilisant les équations de Stokes à des bassins sédimentaires faillés et ayant une topographie non plate. Cela permettrait une possible amélioration de la restauration géomécanique. Pour cela, je fais, dans un premier chapitre, une revue des différentes méthodes de restauration structurale géométriques, géomécaniques et utilisant les equations de Stokes. Je fais également une revue des descriptions matérielles du sous-sol et de la manière de résoudre numériquement les équations de Stokes à l'aide de la méthode des éléments finis. Dans un second chapitre, je décris le code FAIStokes, développé pour appliquer numériquement la méthode de restauration par les équations de Stokes. Je décris également l'application à des modèles de référence permettant de vérifier l'implémentation des différents algorithmes présents. Dans une troisième chapitre, je montre les résultats obtenus sur des modèles simples du sous-sol, ainsi que les premiers problèmes inhérents à la méthode. Dans un dernier chapitre, j'utilise l'application de la méthode à un modèle analogique pour étudier l'influence des différents paramètres de simulation sur les résultats obtenus, et déterminer ainsi les "meilleurs" paramètres dans cette application.

État de l'art

La restauration structurale

La restauration structurale est un ensemble de méthodes permettant de faire revenir un modèle structural à un état antérieur dans le temps. L'objectifs est double: valider le modèle en vérifiant si cet état antérieur est géologiquement possible et probable, et étudier la déformation du modèle au cours du temps. Les méthodes classiques consistent à enlever les déformations dues aux plis et aux failles. À cela s'ajoutent des méthodes prenant en compte d'autres paramètres tels que la déposition et l'érosion de sédiments (e.g., Dimakis et al. 1998), la compensation de l'isostasie (e.g., Allen and Allen 2013), les effets de subsidence thermiques (e.g., Royden and Keen 1980), la decompaction des roches (e.g., Durand-Riard et al. 2011), ou encore la migration inverse de systèmes chenalisés (e.g., Parquer et al. 2017). Dans ce manuscrit, seules les méthodes de restauration visant à enlever l'action des plis et des failles dans des bassins sédimentaires sont étudiées.

Restauration géométrique et cinématique

Depuis le début du siècle dernier, les méthodes de restauration structurale sont principalement basées sur des hypothèses géométriques et cinématiques (e.g., Chamberlin 1910; Dahlstrom 1969; Gratier 1988; Rouby 1994). Les premières méthodes utilisaient la conservation de la longueur et de l'épaisseur des hori-

zons pour les applanir et restaurer ainsi des coupes géologiques. Ces méthodes ont par la suite été améliorées pour prendre également en compte les couches d'épaisseur variable, les déformations hors-plan et les processus volumiques. Ces méthodes, cependant, simplifient considérablement la déformation des roches du sous-sol, négligeant les effets mécaniques à l'intérieur des couches géologiques. Par ailleurs, la plupart des méthodes de restauration ne sont valables qu'en 2D, et les méthodes valables en 3D posent encore problème dès que l'on s'éloigne un peu trop du cas idéal. Dans ce contexte, de nombreux scientifiques ont exposé la nécessité d'incorporer les phénomènes mécaniques dans le processus de restauration (e.g., Fletcher and Pollard 1999; Muron 2005; Maerten and Maerten 2006; Moretti 2008; Guzofski et al. 2009; Al-Fahmi et al. 2016).

Restauration géomécanique

La restauration géomécanique a été développé depuis les années 2000 comme une simulation géomécanique avec des conditions aux limites spécifiques Maerten and Maerten (2001); De Santi et al. (2002); Muron (2005); Moretti et al. (2006); Maerten and Maerten (2006); Durand-Riard (2010); Tang et al. (2016). Dans cette approche, la déformation interne au modèle n'est pas connue *a priori*, elle est calculée en paramétrisant le modèle avec des propriétés élastiques. La restauration elle-même est effectuée grâce aux conditions aux limites et de contact sur les failles. Le problème de cette méthode de restauration est que les failles sont considérées comme de surfaces sans friction, et que les conditions de restauration sont encore principalement géométriques (e.g., l'aplatissement de la surface supérieure, le rattachement des bords de faille). De plus, les conditions élastiques sont des simplifications importantes qui négligent fortement les déformations visco-élastiques et plastiques des roches lors de grandes déformations à l'échelle des temps géologiques. Une autre difficulté apparaissant lors de la restauration géomécanique est le recours à un maillage. En effet, le calcul des déformations élastiques d'un milieu nécessite un maillage conforme aux discontinuités et valide, qui est difficile à obtenir en 3D, et dont la qualité impacte fortement la rapidité et la qualité des simulations. Or, en restauration géomécanique, le modèle peut subir des déformations importantes qui dégradent le maillage et entrainent le besoin d'un remaillage régulier du modèle, opération à la fois difficile et coûteuse en temps de calcul.

Utilisation des équations de Stokes

Les roches se comportent généralement comme des matériaux élastiques lors de petites déformations à des échelles de temps allant jusqu'à la centaine d'années, mais peuvent réagir comme des fluides visqueux lors de grandes déformations à l'échelle des temps géologiques (plusieurs milliers ou millions d'années) (Moretti and Froidevaux 1986; Massimi et al. 2006; May et al. 2014; Cornet 2015; May et al. 2015). Cela a motivé l'utilisation des équations de Stokes pour les simulations géomécaniques, notamment dans les contextes de structures salifères ou dans la modélisation des mouvements du manteau terrestre (Nalpas and Brun 1993;

Weijermars et al. 1993; Fullsack 1995; Thieulot 2011).

Équations générales

Les mouvements des fluides visqueux sont décrits par les équations de Navier-Stokes. Dans le cas des fluides très visqueux, tels que les roches à des échelles de taille et de temps géologiques, on peut montrer que la partie inertielle de ces équations est négligeable. Il est alors possible de simplifier ces équations afin d'obtenir les équations de Stokes montrées en Eq. (1.11). La résolution des équations de Stokes permet d'obtenir le champ des vitesses et la pression dans un milieu constitué de fluides visqueux. Une des particularités de ce champ est qu'il est stationnaire (le temps n'apparait pas dans les équations) et ne dépend que de la répartition des fluides à un instant t. Lorsque des instabilités (dues à la répartition des masses par exemple) apparaissent, la répartition des fluides change, et le champ de vitesse avec elle. Numériquement, ce changement est fait par une advection des propriétés dans le modèle étudié, par exemple en utilisant le schéma d'Euler Eq. (1.12).

Application à la restauration

Les méthodes de restauration telles que la conservation de la longueur et de l'épaisseur des couches ne parviennet pas, le plus souvent, à restaurer les modèles incluant des roches évaporitiques. En effet, les évaporites telles que le sel se déforment par phénomène de fluage à l'échelle des temps géologiques, se comportant alors comme des fluides très visqueux, et formant des structures à la géométrie variée et potentiellement très déformée. Dans ce contexte, une méthode de restauration a été développée par Ismail-Zadeh et al. (2001) en se basant sur des simulations mécaniques considérant les roches comme des fluides très visqueux. La vitesse calculée par la résolution des équations de Stokes ne dépendant que de la disposition des fluides à l'instant où elle est calculée, l'idée derrière la méthode est de l'appliquer avec un pas de temps négatif lors de l'advection du modèle. Cela permet d'avoir une restauration plus physique, les simulations étant entrainées uniquement par le poids et des conditions aux limites naturelles, telles qu'une surface supérieure libre. Cette méthode n'a cependant été appliquée pour le moment qu'à des bassins salifères où les failles sont négligées, et la topographie est plate (ou considérée comme aplanie par l'érosion et le dépôt de sédiments).

Méthodes numériques

Afin d'effectuer la restauration par fluage, il est nécessaire de résoudre les équations de Stokes. Les modèles d'interêt ayant une complexité ne permettant pas la résolution analytique de ces équations, leur solution doit être calculée de manière approchée par des méthodes telles que les éléments finis ou les différences finies.

Descriptions matérielles d'un modèle

Afin d'appliquer des méthodes de résolution des équations de Stokes sur des modèles du sous-sol, il est tout d'abord nécessaire de numériser ces derniers. Pour cela, différentes descriptions existent. Les plus communes sont les descriptions Lagrangiennes et Eulériennes (Cornet 2015). Dans la description Lagrangienne, le point de vue est mis sur l'objet en mouvement: la déformation est calculée sur différents points de modèle, qui sont ensuite déplacés. Cette méthode permet notamment de garder en mémoire le chemin effectué par chacun des points du modèle. Dans la description Eulérienne, les points utilisés pour le calcul de la déformation sont immobiles, et la valeur des paramètres physiques à leur position change en fonction du temps. Cette méthode permet de garder une grille de calcul stable, notamment pour le calcul de champs de vitesse dans des fluides.

Dans les modèles géologiques où de grandes déformations s'opèrent, et où il est nécessaire de garder une trace du chemin parcouru par les différents points du modèle, les deux descriptions précédentes sont limitées. Pour garder les avantages des deux méthodes, la description arbitrairement Lagrangienne ou Eulérienne a donc été développée (e.g., Hughes et al. 1981; Fullsack 1995). Cette description considère un modèle Lagrangien permettant de garder une trace des déformations, mais utilise une grille Eulérienne pour le calcul de la déformation du modèle. Cette grille peut également être déformée indépendamment du modèle, pour permettre à ses points de suivre la topographie ou certaines surfaces géologiques par exemple.

Afin de garder une trace des propriétés physiques et des déformations dans un modèle sans avoir à utiliser un maillage, les méthodes utilisant des particules ont été développées (e.g., van Keken et al. 1997; Asgari and Moresi 2012; Gassmöller et al. 2018). Leur avantage principal est de pouvoir considérer un modèle sans connectivité imposée, dont les propriétés mécaniques sont stockées dans les différents points qui le composent. Cela permet de se débarasser des contraintes de validité du maillage, et des remaillages nécessaires lors de grandes déformations.

La méthode des éléments finis

La méthode des éléments finis est une méthode mathématique de résolution approchée des équations aux dérivées partielles (Hughes 2012). Elle regroupe un grand nombre d'applications, qui utilisent toutes les mêmes étapes:

- Subdivision du modèle en un ensemble d'éléments (appelé maillage).
- Passage des équations aux dérivées partielles de la "forme forte" à la "forme faible" sous forme d'intégrale sur tout le domaine d'étude.
- Discrétisation de l'intégrale sur chaque élément du maillage.
- Discrétisation du domaine fonctionnel afin de calculer la solution approchée de la forme faible dans chaque élément.
- Changement de coordonnées afin de se placer dans un élément de référence où la résolution des équations est triviale.

- Dans chaque élément, cela revient à résoudre un problème matriciel dépendant des contacts avec les éléments adjacents.
- Les problèmes matriciels de chaque élément sont assemblés en un système linéaire unique.
- Un solveur est utilisé pour résoudre le système linéaire.

Développement du code FAIStokes

Le code FAIStokes a été développé afin d'appliquer la méthode de restauration utilisant les équations de Stokes et une advection en temps négatif à des modèles du sous-sol.

Spécificités du code FAIStokes

Le code FAIStokes est écrit en language C++. Il dépend de la bibliothèque d'éléments finis deal.II (Bangerth et al. 2007; Arndt et al. 2019, 2020) et de la librairie RINGpcl pour la recherche de voisins dans les nuages de particules. Les modèles utilisés dans FAIStokes sont discrétisés sur des nuages de points. La résolution des équations de Stokes se fait sur une grille raffinée adaptivement, via la méthode des éléments finis codée dans la librairie deal.II.

À chaque pas de temps, les propriétés mécaniques du modèle (densité et viscosité) sont interpolées sur les éléments de la grille. Ces propriétés sont utilisées pour assembler le système linéaire matriciel. La méthode utilise des éléments de Taylor-Hood Q_2Q_1 satisfaisant les conditions de stabilité de Ladyzhenskaya-Babuŝka-Brezzi. La résolution du système linéaire est faite en utilisant un solveur FGMRes pré-conditionné par une matrice utilisant le complément de Schur. La résolution des équations de Stokes permet de déterminer le champ de vitesse dans le domaine d'étude. Ce champ de vitesse est alors interpolé de la grille de calcul vers les particules à l'aide d'un interpolation quadratique d'ordre deux. Un schéma de Runge-Kutta d'ordre deux est ensuite utilisé pour déplacer les particules.

Afin de pouvoir considérer l'interface entre le modèle et l'air, la condition de surface libre sur la surface supérieure a été implémentée. Cela implique des changements de la topographie, celle-ci est donc décrite par un nuage de points spécifiques. Ces points sont déplacés à chaque pas de temps, puis les noeuds de la surface supérieure de la grille sont déplacés verticalement jusqu'à la position actualisée de la topographie. La déformation des noeuds supérieure est ensuite propagée dans le reste de la grille pour que celle-ci reste valide. Afin d'éviter des dépassements, l'algorithme de stabilisation de la surface libre présenté par Kaus et al. (2010) a été implémenté dans FAIStokes.

Application du code à des modèles de référence

Afin de tester les différentes parties du code et de vérifier la validité des résultats, cinq modèles de références ont été utilisés. Ils ont permis de comparer les résultats

du code à des solutions analytiques et des résultats obtenus par d'autres codes de calcul, dans différents cas de figures. Ces cas incluent plusieurs instabilités de Rayleigh-Taylor avec différentes géométries, permettant de vérifier que la grille de calcul à raffinement adaptatif est à même de fournir des résultats valides, y compris dans des zones avec de forts contrastes de viscosité sur de petits éléments. La qualité de l'interpolation de la vitesse sur la particules a également été testée, ainsi que l'implémentation de la surface libre, et de l'algorithme de stabilisation associé.

Premiers résultats et premiers écueils

Le code FAIStokes a été utilisé pour appliquer la méthode de restauration présentée à différents modèles dans des conditions simplifiées de la réalité géologique.

Premiers résultats

Les deux premiers modèles utilisés visent à reproduire le comportement simplifié de création d'un diapir de sel. Ils sont composés d'une couche de sel et d'une couche de sédiments sus-jacente, qui se déforment par instabilité de Rayleigh-Taylor. Le deuxième modèle a également une couche de sédiment en dessous du sel, et les sédiments au-dessus du sel sont séparés en plusieurs couches aux propriétés variables. Les conditions aux limites utilisées dans ces modèles sont simples (glissement sans friction ou absence de mouvement). Afin de déterminer la qualité de la restauration sur ce type de modèles, une simulation en temps positif a tout d'abord été faite, durant laquelle un diapir de sel s'est formé, puis une restauration du modèle en résultant a été effectuée. Cela a permis la comparaison entre le modèle initial (pré-simulation) et le modèle final (post-restauration). Les résultats sont concluants sur les deux modèles, permettant de valider la méthode de restauration dans des cas à la géométrie et aux conditions aux limites simples. On retrouve cependant une incapacité de la méthode à gérer les déformations trop importantes telles que les sutures dans le sel, déjà évoquée par Ismail-Zadeh et al. (2001).

Introduction de conditions aux limites plus physiques

Afin d'introduire des conditions aux limites plus proches de la réalité, la condition de surface libre a également été testée sur le deuxième modèle de création de diapir de sel. Dans les simulations en temps positif, cette surface libre est stable et se déforme peu. Dans les simulations de restauration, en revanche, des instabilités apparaissent, faisant croître la topographie de manière incontrôlée. Ces instabilités sont dues à l'entrainement de la simulation par le poids. Par exemple, une erreur négative dans le calcul de la vitesse de la topographie va élever la surface supérieure au-dessus de sa position normale (à cause de l'advection en temps négatif). La résolution des équations de mouvement donnant une vitesse qui fait se rapprocher le modèle d'un état de stabilité (en temps positif), la vitesse calculée va être orientée vers le bas là où la surface supérieure est trop haute, élevant

encore la topographie à cet endroit lors de l'advection en temps négatif. Afin de régler cette instabilité, différentes méthodes ont été testées, incluant différentes tractions spécifiques sur la surface supérieure, mais sans résultats significatifs.

Le moyen le plus efficace de gérer la surface libre en temps négatif a été de se placer dans les cas où les erreurs de calcul sont étouffées par un changement important de la topographie. Un modèle en zone d'extension a été utilisé, représenté par une condition de bord avec une vitesse sortante, et utilisant une surface libre pour représenter la topographie. Dans ce modèle, deux failles permettent la création d'un graben en temps positif. La méthode de restauration donne des résultats convaincants sur le modèle de graben résultant des simulations en temps positif. Les instabilités de la surface libre sont écrasées par le mouvement d'extension du modèle, et n'apparaissent qu'à la fin de la simulation, et de manière mineure. Ce modèle permet ainsi de valider la méthode de restauration dans des contextes de bassins sédimentaires faillés, en extension, et avec une surface supérieure considérée comme libre.

Première évaluation du choix des paramètres mécaniques

Un dernier modèle a été utilisé afin d'évaluer les paramètres mécaniques à utiliser en restauration. En effet, les modèles dont on souhaite la restauration sont construits à partir de données plus ou moins éparses et précises, et les propriétés des roches à l'intérieur des modèles ne sont en général pas connues. La géométrie à la fin de la restauration n'est pas connue non plus, et il est souvent difficile de savoir si la rétro-déformation est correcte ou non. Dans le modèle utilisé içi, les conditions aux limites sont simples (glissement sans friction), mais la géométrie initiale a été déterminée de manière stochastique par Clausolles et al. (2019) à partir d'une image sismique. Ainsi, ce cas peut être considéré comme la simplification d'une application réelle. Afin de limiter les paramètres variables, on a fixé la densité (connue) de la couche de sel, ainsi que sa viscosité. Un plan d'expérience a alors été mis en place pour tester l'influence de la densité et de la viscosité des sédiments sur la restauration.

Les résultats sont plutôt concluants, et la couche de sel revient à un état majoritairement plat. La différence majeure entre les différentes expériences est le temps mis par le modèle à retrouver cet état. La donnée de temps de mise en place du diapir pourrait ainsi aider à déterminer de manière plus précise les paramètres à utiliser. Dans les modèle restaurés, on retrouve par ailleurs une cicatrice laissée par le sel dans les sédiments. Cela est sans doute dû à une formation syn-sédimentaire du diapir, et une restauration totale du modèle aurait alors nécessité de retirer les couches de sédiments au fur et à mesure de la restauration.

Discussion sur les premiers résultats

Globalement, les résultats de l'application de la méthode de restauration à des modèles synthétiques ou simplifiés du sous-sol sont concluants. Deux questions majeures restent cependant à explorer pour appliquer cette méthode à des modèles géologiques. Premièrement, quelles conditions aux limites choisir pour les

différentes simulations, et est-il possible de stabiliser l'utilisation d'une surface supérieure libre en restauration? Deuxièmement, quelles propriétés matérielles effectives appliquer aux roches et à leurs fractures?

Restauration d'un modèle analogique

Un modèle d'expérience analogique a été utilisé afin de tester la méthode sur un cas de restauration plus complexe, non synthétique, mais dont la rétro-déformation est connue.

Passage d'un modèle expérimental à un modèle numérique

Un modèle d'expérience analogique est un dispositif expérimental composé d'une boîte remplie de couches de différents matériaux, dont on étudie la déformation. L'idée est de choisir des matériaux dont les propriétés mécaniques imitent les déformations se passant à des échelles d'espace et de temps géologiques. Les données sur le modèle analogique utilisé ici proviennent de l'IFPEN et de C&C Reservoirs, 2016, DAKS^{TM} (Digital Analogs Knowledge System). Elles correspondent à une expérience modélisant la déformation d'un bassin sédimentaire en extension au cours du temps. Plusieurs couches alternant entre le sable et le pyrex (simulant des sédiments) sont déposées sur une base de silicone (simulant une couche d'évaporites) au cours du temps, imitant un dépôt stratigraphique. La boîte dans laquelle évolue le système est inclinée afin d'utiliser la gravité pour simuler l'extension du modèle. La densité des couches est connue, de même que la viscosité du silicone. L'étude des images de tomographie réalisées durant l'expérience permet de déterminer l'altitude après le dépôt de chaque couche, et le temps entre chaque dépôt.

J'ai choisi d'utiliser le modèle à sa taille réelle, afin de profiter de toutes les données disponibles directement, sans ajouter d'incertitudes liées à la mise à l'échelle du modèle. Une fois le modèle numérisé sous forme de nuage de particules, les inconnues pour la restauration sont alors les conditions aux limites à utiliser et la viscosité effective dans les couches de sable et de pyrex, et dans les failles présentes en leur sein.

Influence des conditions aux limites

Afin de tester tout d'abord l'impact des conditions aux limites sur la restauration, la viscosité dans les couches de sable et de pyrex et au coeur des failles a été fixée sur un nuage de particules. Celui-ci a ensuite été utilisé dans différentes configurations de conditions aux limites.

Premièrement, le modèle a été restauré en fixant la vitesse sur les bords: une condition d'aplatissement de la surface supérieure a été utilisée, et une vitesse dépendant du volume entrant imposée sur la surface en extension à droite du modèle. Les résultats obtenus sont corrects, et permettent de vérifier la possibilité d'une restauration en utilisant le même type de conditions aux limites que la restauration géomécanique usuelle.

Afin d'utiliser des conditions aux limites plus naturelles, le cas de la surface à droite du modèle a tout d'abord été étudié. En effet, l'application d'une vitesse spécifique introduit une sur-paramétrisation du modèle pouvant entrainer des dépassements sur la vitesse à l'intérieur du modèle. Cette condition néglige également la différence de vitesse en fonction de l'altitude sur ce bord. Plusieurs tests ont donc été effectué avec une condition de Neumann en traction. Celle-ci, si elle prends en compte la valeur de la pression lithostatique dans le modèle, permet de mieux équilibrer le système lors de la restauration.

Le cas de la surface supérieure du modèle a ensuite été étudié. En effet, cette surface est en contact avec l'air durant l'expérience du modèle analogique, et devrait donc être considérée comme une surface libre. Cela permet de se détacher de la condition d'aplatissement de la topographie, alors que la vitesse réelle à cet endroit n'est pas connue. L'application d'une surface supérieure libre permet également de vérifier que l'utilisation d'une traction dépendant de la pression lithostatique sur le bord droit du modèle est nécessaire pour équilibrer la déformation lors de la restauration.

Influence des paramètres mécaniques

L'étude des conditions aux limites a également permis de voir que les propriétés matérielles utilisées jusque là ne permettaient pas la restauration du modèle analogique. En particulier, la viscosité des couches de sable et de pyrex était trop faible.

Afin de déterminer les 'meilleures' propriétés matérielles effectives dans le modèle, un plan d'expérience a été mis en place. Les autres paramètres étant donnés, ce plan porte sur les variations de la viscosité effective des failles et des couches de sable et de pyrex. Par soucis de simplicité, la viscosité a été considérée comme constante et la même dans les couches de sable et de pyrex (simulant le dépôt stratigraphique). Huit simulations de restauration ont été effectuées sur la strate la plus récente du modèle, pour des viscosités entre 10^5 et 10^7 Pa.s pour le dépôt stratigraphique, et entre 5.10^3 et 5.10^6 Pa.s pour les failles.

Pour comparer les résultats obtenus, un premier critère, basé sur la distance de la topographie à l'altitude de référence à la fin de la restauration de la strate, a été utilisé. Ce critère permet de voir que les simulations se rapprochent globalement de l'altitude visée au début de la simulation, mais que certaines s'en éloignent ensuite. L'état du modèle à la fin des huit simulations a ensuite permis de comprendre de manière plus détaillée les différences entre les simulations. Ainsi, une viscosité trop faible dans le dépôt stratigraphique entraine une déformation trop importante du modèle, tandis qu'une viscosité trop importante dans les failles ne permet pas de restaurer leur rejet. Finalement, ces simulations ont permis d'affiner la valeur de viscosité à appliquer dans le modèle, et ont également permis de voir qu'il est nécessaire, pour restaurer le modèle, d'appliquer une viscosité différente dans chacune des failles.

Discussion sur les résultats obtenus sur le modèle analogique

L'étude du modèle analogique a permis plusieurs résultats. Premièrement, elle a montré l'application de la méthode de restauration à un modèle d'entrée obtenu de manière expérimentale (et non synthétique), mais dont la géométrie passée est connue et peut être comparée aux résultats. Cela a permis de valider la méthode de restauration en utilisant des conditions aux limites cinétiques et en considérant les failles comme des zones de plus faible viscosité. Deuxièmement, des conditions aux limites plus physiques peuvent être envisagées pour la restauration. Une traction basée sur la pression lithostatique permet ainsi de mieux équilibrer la vitesse dans les simulations, tandis qu'une surface supérieure libre permet de déterminer les propriétés matérielles effectives du modèle. Enfin, une plan d'expérience a permis de réduire l'incertitude sur les propriétés matérielles à appliquer dans le modèle, et de repérer certaines simplifications à retirer, comme la considération d'une même viscosité dans toutes les failles.

Cette étude permet d'envisager l'application de la méthode à des modèles structuraux du sous-sol. Une mise à l'échelle des propriétés effectives dans le modèle analogique pourrait alors permettre leur détermination dans des modèles dont la déformation est analogue.

Conclusions et perspectives

Le but de cette thèse était de trouver une manière d'appliquer des conditions plus physiques lors de la restauration géomécaniques de modèles structuraux. Pour ce faire, l'idée a été d'utiliser une méthode de restauration basée sur les équations de Stokes et d'aller plus loin en l'appliquant à des modèles présentant des failles et une topographie variable. Je récapitule içi les contributions apportées par ce travail, et les perspectives pouvant être intéressantes pour la suite.

Tout d'abord, le code FAIStokes a été développé pour appliquer la méthode de restauration utilisant les équations de Stokes. Ses éléments ne sont pas novateurs, mais il a permis de montrer qu'il est possible d'appliquer cette méthode de restauration en utilisant une discrétisation particulaire du milieu et en effectuant les calculs sur une grille à raffinement adaptatif. Cette méthode permet d'obtenir des résultats avec une bonne précision sans trop augmenter le temps de calcul, et sans avoir à mailler le domaine d'étude. Elle peut cependant entrainer des nuages de particules de grandes tailles, et une distortion de la grille de calcul dans le cas d'une topographie trop accidentée.

La deuxième contribution de cette thèse a été de montrer que la restauration basée sur les équations de Stokes est à même de fonctionner sur des modèles présentant des failles et une topographie qui évolue en fonction du temps. La méthode a été utilisée sur différents modèles synthétiques, où elle a montré son potentiel pour restaurer des modèles avec des conditions aux limites simples. La présence d'une condition de surface libre sur la topographie a présenté des difficultés, mais ces dernières ont pu être relaxées par l'ajout de conditions telles que des failles et une extension latérale du modèle.

La dernière contribution a été l'application de la méthode de restauration à un modèle issu d'une expérience de déformation analogique. Cela a permis tout d'abord de vérifier que la méthode de restauration utilisant les équations de Stokes fonctionne avec des conditions aux limites en déplacement. L'impact de différentes conditions aux limites a ensuite été étudié, afin de remplacer les conditions en déplacement par d'autres plus physiques, telles qu'une condition de surface supérieure libre, ou une condition de traction sur les côtés du modèle. Ces conditions peuvent cependant déséquilibrer les modèles lors de la restauration si les propriétés matérielles utilisées ne sont pas correctes. Un plan d'expérience a dont été mis en place pour trouver les propriétés matérielles les plus justes (celles qui ne déséquilibreront pas les simulations de restauration). Ce plan a permis de réduire les incertitudes sur les propriétés à appliquer dans le modèle analogique, et de mettre le doigt sur certaines simplifications trop importantes, telles que l'usage d'une viscosité égale dans toutes les failles.

Plusieurs perspectives s'ouvrent avec les résultats obtenus.

Premièrement, le code FAIStokes pourrait être amélioré de différentes manières. Afin de dimminuer le temps de calcul, une contribution purement technique serait de paralléliser le code. Cela permettrait d'effectuer une gamme de tests plus large, et serait, il me semble, nécessaire pour envisager d'appliquer la méthode à des modèles 3D du sous-sol. Différents critères d'analyse pourraient également être implémentés, tels que le calcul du rejet des failles ou de la déformation locale, afin d'avoir d'autres moyens de comparer les résultats obtenus. Enfin, il pourrait être intéressant d'envisager d'autres méthodes d'interpolation pour le transfert d'information entre les particules matérielles et la grille de calcul. Une certaine forme d'homogénisation permettant de trouver les paramètres effectifs locaux, par exemple, pourrait dimminuer les forts contrastes locaux de viscosité. Cela engendrerait alors une moindre pression sur le solveur, et une dimminution du temps de calcul.

Deuxièmement, la méthode pourrait être appliquée au modèle analogique de manière plus approfondie. Cela permettrait d'effectuer plus de tests sur certains paramètres qui n'ont pas été étudiés mais pourraient avoir un impact sur la restauration. Il serait alors possible, par exemple, de déterminer la meilleure distribution de viscosité dans les failles, ou encore de tester l'impact d'une viscosité variant en fonction de l'age ou de l'altitude des couches ou des failles. La construction d'un modèle structural 3D de l'expérience analogique, et sa restauration, permettraient également d'étudier la viabilité de la méthode en 3D, et sa capacité à gérer les déformations hors-plan.

Enfin, bien que l'ajout de conditions plus physiques dans la restauration géomécanique soit intéressant en soit, le but est également de fournir une méthode fonctionnelle de restauration de modèles structuraux du sous-sol. Dans un premier temps, l'application de la méthode à d'autres modèles analogiques permettrait la détermination des paramètres effectifs pour différents types de déformation. La mise à l'échelle de ces paramètres effectifs pourrait alors guider le choix des paramètres à appliquer dans des modèles du sous-sol à une échelle de

temps géologique. Dans ces modèles, les conditions aux limites sont également plus difficiles à déterminer. La restauration basée sur les équations de Stokes pourrait être un moyen de trouver les 'meilleures' conditions, qui équilibrent au mieux les simulations mécaniques en temps négatif.

Introduction

Importance of structural restoration

Understanding and modeling the subsurface

The Earth's subsurface is the result of billions of years of deformation. In order to study it and the potential ressources inside it, it can be extremely valuable to understand its changes through time. Indeed, when modeling the subsurface, the geological history helps to link the different scales and resolutions at which the data is available (particularly where the available data is limited). On the surface, the topography can be obtained with a good precision thanks to the current technology, but the geological map is constrained by how the surveys that constructed it were led, their precision and the density of the outcrops and vegetation. It can be complemented by well logging, which gives high precision over the type and properties of rocks inside the Earth, but is limited to 1D measures, and needs heavy equipment (which also makes it highly expensive). At a larger scale, seismic reflection imaging can give 2D data (or 3D data in the case of whole seismic surveys) over a large area, but it has a lower resolution than well logging and it can yield significant interpretation uncertainties. Moreover, it only gives a measure of the impedance heterogeneity inside the subsurface, which can be used to obtain the position of geological interfaces, but not their physical properties (Sato et al. 2012; Fomel and Landa 2014). Once the data is obtained, geologists use their knowledge to link the different scales and form a hypothesis on the history of an area. One way to sum up both the data and geological knowledge is to make a structural model, representing the geometry of the subsurface in the area. This structural model has two types of uncertainties: from measures, depending on the precision and the resolution of the data, and from the hypotheses that were made during its construction, depending on how the history of the area is understood (Groshong 2006; Fossen 2016). As a result, a better understanding of the deformation history of the subsurface can lead to less uncertainty on the characterization of its geometry. Most of all, a wrong interpretation of the deformation history can lead to a completely false characterization of the subsurface geometry.

Moreover, the presence of natural ressources inside the subsurface depends on its geological history. In petroleum geosciences, for example, the history of a sedimentary basin determines its economical interest. Indeed, kerogen can only be transformed from organic matter by specific bacteria, under specific anaerobic conditions. This kerogen can then only produce oil and gas inside a buried source rock and under specific pressure and temperature conditions. Finally, the hydrocarbons need a sufficient pressure to leave the source rock. Even then, they need to be accumulated in natural reservoirs

in order to be collected. These reservoirs are formed by permeable rocks and sealed by impermeable natural geological traps (such as clay layers of fault systems), so their formation also depends entirely on the history and deformation of the basin (Hatcher et al. 1983; Suggate 1998; Landais et al. 1994; Mello et al. 1995; Massimi et al. 2006). In the mining industry, deformation and fracturation of a zone, as well as fluid circulation through time, affect greatly the potential mineralizations inside an area (Tripp and Vearncombe 2004). Past strain also affects current stress in the subsurface, which is important to consider for the stability of human-made structures.

Restoration as a validation tool

Structural restoration has been developed as a validation tool, to check if a structural model and its history are consistent with the hypotheses on which the model relies (Chamberlin 1910; Dahlstrom 1969; Gratier 1988; Rouby 1994; Dimakis et al. 1998; Maerten and Maerten 2001; Medwedeff et al. 2016). The idea is to try and make a model go back in time using a set of rules, and verifying if the restored state of the model is geologically reasonable. This allows a measure both of the validity of the structural model itself, and of the validity of the hypotheses that were made on its history. It can also give new insight on the deformation history of an area, by analyzing the strain of the rock layers during retro-deformation for example.

A multitude of restoration methods exist, depending on the various parameters of the modeled area, such as:

- Its scale, ranging from fault-throws of a few millimeters to outcrops several kilometers large.
- The scale of its deformation, from lightly folded area to highly deformed mountain ranges.
- The geological objects inside it, such as faults, evaporite layers, channelized systems, ...
- The data and knowledge available, from outcrops data to full geological surveys incorporating seismic and well data.

In this manuscript, we mainly focus on models of sedimentary basins ranging from a few hundreds of meters to a few tens of kilometers wide, where the rock layers are folded and faulted.

In this context, some of the first restoration principles were laid by Dahlstrom (1969), who observed the apparent layer thickness uniformity in a fold and thrust belt. He then used it to assimilate the comparison of relative line-length of pre-growth layers to verifying the conservation of mass, providing a validation criterion for the interpretation of cross-sections. Different studies then led to ways to include fault geometry as a validation criterion (e.g., Boyer and Elliott 1982; Suppe 1983; Medwedeff and Suppe 1997). Area balancing was also used in cross-sections where the folds and faults impaired the conservation of layer thickness during deformation (e.g., Epard and Groshong 1993). This all led in turn to the concept of retrodeformability as a validation tool, where past and present geometry states, as well as the deformation path linking the two, are analyzed to check if they are geologically possible and probable.

Advent of geomechanical restoration in two fields, and its current limits

Following the first methods, various schemes emerged to complement or upgrade the retro-deformation restoration, such as map and multi-map restoration, pseudo-3D analyses or adaptations of the GeoChron model (e.g., Gratier and Guillier 1993; Mallet 2002; Lovely et al. 2018). These allowed a better accounting of the geology, particularly by introducing 3D restoration in models where out-of-plane deformation was large. One of the downfalls of these methods, however, is that they are still mainly based on geometrical considerations. To introduce more physical and mechanical considerations, several fields developed restoration methods based on mechanical simulations.

Geomechanical restoration of sedimentary basins

In sedimentary basins, structural models consist mainly of sedimental rock layers which have been folded and faulted. Other deformation mechanisms also include erosion and deposition of sediments, and compaction of the layers. In these setups, geomechanical restoration was introduced as a mechanical simulation in which the rock layers are modeled with elastic properties and the faults by free-slip surfaces (e.g., Maerten and Maerten 2001; Muron 2005; Moretti et al. 2006; Durand-Riard et al. 2013b). The restoration itself is performed with specific boundary conditions, such as the flattening of the top surface or the removal of fault throw by binding the hanging-wall and footwall cutoff lines. While these methods introduce more physical strains than those of purely geometrical schemes, they are still limited in several ways. Firstly, the deformation drive for the simulations is still based on geometric unfolding and unfaulting. These simplifying conditions are unphysical and do not necessarily respect the paleo-stress state. Secondly, rock behavior is only modeled with elastic properties. While these are a good assessment of rock deformation at timescales up to a few thousand years, they neglect the important viscous and plastic behavior that can appear at geologic timescales. Moreover, they force the use of overly simplifying hypotheses, such as considering the interface with a salt layer as a free surface (Chauvin et al. 2018). Lastly, current geomechanical restoration methods rely on a surface or volume mesh for the computation of the model strain and deformation. These meshes are used because they can precisely account for the different scales and shapes of geological objects. Their construction, however, can be complicated, particularly in 3D. Moreover, the precision on computations using them relies on their validity. In restoration, the model undergoes large deformations, distorting the mesh and invalidating it. Consecutively, the model needs to be edited and remeshed, which takes time and limits the application of geomechanical restoration as a validation tool.

Creeping flow restoration of evaporites basins

In evaporitic basins, the deformation inside structural models is dominated by a large variety of salt structures. Indeed, at geological timescales, evaporites, and particularly rock salt, behave with a creeping behavior. This leads to salt forming extremely various shapes, as can be seen in Fig. 1. In such models, geometrical restoration isn't able to

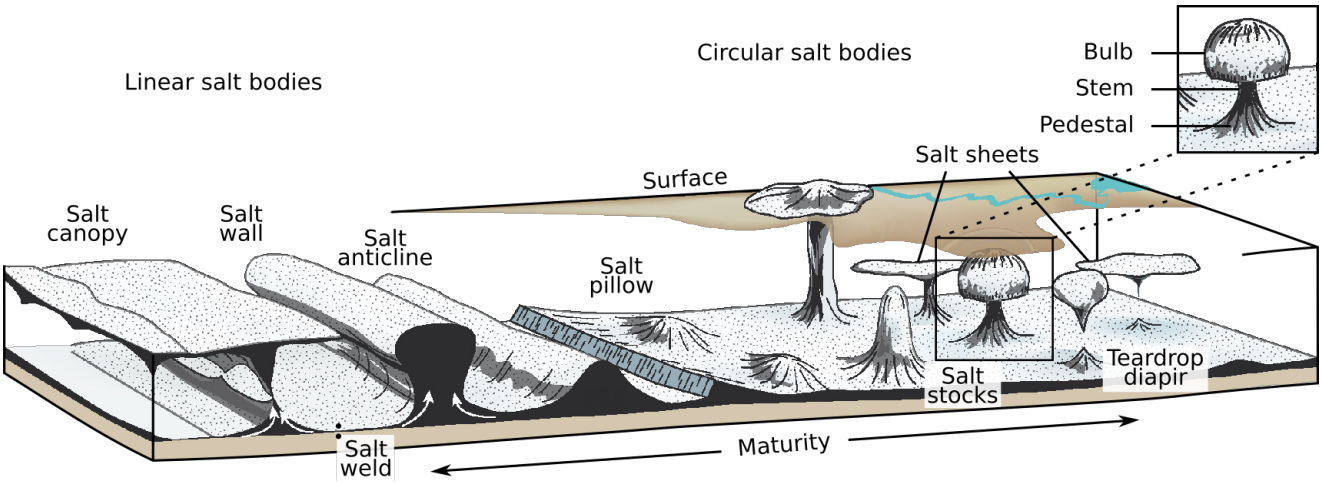

Figure 1: Variability of salt structures, depending on the surrounding sediments, the rate of sedimentation and erosion, and the regional and local tectonic movement. Adapted from Fossen (2016) by Clausolles (2020).

deal with the complicated interfaces between sediment and salt. To solve this issue, creeping flow restoration was developed by building upon the mechanical behavior of salt, and modeling its retro-deformation with Stokes equations and backward time stepping (Ismail-Zadeh et al. 2001; Kaus and Podladchikov 2001; Ismail-Zadeh et al. 2004b; Fernandez 2014). It showed good results on analytical 2D and 3D models, as well as depth-converted cross-sections. In those setups, however, faults were neglected, and the top surface in contact with air was considered as flattened by erosion and sedimentation at each time step.

Goals, approach and contributions

Goals and manuscript organization

We have shown that geomechanical restoration has several issues. Here, we try to resolve some of them by applying creeping flow restoration to sedimentary basins that are folded and may present faults. For that, we focus on these questions:

- How to improve geomechanical restoration by replacing some of its geometric conditions by more physical ones?
- Is it possible to apply creeping flow restoration to basin-scale models including faults, sedimentation and extension processes, and generally non-flat topography?
- Is it possible to model faults as shear zones with an effective viscosity?
- What is the impact of different boundary conditions on the simulation results?
- How to choose the material and effective properties of the layers inside a model?

In order to answer them, the manuscript is composed of four chapters. The first chapters reviews in detail the previous restoration methods with geometric, geomechanic and creeping flow methods. It also reviews the different ways of considering the subsurface

in mechanical simulations, and some of the specificities of applying the Finite Element Method to solve the Stokes equations numerically. Its aim is to see in more detail previous restoration methods and their advantages as well as their issues, and provide first methodological keys on how to choose a scheme to do creeping flow restoration on sedimentary basins. The second chapter introduces the software that was developed for creeping flow restoration. Its aim is to detail the choices that were made during the development, and their reasons in light of restoration challenges. It also provides keys on how to build such a software, and benchmark it. The third chapter presents the results obtained with the method on various simple models. Its aim is to assess the capability of the creeping flow restoration scheme and its issues, on sedimentary basin models with simplified setups and boundary conditions. It also gives first means of choosing the material and effective properties inside the models. The fourth chapter presents the results obtained on a laboratory analogue model. Its aim is to measure the impact of the different choices that are made when restoring a complex model, such as the choice of boundary conditions, material properties and effective properties.

Table 1 lists the accronyms and symbols throughout the manuscript, as well as their unit (if they have one).

Contributions of the thesis

The contributions of the present thesis and manuscript are:

- Building up the creeping flow restoration method using a numerical technique which involves particles and adaptive grid refinement in 2D.
- Testing the creeping flow restoration method on models which include faults and a non-flat top free surface.
- Applying the method to a laboratory analogue model, giving an assessment of the issues as well as the impact of the choice in boundary conditions and material and effective properties.

Context of the thesis

This PhD thesis was done in the frame of the RING Team of the GeoRessources laboratory, at the Université de Lorraine. It was supervised by Professor Guillaume Caumon and by Associate Professor Paul Cupillard from Université de Lorraine. Cedric Thieulot, Associate Professor at Utrecht University, also collaborated by providing scientific and technical expertise. Funding for the PhD was provided by the RING-Gocad consortium.

Previous works on restoration in the RING Team include Muron (2005); Durand-Riard (2010); Chauvin (2017). One of the aims of the PhD thesis was to use Arbitrary Lagrangian Eulerian methods to properly handle large deformations in geomechanical restoration; that was, in time, what led to the use of the Stokes equations. As the team was not familiar with their use, a significant part of the thesis was dedicated to developing a software for creeping flow simulations. The Underworld software was first used for various tests. Secondly, I tried adapting the RINGMecha software, developed during the PhD theses of Chauvin (2017) and Mazuyer (2018), and using the MFEM library. As it was specialized in dealing with tetrahedral meshes, the idea was abandoned

for the benefit of using grids in an ALE scheme. After reviewing several softwares advised by Cedric Thieulot, I decided to code a software in C++, using the Deal.II library as a base for the Finite Element computation parts of the code. It allowed more freedom on the development of algorithms specific to creeping flow restoration, while being compatible with the license for the RING-Gocad consortium sponsors. This software, called FAIStokes, was developed during the rest of the PhD thesis, and is used for all the results presented in this manuscript. It involved specifically:

- Getting familiar with the deal.II library through the lectures of W.Bangerth, available online, and the deal.II tutorials.
- While continuing the tutorials, starting the development of FAIStokes, involving the implementation of particle swarm algorithms. These algorithms were first developed from scratch, and then derived from the RINGpcl library (developed in the RING team) for the use of neighboring particles research trees.
- Implementing several benchmarks to test, compare and verify the results of the code.
- Upgrading different parts of the code along the way (property and velocity interpolation, particle swarm density, dealing with constant and variable flow boundary conditions, implementation of a lithostatic pressure traction on the side boundaries, ...)

Communications associated to this thesis

Notations: $^{(r)}$*peer-reviewed article,* $^{(o)}$*oral presentation,* $^{(p)}$*poster presentation,* $^{(a)}$*proceeding article,* $^{(e)}$*extended abstract.*

Peer-reviewed article

$^{(r)}$ M. Schuh-Senlis, C. Thieulot, P. Cupillard and G. Caumon (2020). Towards the application of Stokes flow equations to structural restoration simulations. *Solid Earth*, doi: 10.5194/se-11-1909-2020.

Conferences

$^{(o)}$ M. Schuh-Senlis, C. Thieulot, P. Cupillard, and G. Caumon (2019). Towards the application of Stokes' flow equations to structural restoration simulations. In *20th Annual Conference IAMG 2019*.

$^{(o,e)}$ M. Schuh-Senlis, C. Thieulot, P. Cupillard, and G. Caumon (2020). Structural restoration of geological structures with viscous Stokes flow - principle and first results. In *82th EAGE Conference and Exhibition 2020*, doi: 10.3997/2214-4609.202010733.

RING Meeting articles

[(a)] M. Schuh-Senlis, P. Cupillard, G. Caumon, and Jean Braun (2020). Creeping flow equations for the simulation of large deformations and their possible application to structural restoration: a bibliographic review. In *RING Meeting 2018*.

[(a)] M. Schuh-Senlis, C. Thieulot, P. Cupillard and G. Caumon (2020). Towards the application of Stokes' viscous flow equations to structural restoration simulations. In *RING Meeting 2019*.

[(a)] M. Schuh-Senlis, C. Thieulot, P. Cupillard and G. Caumon (2020). Application of Stokes flow equations to structural restoration simulations. In *RING Meeting 2020*.

Table 1: List of accronyms and symbols throughout the manuscript.

Acronym	Meaning
ALE	Arbitrary Lagrangian Eulerian
PIC	Particle In Cell
PDE	Partial Differential Equation
FEM	Finite Element Method
FDM	Finite Difference Method
FE	Finite Element
CG	Conjugate Gradient
FGMRes	Flexible Generalized Minimal Residual
CVI	Conservative Velocity Interpolation
FSSA	Free Surface Stabilization Algorithm
CFL	Courant-Friedrichs-Lewy
LBB	Ladyzhenskaya-Babuŝka-Brezzi
GUI	Graphical User Interface
EGS	European Geophysical Society
CPU	Central Processing Unit (in computers)
Symbol	**Meaning and units**
$\overline{x}$	position (m)
t	time (s)
$\overline{u}$	displacement (m)
$\overline{v}$	velocity (m.s^{-1})
$\overline{\nabla}$	del operator (m^{-1})
ρ	density (kg.m^{-3})
η	dynamic viscosity (Pa.s)
p	pressure (Pa = kg.m^{-1}.s^{-2})
$\overline{\overline{\sigma}}$	Cauchy stress tensor (kg.m^{-1}.s^{-2})
$\overline{f}$	sum of volumic forces (kg.m^{-2}.s^{-2})
$\overline{\overline{\overline{\overline{C}}}}$	elastic fourth-order tensor (kg.m^{-1}.s^{-2})
$\overline{\overline{\epsilon}}$	strain tensor (non dimensional)
$\overline{\overline{\tau}}$	deviatoric part of the stress (kg.m^{-1}.s^{-2})
$\overline{\overline{I}}$	identity tensor (non dimensional)
$\overline{\overline{W}}$	material spin tensor (non dimensional)
Re	Reynolds number (non dimensional)
Fr	Froude number (non dimensional)
Ω	domain of study
Γ	boundary of Ω

Chapter 1

State of the art

Contents

Abstract In this chapter, I first review the methods that have been used in the literature for the structural restoration of sedimentary basins, as well as their limits. I start with the first methods using purely geometric means, and then present the methods introducing mechanical simulations in the process. Secondly, I introduce the principles behind Stokes flow simulations and how they have been used for the restoration of models including salt layers. I also point out how they can be used to simulate other rheologies. Finally, I present some specificities of the implementation of creeping flow simulations in a numerical code. To do so, I first review the approaches used to represent the material model throughout the simulation. Then I review the key points of the FEM and outline some details of its application to the resolution of the Stokes equations.

1.1 Introduction

Structural restoration consists of trying to make a structural model go back in time. It serves two purposes. First, it is used to verify if the state of the model before its deformation is geologically possible and probable, and as such, makes a useful tool to assess the validity of the model. Second, it can be used to study and analyze the deformation and fracturation history of the area, and eventually check if it is in accordance with the hypotheses that were made for the creation of the structural model. The first methods used purely geometrical means to restore structural models. Later on, geomechanical restoration was developed to tend to the need for more mechanical assumptions, but still relies on geometrical conditions and only considers elastic motion. Creeping flow restoration was developed for the restoration of models including salt structures that could not be handled with geometrical means, and was used successfully on different types of models. It relies on the Stokes equations, the implementation of which in a numerical code having a few specificities.

1.2 Structural restoration

Geological model restoration covers a number of different processes and methodologies. The classical techniques are unfolding and unfaulting using length/area preservation in order to remove the effects of tectonic forces. In addition to this, a large number of methods have been developed to take into account the effects of other important parameters, like erosion and deposition of sediments (e.g., Dimakis et al. 1998; Chauvin 2017), isostasy compensation (e.g., Allen and Allen 2013), thermal subsidence due to mantle thermal effect (Royden and Keen 1980; Allen and Allen 2013), rock decompaction due to a change of load (e.g., Athy 1930; Durand-Riard et al. 2011; Allen and Allen 2013), or, at a smaller scale, the reverse migration of channelized systems (e.g., Parquer et al. 2017). These methods allow us to assess the temporal evolution of a structural model, in

order to evaluate its consistency and test the hypotheses which led to its construction. It can also serve to quantify the shortening of an area, or analyze the strain in a current model. Paleo-basin geometries consistent with present-day observations can then be generated, for use in more elaborate hydro-mechanical forward models (e.g., Bouziat et al. 2019). In this manuscript, the focus is put on structural restoration based on unfolding and unfaulting. The following section is largely based on the bibliographic review on the subject by Chauvin (2017).

1.2.1 Geometric and kinematic restoration

Since the beginning of the last century, structural restoration methods have been mostly based on geometric and kinematic assumptions (e.g., Chamberlin 1910; Dahlstrom 1969; Gratier 1988; Rouby 1994; Groshong 2006; Lovely et al. 2018; Fossen 2016).

Their first implementation was the balancing restoration, which relies mostly on the conservation of layer bed area and thickness to restore cross-sections (e.g., Chamberlin 1910; Dahlstrom 1969; Groshong 2006) (Fig. 1.1). Its major drawback, as every other 2D method, is to consider that deformation can only happen in the plane of the cross-section. This is possible only if the out-of-plane deformation can be considered negligible, which precludes applications in settings such as strike-slip systems for example.

Map restoration has been developed to study deformations that are mainly horizontal (e.g., Cobbold and Percevault 1983; Gratier et al. 1991; Rouby 1994; Ramón et al. 2016). It considers structural models as a stack of layers modeled by surfaces that are folded and faulted, and aims at flattening these surfaces. This method is based on geometrical conservation and recovery of fault offsets, and restoration of horizon surfaces underlying the top layer is performed using kinematic laws such as flexural slip or simple shear. The resulting computed displacement can be used to analyze the strain and stress along the horizon surface. Although all the horizons are defined in a 3D space, this restoration process considers only surfaces and not the entire volume of the model; it is therefore qualified as 2.5D.

Finally, fully 3D geometrical methods have also been developed (Massot 2002; Muron 2005; Medwedeff et al. 2016), allowing the tracking of internal volumetric deformation. They are all based on the minimisation of deformation and on volume conservation. Among them, Massot (2002) relies on unfolding and unfaulting the uppermost horizon and then interpolating the deformation in the rest of the model on a regular grid representing the geological volume. This interpolation is made using Discrete Smooth Interpolation (DSI) (Mallet 1989, 1992, 1997), and was later extended to tetrahedral meshes. Another method of volumic restoration by Medwedeff et al. (2016) and Lovely et al. (2018) is based on depositional coordinates (GeoChron model) computed using two types of deformations: minimal deformation and flexural slip (Mallet 2004; Moyen 2005). As 3D methods only work in specific setups, however, most applications of geometric and kinematic restoration remain 2D (cross-section and map restoration).

The main issue with all these methods is that they considerably simplify rock deformation mechanisms. Indeed, they rely on a global simple shear (or flexural slip), assumption which generally ignores mechanical layering effects. Moreover, the principle of masse conservation is reduced to the conservation of the surface or volume of the

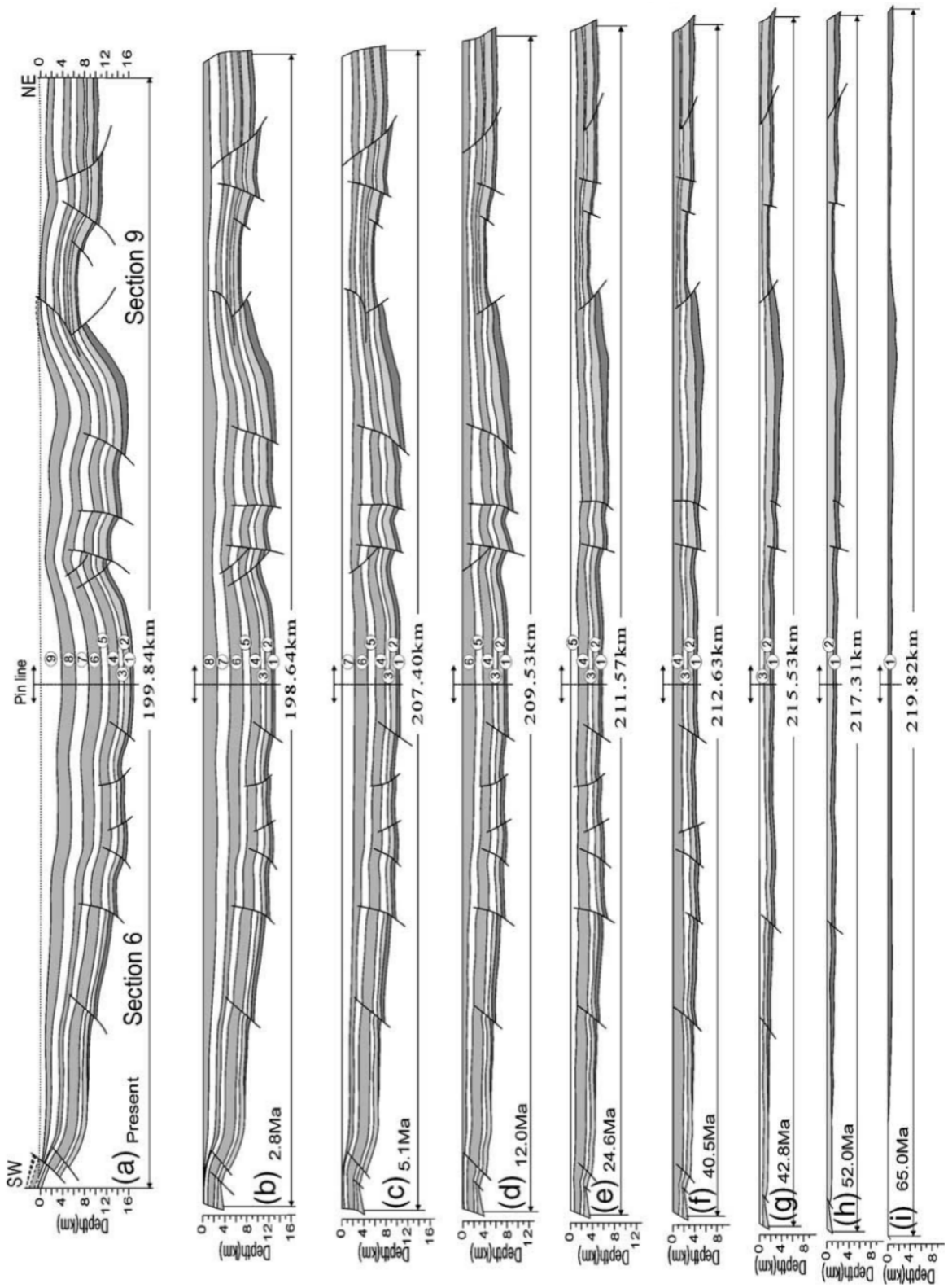

Figure 1.1: Example of an application of the balancing restoration, to restore sequentially a cross-section from the Qaidam basin in South-West China, from Zhou et al. (2006). (a) is the cross-section before the restoration, and (b) to (i) show the restoration of each of the geological layers.

layers. In this light, numerous authors have stated the necessity of incorporating mechanics into the restoration of geological models (e.g., Fletcher and Pollard 1999; Muron 2005; Maerten and Maerten 2006; Guzofski et al. 2009; Al-Fahmi et al. 2016).

1.2.2 Geomechanical restoration

Mechanics-based restoration has been developed since the 2000s as a geomechanical simulation with specific boundary values (Maerten and Maerten 2001; De Santi et al. 2002; Muron 2005; Moretti et al. 2006; Maerten and Maerten 2006; Guzofski et al. 2009; Durand-Riard 2010; Durand-Riard et al. 2013b; Tang et al. 2016). In this approach, internal deformation is not known *a priori*, and the resulting strain is computed from the mechanical behavior of rocks and the applied boundary conditions. Tracking the strain and stress through time gives valuable information on the deformation mechanisms, the potential fracture areas and the possible paleo-geometry. The model is parameterised by elastic properties to mimic the response of rocks to mechanical stresses. The restoration displacement is computed using fundamental laws of motion such as mass conservation and linear momentum conservation, instead of geometric or kinematic rules. In practice, it is done by solving the equation of motion

$$\overline{\nabla} \cdot \overline{\overline{\sigma}} = \overline{f_{ext}} \tag{1.1}$$

where $\overline{\nabla}$ is the del operator, $\overline{f_{ext}}$ is the sum of external forces, and $\overline{\overline{\sigma}}$ is the Cauchy stress tensor. Under the assumption that rocks behave as elastic materials, $\overline{\overline{\sigma}}$ is defined by Hooke's law for elastic motion:

$$\overline{\overline{\sigma}} = \overline{\overline{\overline{\overline{C}}}} : \overline{\overline{\epsilon}}, \tag{1.2}$$

with $\overline{\overline{\overline{\overline{C}}}}$ the elastic fourth-order tensor and $\overline{\overline{\epsilon}}$ the (small-)strain tensor associated to the displacement $\underline{u}$ by

$$\overline{\overline{\epsilon}} = \frac{1}{2}\left[\overline{\nabla}(\overline{u}) + \overline{\nabla}(\overline{u})^T\right]. \tag{1.3}$$

The restoration itself is performed by applying specific boundary conditions to constrain the model (Fig. 1.2). These conditions, usually imposed on the displacement, rely on the following asumptions: the uppermost horizon was flat and horizontal at its deposition time, and it was not faulted. Other conditions can be introduced as complementary geological knowledge, such as direction and scale of deformation, or amount of shortening (Chauvin et al. 2018). Compared to previous methods, it allows the consideration of more physical deformation processes for the sedimental layers, leading to more physical strains inside the restored model. It can also be used to study the deformation history of the model where it is least known, particularly in regions away from the boundaries where the displacement is imposed.

Although these methods offer significant advances in the structural restoration of geological models, they still present many limitations. First, the true mechanical deformation of rocks is highly irreversible and the boundary conditions set to unfold and unfault the medium are often unphysical (Lovely et al. 2012). Moreover, these conditions are shortcuts to the paleo-stress state, hence can be easily questioned (Durand-Riard

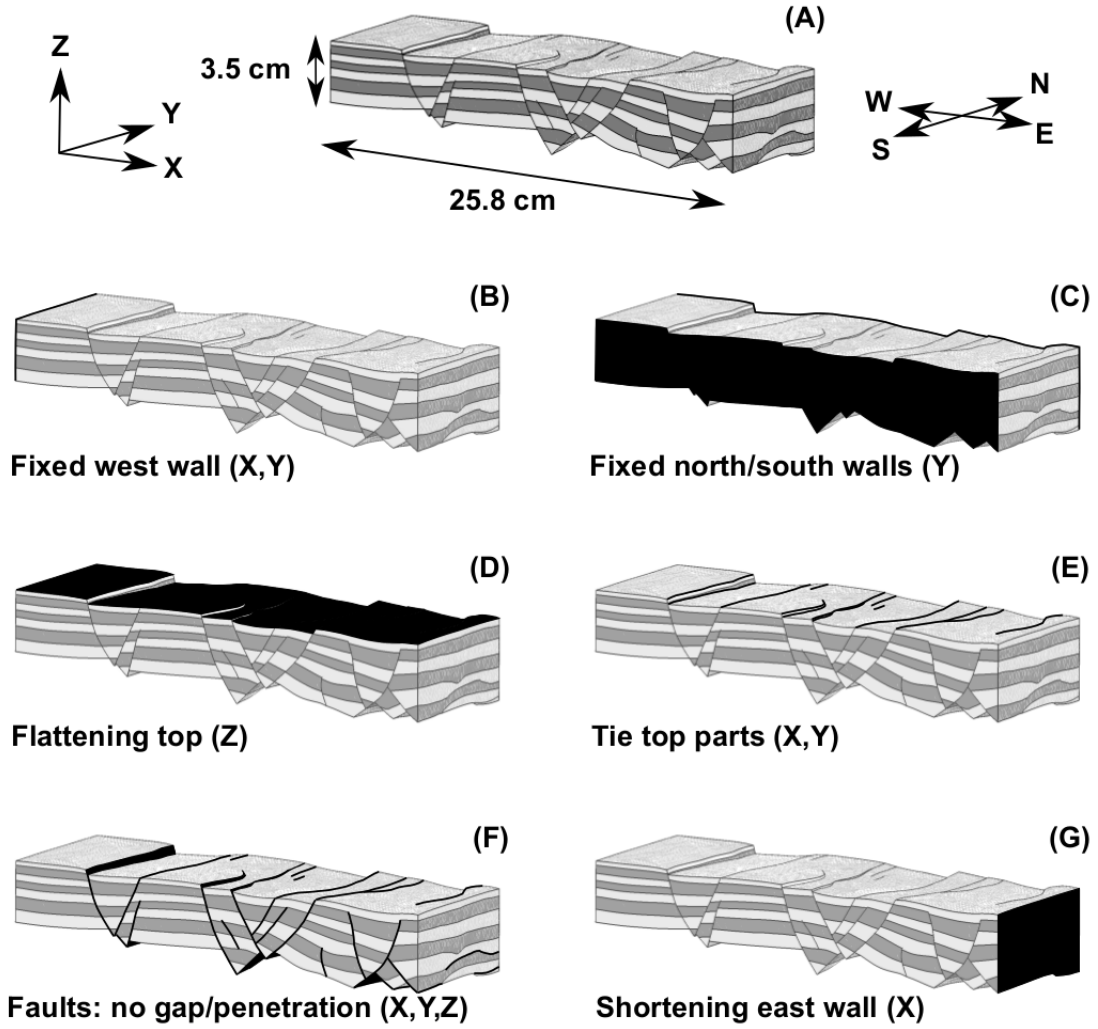

Figure 1.2: Example of boundary conditions used for the geomechanical restoration of a 3D geomodel, from Chauvin (2017). (A) is the 3D geomodel to restore, and (B) to (G) are boundary conditions applied to restore the model.

et al. 2010; Lovely et al. 2012; Durand-Riard et al. 2013a). For example, Durand-Riard et al. (2013b) claims that classical boundary conditions are unable to account for strike-slip and highly oblique-slip faults, and offers two alternatives for a better simulation of faults. The first is to constrain fault motion by using known fault-slip data as piercing points. This, however, implies having sufficient data, which is rarely the case, and can result in unrealistic strain around the constrained points on the fault. The second method is similar to that of Lovely et al. (2012): it constrains fault displacement using the opposite of the forward fault displacement. This was proved to provide an accurate recovery of faults and may yield a strain field more consistent with the forward strain patterns, which cannot be achieved with classical boundary conditions. Nevertheless, geomechanical restoration only considers elastic rock properties so far, neglecting other possible behaviours, such as visco-elasticity or plasticity (Gerbault et al. 1998). Transverse isotropic behaviour also affects results (Durand-Riard et al. 2013a). Moreover, the elastic behavior can only be applied to a model where the internal deformations remain small, which is usually not the case in restoration. These physical issues raise

the question of the capability of geomechanical restoration to properly recover paleo-deformation. There is, therefore, no clear guidelines on which method to choose between geometric and kinematic restoration and geomechanical restoration, despite the benefits of the second one (Maerten and Maerten 2006; Guzofski et al. 2009). Moreover, while it is called geomechanical restoration, it is extensively controlled by geometric considerations: flattening of the top layer and a geometric unfaulting based on stitching the horizon cutoff lines across each fault.

Another issue is the need for a valid volumetric mesh of the structural model, including a boundary representation of the geological domain with the horizons and faults as boundaries (e.g., Muron 2005; Durand-Riard et al. 2010). Such a mesh is difficult to generate, as shown by Pellerin et al. (2014) and Anquez et al. (2016). Since restoration deals with large deformations, this mesh evolves and has to be edited a lot or even rebuilt (Fig. 1.3), limiting the applicability of the geomechanical restoration to be used as a validation tool.

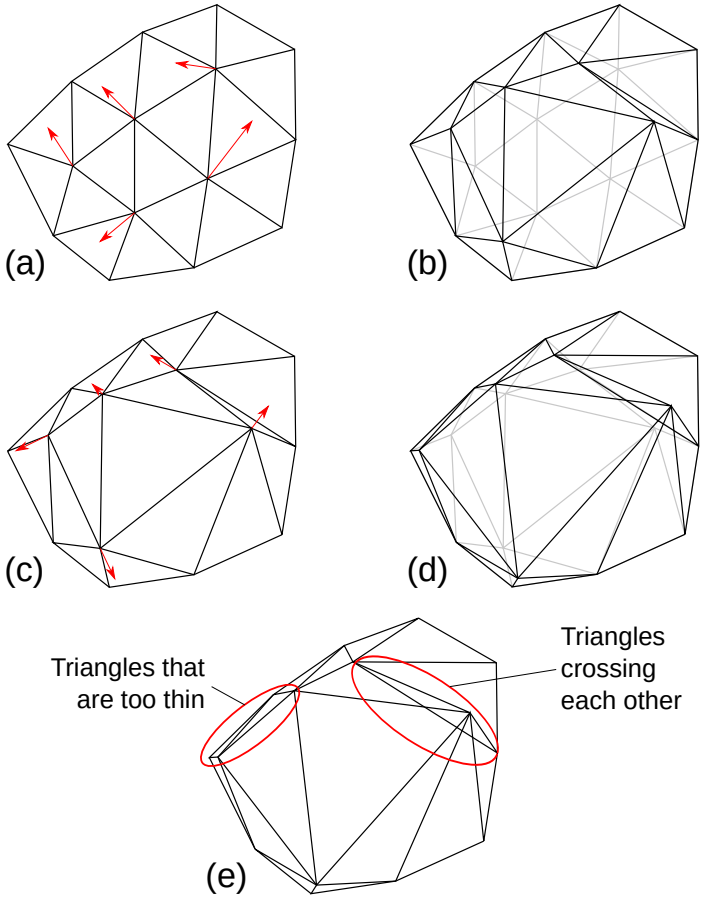

Figure 1.3: 2D synthetic example of how deforming a mesh through time can make it invalid for various computations, implying the need for a remeshing algorithm to be applied. (a) and (b) are the states of a mesh during displacement computation and after, (c) and (d) are the same at the next displacement iteration. (e) shows the problems occurring due to the mesh deformation: invalid crossing triangles and triangles that are too thin for the computation to be accurate on them.

To sum up, geomechanical restoration has overcome some limitations of the "classical" geometric restoration process, but there is substantial need for improvement to

better account for physical processes such as different rheologies, larger deformations, faults, and salt tectonics.

1.3 Stokes flow

While most rocks act as elastic materials when submitted to small deformations and for timescales of a few milliseconds to hundreds of years, they may exhibit a viscous fluid-type behavior when dealing with large deformations that occur at timescales of thousands, millions or more years (Moretti and Froidevaux 1986; Massimi et al. 2006; May et al. 2014; Cornet 2015; May et al. 2015). In particular, rock salt reacts as a viscous fluid when submitted to high stress (Nalpas and Brun 1993; Weijermars et al. 1993; Hudec and Jackson 2007). This has motivated the use of viscous flow simulations to study the evolution of salt structures, as well as other geological processes, both forward and backward in time. Moreover, we show in Appendix 1.A that a creeping flow simulation code can also be used to simulate other rheologies with only a few additional computations.

1.3.1 General equations

The Navier-Stokes equations describing the flow of viscous fluids can, with the incompressibility hypothesis, be written

$$\begin{cases} \overline{\nabla} \cdot \overline{\overline{\sigma}} - \rho \dfrac{\partial \overline{v}}{\partial t} - \rho(\overline{v} \cdot \overline{\nabla})\overline{v} = \overline{f} \\ \overline{\nabla} \cdot \overline{v} = 0 \end{cases} \tag{1.4}$$

where $\overline{\nabla}$ is the del operator, $\overline{\overline{\sigma}}$ is the stress tensor, ρ is the density, $\overline{f}$ is the specific body force (usually the volume weight $-\rho\overline{g}$), and $\overline{v}$ is the velocity. The stress consists of a deviatoric part $\overline{\overline{\tau}}$, and an isotropic pressure p:

$$\overline{\overline{\sigma}} = \overline{\overline{\tau}} - p\overline{\overline{I}}, \tag{1.5}$$

where $\overline{\overline{I}}$ is the identity tensor. In the viscous flow assumption, the deviatoric part of the stress is

$$\overline{\overline{\tau}} = 2\eta\overline{\overline{D}}, \tag{1.6}$$

with η the dynamic viscosity and $\overline{\overline{D}}$ the infinitesimal strain rate tensor defined by

$$\overline{\overline{D}} = \frac{1}{2}\left[\overline{\nabla}(\overline{v}) + \overline{\nabla}(\overline{v})^{\mathrm{T}}\right]. \tag{1.7}$$

Assembling Eq. (1.4), (1.5), (1.6) and (1.7), the Navier-Stokes equations can be written

$$\begin{cases} \overline{\nabla} \cdot \left[\eta(\overline{\nabla}\overline{v} + (\overline{\nabla}\overline{v})^{\mathrm{T}})\right] - \overline{\nabla}p - \rho \dfrac{\partial \overline{v}}{\partial t} - \rho(\overline{v} \cdot \overline{\nabla})\overline{v} = -\rho\overline{g} \\ \overline{\nabla} \cdot \overline{v} = 0 \end{cases} \tag{1.8}$$

The materials we deal with here are highly viscous, and we observe their deformation over thousands to millions of years. Let us do a dimensional analysis of the different parameters of the equation (Massimi et al. 2006). The following reference values for

density and viscosity are reasonable for sedimentary rocks:

$$\widetilde{\eta} = 10^{17} \text{ Pa.s}, \quad \widetilde{\rho} = 2 \times 10^{3} \text{ kg.m}^{-3}.$$

For the reference timescale and characteristic length of the models we work with, we take

$$T = 1 \text{ Ma} \simeq 3.15 \times 10^{13} \text{ s}, \quad L = 1000 \text{ m},$$

which scales the pressure and velocity by

$$P = \widetilde{\rho} g L = 1.962 \times 10^{7} \text{ Pa} \quad \text{and} \quad V = \frac{L}{T} = 3.18 \times 10^{-11} \text{ m.s}^{-1}.$$

We can then consider the non-dimensional quantities

$$\widetilde{t} = \frac{t}{T}, \quad \widetilde{x} = \frac{x}{L}, \quad \widetilde{p} = \frac{p}{P} \quad \text{and} \quad \widetilde{v} = \frac{v}{V} = v\frac{T}{L}$$

respectively for the time, space, pressure and velocity. In order to use them, the time and space derivatives also need rescaling such as

$$\frac{\partial}{\partial t} = \frac{1}{T}\frac{\partial}{\partial \widetilde{t}} \quad \text{and} \quad \widetilde{\nabla} = \frac{1}{L}\widetilde{\nabla}.$$

Writing Eq. (1.8) with those non-dimensional quantities, we obtain

$$\begin{cases} \left(\dfrac{\widetilde{\eta}}{LT}\right)\widetilde{\nabla}\cdot\left[\widetilde{\nabla}\widetilde{v} + (\widetilde{\nabla}\widetilde{v})^{\mathrm{T}}\right] - (\widetilde{\rho} g)\widetilde{\nabla}\widetilde{p} - \left(\widetilde{\rho}\dfrac{L}{T^2}\right)\dfrac{\partial \widetilde{v}}{\partial \widetilde{t}} - \left(\widetilde{\rho}\dfrac{L}{T^2}\right)(\widetilde{v}\cdot\widetilde{\nabla})\widetilde{v} = -\widetilde{\rho} g \\ \dfrac{1}{T}\widetilde{\nabla}\cdot\widetilde{v} = 0 \end{cases} \tag{1.9}$$

At this point, we can introduce the *Reynolds* and *Froude* non-dimensional numbers associated to this dimensional analysis

$$Re = \frac{\widetilde{\rho} V L}{\widetilde{\eta}} = \frac{\widetilde{\rho} L^2}{\widetilde{\eta} T} \quad \text{and} \quad Fr = \frac{V}{\sqrt{gL}} = \frac{\sqrt{L}}{T\sqrt{g}}$$

which represent, respectively, the ratio between the inertial and viscous forces, and the ratio between buoyancy and inertial forces. Equation (1.9) can then be rewritten to

$$\begin{cases} \dfrac{1}{Re}\widetilde{\nabla}\cdot\left[\widetilde{\nabla}\widetilde{v} + (\widetilde{\nabla}\widetilde{v})^{\mathrm{T}}\right] - \dfrac{1}{Fr^2}\widetilde{\nabla}\widetilde{p} - \dfrac{\partial \widetilde{v}}{\partial \widetilde{t}} - (\widetilde{v}\cdot\widetilde{\nabla})\widetilde{v} = -\dfrac{1}{Fr^2}\dfrac{1}{g} g \\ \widetilde{\nabla}\cdot\widetilde{v} = 0 \end{cases} \tag{1.10}$$

In our case, the value of the *Froude* and *Reynolds* numbers are

$$Re \simeq 6.35 \times 10^{-22} \quad \text{and} \quad Fr \simeq 3.21 \times 10^{-13}$$

so the inertial parts of the Navier-Stokes equations can be neglected. This justifies the

use of a simplified form of Eq. (1.8), also called Stokes equations:

$$\begin{cases} \overline{\nabla} \cdot \left[\eta(\overline{\nabla}\overline{v} + (\overline{\nabla}\overline{v})^{\mathrm{T}})\right] - \overline{\nabla}p = -\rho\overline{g} \\ \overline{\nabla} \cdot \overline{v} = 0 \end{cases} \tag{1.11}$$

Neglecting the inertial term removes time from the equations, which means Eq. (1.11) describe a steady-state flow, and their resolution provides the velocity of a fluid at a specific position and time. When different fluids are present, the conditions that are applied at their boundaries, as well as their differences in density, can create instabilities such as Rayleigh-Taylor instabilities. These instabilities make the flow non-stationary as they advect the viscosity and density fields in time. In numerical schemes, this advection is carried out in a discretized way, at the end of each time step. The simplest way to do it is by using an Euler scheme, the position $\overline{x}(t + \Delta t)$ of each point of the material model after a time step Δt being computed as

$$\overline{x}(t + \Delta t) = \overline{x}(t) + \overline{v}(t) \cdot \Delta t, \tag{1.12}$$

with $\overline{x}(t)$ the position and $\overline{v}(t)$ the computed velocity of the point at time t. While higher-order methods exist (e.g., Ismail-Zadeh and Tackley 2010), particularly to stabilize the advection scheme in the case of large time steps, we choose to present the concept with this one for simplicity. This Finite-Difference approximation relies on the idea that if the chosen time step Δt is small enough, we can approximate the velocity of a particle as a constant over this time step (Δt is usually calculated using a Courant-Friedrichs-Lewy (CFL) condition (Courant et al. 1928) to ensure it).

1.3.2 Application to restoration

The idea of a restoration method based on creeping flow was introduced at the EGS General Assembly in Hague in 1999 and later published in Ismail-Zadeh et al. (2004a). It was introduced as a way to improve the restoration of salt structures. Indeed, salt rock is less dense than most sedimental rocks, and behaves as a viscous fluid over geological timescales (Nettleton 1934; Woidt 1978; Poliakov et al. 1996). As such, salt layers form Rayleigh-Taylor instabilities with their overburdens, which can lead to salt structures taking a wide variety of shapes depending on the environment (Jackson and Hudec 2017). In particular, factors such as the type of overburden, the position and rate of erosion and deposition of sediments over it, the tilt of the depositional surface or the tectonic setting can have a large impact on salt flow and the resulting structures (e.g., Zaleski and Julien 1992; Podladchikov et al. 1993; Poliakov et al. 1996). This rheology and wide variety of complicated shapes make the conservation of layer area and thickness unable to perform restoration on models where salt has a large role. In this context, considering rocks as highly vicous fluids in a restoration scheme can, not only hold more physical results, but allow the restoration of some models to make more geological sense. Moreover, as said in the previous subsection, Stokes equations describe a steady-state flow where time appears only in the application of the velocity to the density and viscosity fields. As the computation of the velocity does not depend on previous times (contrarily to elasticity constraints which depend on previous strain), the advection can be applied with a negative time. This is the basis of backward

time stepping restoration schemes: during the numerical advection, instead of applying Eq. (1.12) at each time step, one can advect the points of the material model with

$$\overline{x}(t - \Delta t) = \overline{x}(t) - \overline{v}(t) \cdot \Delta t, \tag{1.13}$$

like in Fig. 1.4.

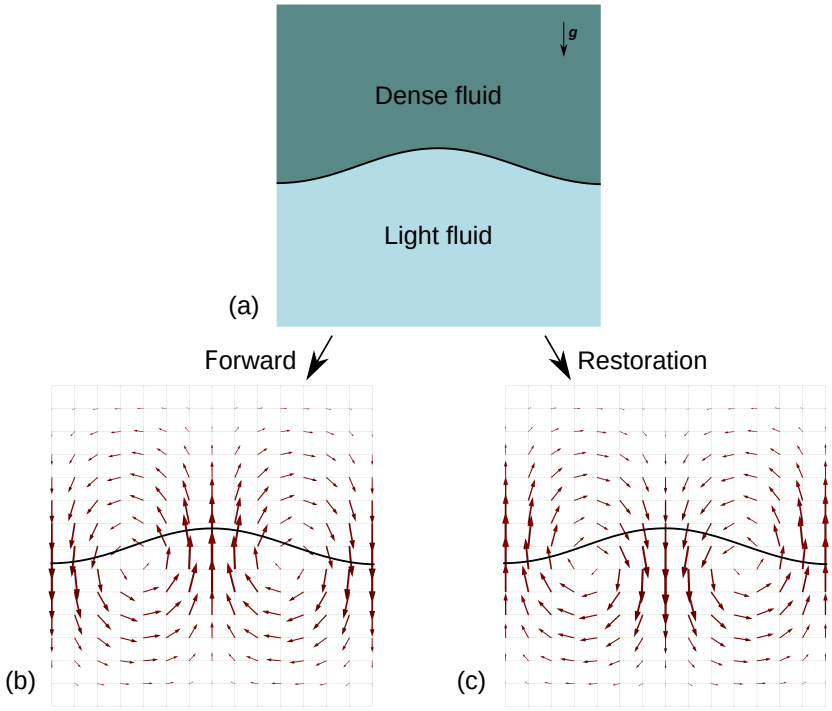

Figure 1.4: Example of the restoration scheme for a simple setup (a): as the arrows in (b) represent the velocity computed at a specific time step for a forward scheme, the advection of the material model in a restoration scheme is done with the opposite of the computed velocity, shown in (c).

In this light, representing the mechanical behavior of geological materials with viscous fluids holds several advantages, such as the use of 'natural' boundary conditions, like a free surface on top, and the account of rheologies like salt layers.

The first creeping flow restoration implementations used a linear viscous (Newtonian) rheology, and proved to be able to restore 2D seismic cross-sections of salt diapirs (along with a backstripping method for the sedimentation processes, see Fig. 1.5) (Ismail-Zadeh et al. 2001) and 3D Rayleigh-Taylor instabilities (Kaus and Podladchikov 2001; Ismail-Zadeh et al. 2004c). They were also used in the restoration of mantle thermal behaviors (e.g., Ismail-Zadeh et al. 2004b; Korotkii and Tsepelev 2007; Ismail-Zadeh et al. 2016). Since then, the method has been used for 3D unfolding in the absence of gravity (e.g., Schmalholz 2008), extended to non-linear (power-law) viscous behavior (e.g., Lechmann et al. 2010; Fernandez 2014) (Fig. 1.6), or used to study the reverse modeling of flanking structures (e.g., Kocher and Mancktelow 2005). Overall, this approach has proven to allow the unfolding of sediment layers and the restoration of salt structures, both in 2D and in 3D. In the various previous applications, however, faults are either not present, not taken into account in the restoration process, or simply

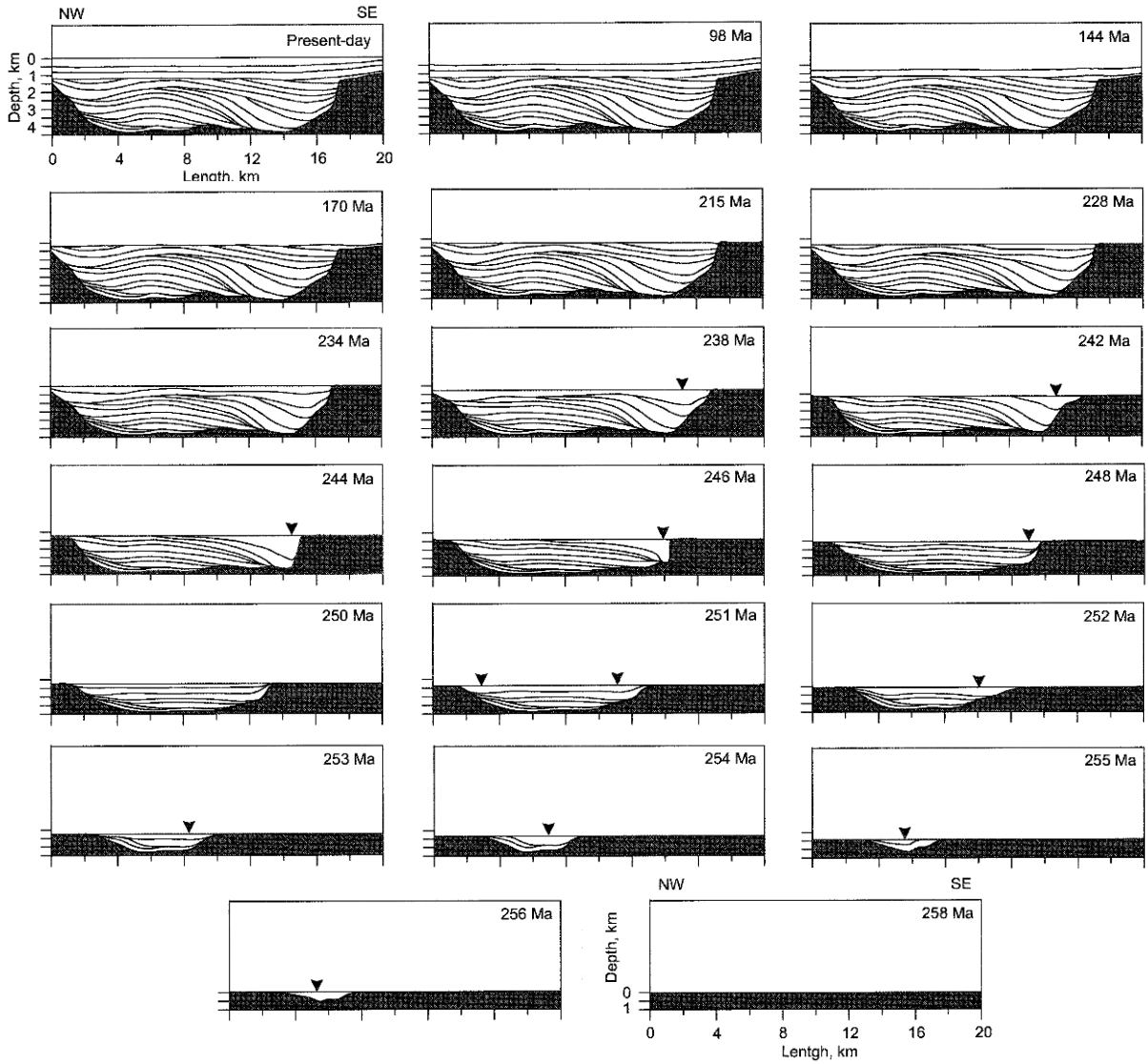

Figure 1.5: Example of the restoration of a cross-section using viscous restoration for the salt layer along with backstripping for the sediment layers. The boundary conditions are set to free slip for the top and lateral boundaries, and no slip for the bottom boundary. Images taken from Ismail-Zadeh et al. (2001).

considered as frictionless surfaces. Also, the top surface in contact with air stays flat during the restoration process as the sedimentation and erosion processes are mostly considered fast enough to flatten the arising topography.

1.4 Numerical methods

In order to perform creeping flow restoration on geological models, one needs to solve the Stokes equations Eq. (1.11) in models where the velocity field evolves in time. However, there is usually no analytical solution for these equations in the studied models, due to their complexity. The solution then has to be approximated. In order to have enough precision and to deal with very large models, this is usually done numerically. The

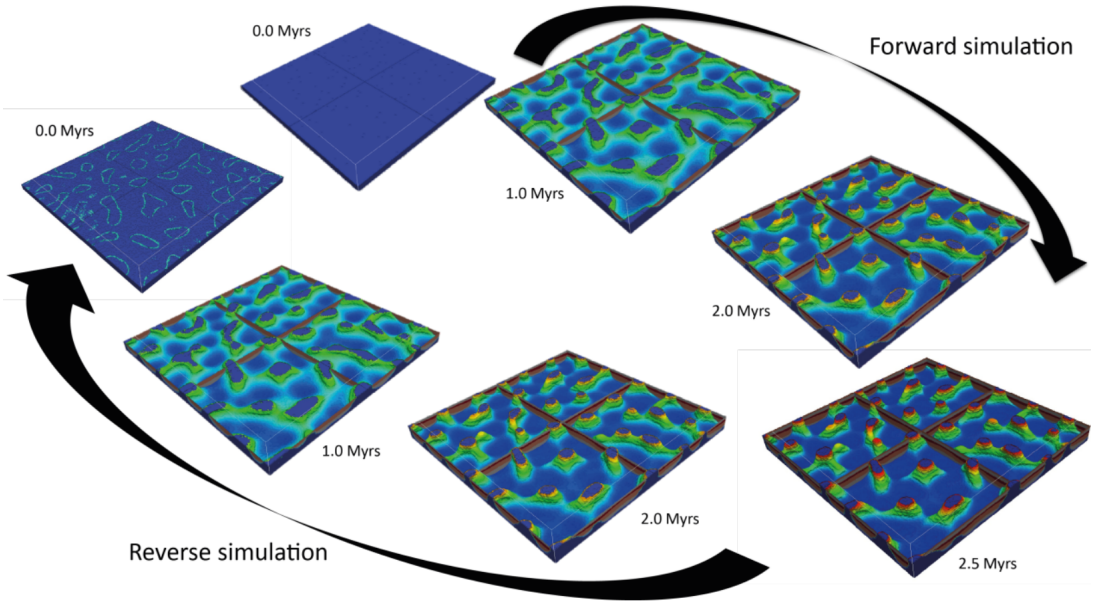

Figure 1.6: Example of the restoration from Fernandez (2014), showing the restoration of a 3D forward simulation including downbuilding.

model is then discretized on a set of points with a prescribed connectivity, and the solution of the Stokes equations is approximated using methods such as the FEM or FDM.

1.4.1 Material representations

The geomechanical simulation of a specific domain requires to choose an appropriate kinematic description to follow the displacement inside the geological layers. In order to discretize the physical reality and solve a mechanical problem numerically, different representations exist. In this subsection, I review some of these representations and the advantages and limits associated with each of them.

1.4.1.1 The Lagrangian and Eulerian frames

There are two main frames for describing a physical phenomenon: the Eulerian frame of reference, also known as the spatial description, and the Lagrangian frame of reference, also known as the material description (e.g., Cornet 2015).

Let us consider a body B and a particle p inside it. We consider their respective position $\overline{B}_0$ and $\overline{x}_0$ at time $t = 0$, and $\overline{B}$ and $\overline{x}$ at time t. The Lagrangian representation of the body B would be a function $\overline{\chi}$ that gives the position $\overline{x}$ of any particle at time t as a function of its position at time $t = 0$: $\overline{x} = \overline{\chi}(\overline{x}_0, t)$. This representation is generally used in solid mechanics, where the paths of the particles are of interest. In the Eulerian description, the movement of the particles is evaluated at several fixed positions $\overline{x}_i$. As time passes, different particles occupy points $\overline{x}_i$, and the objective is to describe the motion, or the temperature, or any feature of the particles at points $\overline{x}_i$. The initial position of the particle that occupies point $\overline{x}$ at time t is then $\overline{x}_0 = \overline{\chi}^{-1}(\overline{x}, t)$ (cf Fig. 1.7). This description is commonly used in fluid dynamics.

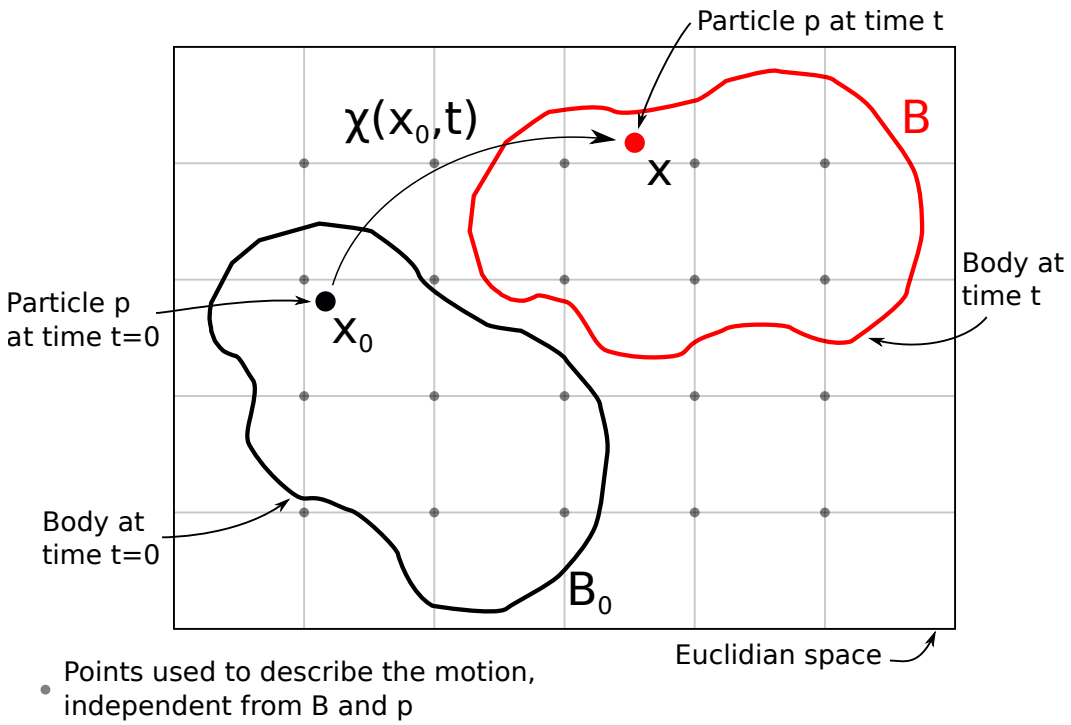

Figure 1.7: Lagrangian and Eulerian descriptions to study the motion: the Eulerian space is fixed, and the motion is evaluated at points independent of the studied body. The Lagrangian description studies the path χ of the particles that constitute the studied body.

The Eulerian methodology is based on a fixed mesh on the whole domain in study, so it can implement accurate and efficient computation of displacements in a geological model (e.g., Deubelbeiss and Kaus 2008; Braun et al. 2008). However, Eulerian methods leave no trace of the movement of particles, so discontinuities such as faults, horizons or other moving surfaces cannot be tracked through time, which is critical when dealing with large deformations. The material properties are also not tracked directly, so their value at the nodes of the mesh can become unaccurate and the computation of the velocity from the Stokes equations loses accuracy after a few time steps.

The Lagrangian approach, on the other hand, incorporates the interfaces, material properties and geometric description by tracking the reference configuration at each step (e.g., Podladchikov et al. 1993; Mello and Henderson 1997; Ismail-Zadeh et al. 2001; Massimi et al. 2006). In this approach, a trace of the path followed by the points of the model can be kept. However, repeated application of mesh movements when the model evolves and particles are displaced may lead to bad quality or even invalid mesh. Since the error in any computation performed in a mesh is linked to its quality, in order to keep the error as low as possible, one then needs remeshing at some time steps, which requires significant efforts. In large deformations, remeshing may even be needed at each time step. To relax such an effort, some methods have been developed to mitigate the loss of numerical precision due to mesh distortion in large deformation simulations (Braun and Sambridge 1994, 1995), but they are limited to 2D simulations where the mesh is a Delaunay triangulation.

When dealing with large deformations of geological models, neither of these two

representations is well adapted, since one needs both the Lagrangian ability to keep track of the material properties and interfaces, and the Eulerian precision and absence of remeshing in case of large displacement. This is why methods mixing the two approaches have been developed when dealing with creeping flow models involving large strains.

1.4.1.2 The Arbitrary Lagrangian Eulerian representation

A notable mix of the two previous frames is the Arbitrary Lagrangian Eulerian (ALE) formulation (Hughes et al. 1981; Fullsack 1995). This method has been developed to overcome the limitations of the Eulerian and Lagrangian formulations by inheriting features from both methodologies. It has often been used in geomechanical simulations involving creeping flow phenomena such as mantle flow simulations. It has had various formulations and implementations, in 2D [Willett et al. (1993); Fullsack (1995); Poliakov et al. (1996); Gemmer et al. (2004); Massimi et al. (2007); Fillon et al. (2013)] and more recently in 3D [Braun (2003); Braun et al. (2008); Braun and Yamato (2010); Ismail-Zadeh et al. (2004c); Thieulot et al. (2014)].

Most of these methods rely on keeping track of the material model in a Lagrangian way, while computing the displacement or the velocity on a Eulerian mesh. Contrarily to the Eulerian frame, however, in the ALE formulation, the Eulerian mesh has an arbitrary velocity and can be deformed. This is particularly interesting to follow specific surfaces inside the computational domain and better account for the material model at interfaces with high contrasts of properties. In particular, allowing for moving interfaces enables the use of free surfaces, moving boundaries or internal interfaces. Since the computational Eulerian mesh is independent of the Lagrangian material, it can be done while keeping deformation inside the computational domain to a minimum. Erosion and deposition of mass is also simplified. Indeed, the Eulerian mesh can easily be deformed on its outer shape in the ALE formulation (e.g., Braun 2003; Thieulot 2011), whereas in the Lagrangian approach it would imply removing or creating mesh elements at each time step.

Depending on the mechanical simulation, the implementation varies as the quantities that need to be tracked are not the same. Lagrangian nodes can be used to track interfaces through time, by advecting them at each time step from the velocity computed on the Eulerian mesh. These Lagrangian interfaces can then be used for the interpolation of material properties on the Eulerian mesh. The Eulerian mesh can also be modified to better fit some of them, for example by deforming the Eulerian mesh so its nodes fit the tracked interfaces (e.g., Fullsack 1995; Gemmer et al. 2004), or by using adaptive mesh refinement (e.g., Braun et al. 2008; Bangerth et al. 2019) (Fig. 1.8). In some other implementations, no internal tracking is done and the Lagrangian part of the code is there only to deform the Eulerian mesh boundaries, to account for a free surface at the top and possibly a movement condition on the sides of the model (Fig. 1.9) (e.g., Gemmer et al. 2004; Thieulot et al. 2014). This is particularly useful in mechanical simulations of the mantle, where the viscosity and density of the materials don't need to be tracked as they depend mainly on the temperature field, which can be computed at each time step by solving the heat equation on the Eulerian mesh.

When using a Lagrangian frame to track the material model, the material parameters need to be transfered from the Lagrangian frame to the Eulerian mesh nodes at

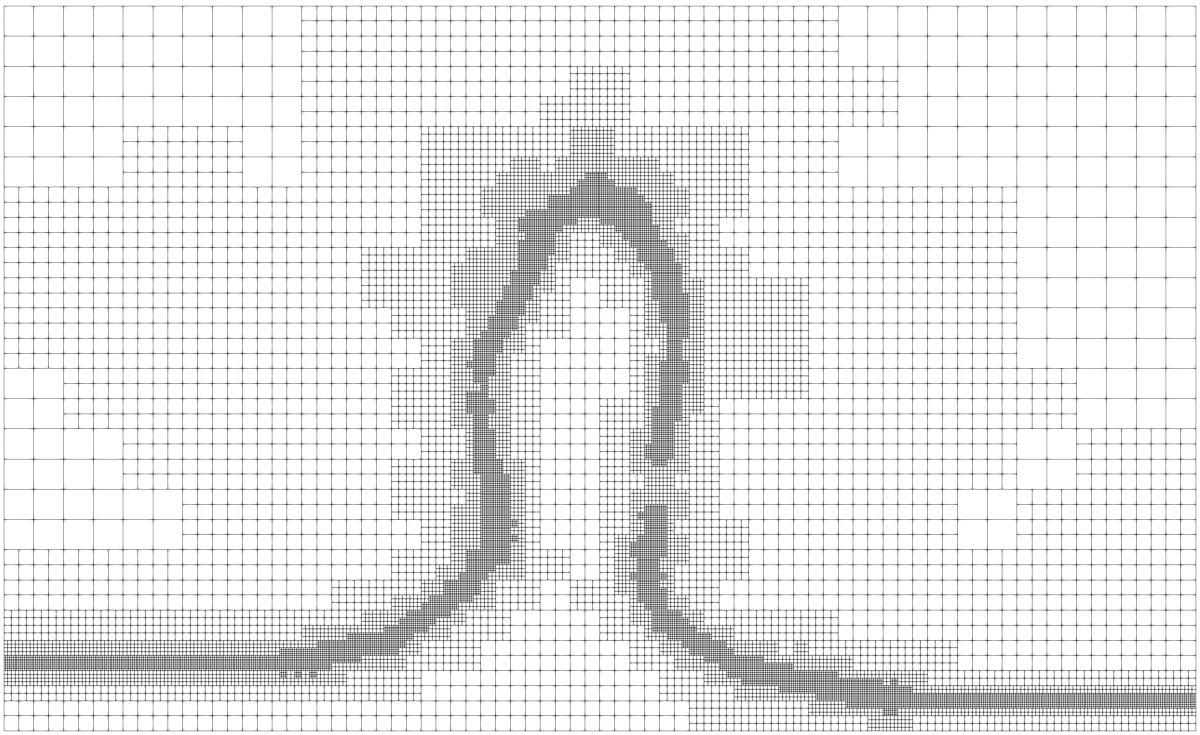

Figure 1.8: Example of an adaptively refined Eulerian grid used to better account some of the interfaces in a model.

each time step. The Lagrangian mesh can then be heavily distorted, as long as it is valid. The other way around, the velocity needs to be interpolated on the Lagrangian nodes to advect them. As mentionned above, the Eulerian mesh can move as well. Although it implies additional computation, tracking precisely the interfaces while minimizing the need for a remeshing of the Lagrangian mesh make this method valuable for geomechanical simulations with very large deformations, compared to the Eulerian or Lagrangian methods.

1.4.1.3 The PIC method

There are several alternatives to relying on a mesh for the Lagrangian description, mostly using particles to describe the changes in material parameters. These particles can be used either to track the interfaces between rock layers, as in the marker chain method (e.g., Woidt 1978; van Keken et al. 1997), or to track the material properties in the domain, as in the Particle-In-Cell (PIC) method (e.g., Christensen and Hofmann 1994; Sulsky et al. 1994; Moresi et al. 2003; Asgari and Moresi 2012; Gassmöller et al. 2018). This method, also known as the Material Point Method (MPM), discretizes the domain of interest with a set of nodes or particles, each having a domain of influence around it. Depending on the implementation, those particles are either used to interpolate the material properties on a computational grid where the motion equations are solved, or used directly to define the shape functions in their domain of influence (Renaudeau et al. 2019). The main advantage of the method is that the particles are

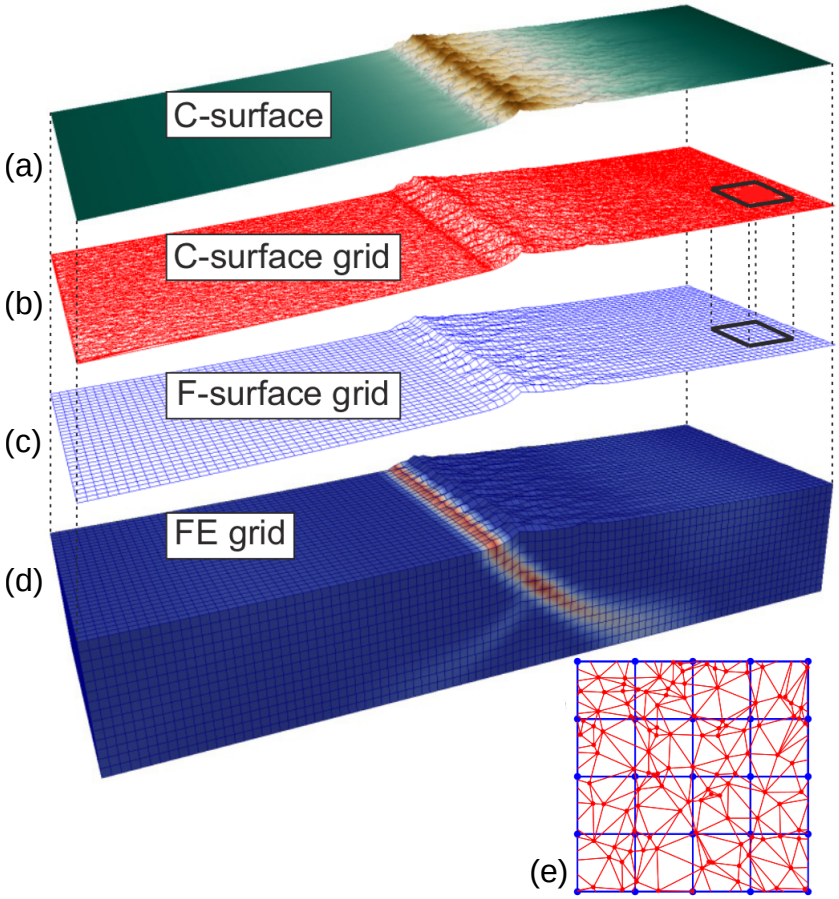

Figure 1.9: Example of an ALE implementation where the cells of the Eulerian FE grid (d) are only deformed upwards to follow the top surface (a). Numerically, this is done by deforming the top surface mesh (b) and interpolating the new position of the top grid nodes (c) on it. (e) shows a close-up view on the superposition of (b) and (c). Taken from Thieulot et al. (2014).

not treated as a mesh with a prescribed connectivity, removing the problem of mesh entanglement and allowing an easier treatment of large deformations. Remeshing issues also vanish, and there is no need to track exact material interfaces, since each particle carries its own constitutive properties. The method can also be parallelized quite easily, since the particle swarm can be divided among the CPUs along with the computational grid (e.g., Gassmöller et al. 2018). While it needs additional verifications to transfer the particles to other parts of the domain during their advection, it considerably simplifies the tracking of material properties. One of the issues of the method is that the interfaces are not available directly. They can, however, be interpolated from the position of the particles on each side of them. Because the particle swarm needs to be dense enough to provide precise interpolation of the material properties, the interpolation of the interfaces can be quite precise as well. Refinement of the model can also be easily obtained by simply adding points in the regions of interest (Liu et al. 2004; Renaudeau et al. 2019). Although they imply relatively high computational cost (due to the high number of particles needed), and a more irregular pattern of the sparsity, their abstraction from meshes make the PIC methods efficient for implementing the computation of

large deformations in geological models using creeping flow equations.

Another advantage of using particles is the ease of including averaging methods during the interpolation of properties to the computation grid. Indeed, when doing physical simulations on geological models, large jumps in viscosity and density (up to several orders of magnitude in the case of viscosity) occur. These jumps lead to very long computation times (because of numerical instabilities in solvers and preconditioners), and can cause over- and undershoots in the numerical approximation of the pressure gradient (Deubelbeiss and Kaus 2008; Thielmann et al. 2014; Heister et al. 2017). Averaging the viscosity and density of the particles when interpolating them on the computation grid mitigates the effect of these jumps.

1.4.2 The FEM method

1.4.2.1 Principle

The Finite Element Method (FEM) is a mathematical method to approximate the solution of partial differential equations. It relies on discretizing the physical domain into a set of elements, such as a grid or a mesh. The partial differential equations are then solved locally on each element, and the global solution is obtained by combining all the elementary solutions (Hughes 2012).

The finite element method regroups a large number of numerical methods, depending on the type of elements that is chosen, the functions used to approximate the field of interest, or the solver of the linear system resulting from the FE discretization. All those methods, however, involve the same steps:

- The domain of interest is subdivided into a set of elements (called mesh).
- The partial differential equations are converted from their "strong form" to a "weak form" as an integral over the domain of interest.
- The weak form integral equation is discretized on each element of the mesh.
- The functional space is discretized on a set of functions to approximate the solution to the weak form on each element.
- A change of variable is operated: each element is mapped to a reference element where the problem solution is trivial.
- In each element, solving the discretized weak form integral equation comes down to solving a matrix system depending on the neighbour elemental nodes.
- The elemental matrix equations are combined into a single linear system for the whole domain. This step is called the assembly.
- Finally, a solver is used to compute the solution of the linear system.

1.4.2.2 Application to the resolution of Stokes equations

The following subsection summarizes some specificities of applying the FEM to the Stokes equations. It builds from Thieulot (2019) and the tutorials and lectures available with the deal.II library (Bangerth et al. 2007; Arndt et al. 2019).

- **Obtaining the weak form**

In the case of the Stokes equations, the strong form of the equation is given by Eq. (1.11). We can write it in vector form as

$$\begin{pmatrix} -\overline{\nabla}\cdot\left(2\eta\overline{\overline{D}}(\overline{v})\right)+\overline{\nabla}p \\ -\overline{\nabla}\cdot\overline{v}\end{pmatrix}=\begin{pmatrix}\rho\overline{g}\\0\end{pmatrix}. \tag{1.14}$$

Multiplying by a vector-valued test function $\varphi=\begin{pmatrix}\overline{w}\\q\end{pmatrix}$ and integrating over the domain Ω, the equation becomes

$$\int_\Omega \overline{w}\cdot\left(\overline{\nabla}\cdot\left(-2\eta\overline{\overline{D}}(\overline{v})\right)+\overline{\nabla}p\right)d\Omega-\int_\Omega q\ \overline{\nabla}\cdot\overline{v}\ d\Omega=\int_\Omega\overline{w}\cdot\rho\overline{g}\ d\Omega, \tag{1.15}$$

which is true for every test function $\varphi=\begin{pmatrix}\overline{w}\\q\end{pmatrix}$. Integrating by parts the second term of the first integral, we obtain

$$\int_\Omega \overline{w}\cdot\left(\overline{\nabla}\cdot\left(-2\eta\overline{\overline{D}}(\overline{v})\right)\right)d\Omega+\int_\Gamma\overline{n}\cdot\overline{w}\ p\ d\Gamma-\int_\Omega\overline{\nabla}\cdot\overline{w}\ p\ d\Omega \\ -\int_\Omega q\ \overline{\nabla}\cdot\overline{v}\ d\Omega=\int_\Omega\overline{w}\cdot\rho\overline{g}\ d\Omega. \tag{1.16}$$

with $\overline{n}$ the unitary vector normal to the boundary $\Gamma=\partial\Omega$ of the domain Ω. After integrating by parts the first integral term, we obtain

$$-\int_\Gamma(\overline{n}\otimes\overline{w}):\left(2\eta\overline{\overline{D}}(\overline{v})\right)d\Gamma+\int_\Omega\overline{\nabla}(\overline{w}):\left(2\eta\overline{\overline{D}}(\overline{v})\right)d\Omega \\ +\int_\Gamma\overline{n}\cdot\overline{w}\ p\ d\Gamma-\int_\Omega\overline{\nabla}\cdot\overline{w}\ p\ d\Omega-\int_\Omega q\ \overline{\nabla}\cdot\overline{v}\ d\Omega=\int_\Omega\overline{w}\cdot\rho\overline{g}\ d\Omega \tag{1.17}$$

This equation can be rewritten by considering the bilinear form integrals $(\cdot\,,\cdot)_\Omega$, $(\cdot\,,\cdot)_\Gamma$ over Ω and Γ:

$$-\left(\overline{n}\otimes\overline{w},2\eta\overline{\overline{D}}(\overline{v})\right)_\Gamma+\left(\overline{\nabla}(\overline{w}),2\eta\overline{\overline{D}}(\overline{v})\right)_\Omega+(\overline{n}\cdot\overline{w},p)_\Gamma-\left(\overline{\nabla}\cdot\overline{w},p\right)_\Omega \\ -\left(q,\overline{\nabla}\cdot\overline{v}\right)_\Omega=(\overline{w},\rho\overline{g})_\Omega \tag{1.18}$$

Since $\overline{\overline{D}}(\overline{v})$ is a symmetric tensor, its scalar product with a general tensor such as $\overline{\nabla}(\overline{w})$ is equal to the scalar product of the symmetrized forms of the two, and we can write the weak form of the Stokes equations:

$$\left(\overline{\overline{D}}(\overline{w}),2\eta\overline{\overline{D}}(\overline{v})\right)_\Omega-\left(\overline{\nabla}\cdot\overline{w},p\right)_\Omega-\left(q,\overline{\nabla}\cdot\overline{v}\right)_\Omega \\ -\left(\overline{n}\otimes\overline{w},2\eta\overline{\overline{D}}(\overline{v})\right)_\Gamma+(\overline{n}\cdot\overline{w},p)_\Gamma=(\overline{w},\rho\overline{g})_\Omega \tag{1.19}$$

for all test functions $\overline{w}$ and q. One of the specificities of the weak form is that its solution is the same as the strong form solution $\overline{v}\in\mathbf{V}=\{\varphi\colon\Omega\to\mathbb{R}^3|\varphi\in H^1(\Omega)|\varphi_{\Gamma_D}=\overline{v}_D\}$ and $p\in Q=L^2$ where Γ_D is the part of the boundaries where Dirichlet conditions are

imposed. This solution holds in particular for all test functions $\overline{w} \in \mathbf{V}_0 = \{\varphi \colon \Omega \to \mathbb{R}^3 | \varphi \in H^1(\Omega) | \varphi_{\Gamma_D} = 0\}$ and $p \in Q$.

- **Applying boundary conditions**

When subdividing the boundaries into Dirichlet and Neumann parts Γ_D and Γ_N, we have $\overline{w} = 0$ on Γ_D, so

$$-\left(\overline{n} \otimes \overline{w}, 2\eta\overline{\overline{D}}(\overline{v})\right)_{\Gamma_D} + (\overline{n} \cdot \overline{w}, p)_{\Gamma_D} = 0 \tag{1.20}$$

and on the rest of the boundary Γ_N, the boundary terms can be re-written as:

$$\begin{aligned}
-\left(\overline{n} \otimes \overline{w}, 2\eta\overline{\overline{D}}(\overline{v})\right)_{\Gamma_N} + (\overline{n} \cdot \overline{w}, p)_{\Gamma_N} &= \sum_{i,j=1}^{dim} -\left(n_i w_j, 2\eta\overline{\overline{D}}(\overline{v})_{ij}\right)_{\Gamma_N} + \sum_{i=1}^{dim} (n_i w_i, p)_{\Gamma_N} \\
&= \sum_{i,j=1}^{dim} -\left(n_i w_j, 2\eta\overline{\overline{D}}(\overline{v})_{ij}\right)_{\Gamma_N} + \sum_{i,j=1}^{dim} (n_i w_j, p\delta_{ij})_{\Gamma_N} \\
&= \sum_{i,j=1}^{dim} \left(n_i w_j, p\delta_{ij} - 2\eta\overline{\overline{D}}(\overline{v})_{ij}\right)_{\Gamma_N} \\
&= \left(\overline{n} \otimes \overline{w}, p\overline{\overline{I}} - 2\eta\overline{\overline{D}}(\overline{v})\right)_{\Gamma_N} \\
&= \left(\overline{w}, \overline{n} \cdot \left[p\overline{\overline{I}} - 2\eta\overline{\overline{D}}(\overline{v})\right]\right)_{\Gamma_N}.
\end{aligned} \tag{1.21}$$

Since the traction on the Neumann boundary can be defined as

$$\overline{h}_N = \overline{n} \cdot \left[p\overline{\overline{I}} - 2\eta\overline{\overline{D}}(\overline{v})\right], \tag{1.22}$$

the weak form of the Stokes equations can be written

$$\left(\overline{\overline{D}}(\overline{w}), 2\eta\overline{\overline{D}}(\overline{v})\right)_{\Omega} - \left(\overline{\nabla} \cdot \overline{w}, p\right)_{\Omega} - \left(q, \overline{\nabla} \cdot \overline{v}\right)_{\Omega} = (\overline{w}, \rho\overline{g})_{\Omega} - \left(\overline{w}, \overline{h}_N\right)_{\Gamma_N} \tag{1.23}$$

- **Discretization**

Since it is not possible to compute the exact solution in an infinite function space, the FEM relies on computing an approximation of the solution by discretizing the equations on a finite dimensional space. The problem then becomes: find $\overline{v}^s \in \mathbf{V}^s$, $p^s \in Q^s$, with $\mathbf{V}^s$ and Q^s finite dimensional subspaces of $\mathbf{V}$ and Q, so that

$$\left(\overline{\overline{D}}(\overline{w}^s), 2\eta\overline{\overline{D}}(\overline{v}^s)\right)_{\Omega} - \left(\overline{\nabla} \cdot \overline{w}^s, p^s\right)_{\Omega} - \left(q^s, \overline{\nabla} \cdot \overline{v}^s\right)_{\Omega} = (\overline{w}^s, \rho\overline{g})_{\Omega} - \left(\overline{w}^s, \overline{h}_N\right)_{\Gamma_N} \tag{1.24}$$

for all test functions $\overline{w}^s$, q^s. Since these equations represent a symmetric saddle point problem, the function space $\mathbf{V}^s, Q^s$, in which we search for the solution, needs to satisfy the Ladyzhenskaya-Babuška-Brezzi (LBB) conditions for stability (Ladyzhenskaya 1969; Donea et al. 2004). A simple example of a function space which satisfies the LBB conditions is Q_{p+1}^{dim}, Q_p (Taylor-Hood elements on quadrilateral/hexahedral grids of order $p+1$ for velocity and p for pressure) with $p \geq 1$, i.e., using elements one order higher for velocities than for pressures. Function spaces that do not satisfy the LBB conditions have also been used in various Stokes flow FEM-based codes (e.g., Hughes

et al. 1986; Silvester and Kechkar 1990; Qin and Zhang 2007; Liao and Silvester 2012; Thieulot 2019). Indeed, they allow the use of lower order elements, which can reduce the computation time and amount of memory used in software. The downfall of these schemes is that they need stabilization processes in order to be able to circumvent the LBB condition. In addition, for Q_1P_0 elements (bi/tri-linear velocity and constant pressure elements) for example, the system to solve is not scalable with the mesh resolution, which makes computation on high resolution meshes not tractable (Thieulot 2019).

- **Linear system**

Assembling the linear system for Stokes equations, if the degrees of freedom are sorted so that the velocity variables come before all pressure variables, the linear system can be subdivided in blocks:

$$\begin{pmatrix} A & B^T \\ B & 0 \end{pmatrix} \begin{pmatrix} U \\ P \end{pmatrix} = \begin{pmatrix} F \\ 0 \end{pmatrix}, \tag{1.25}$$

where U, P are the values of velocity and pressure degrees of freedom, respectively. A is the mass matrix on the velocity space, B is the negative divergence operator and B^T is its transpose and corresponds to the gradient operator. This system, however, has a zero block at the bottom right, and it is indefinite. This implies that solvers such as the Conjugate Gradient (CG) method cannot work, and other iterative solvers such as MinRes, SymmLQ or GMRES cannot be used with their usual preconditioner since there are zeros on the diagonal. This is usually bypassed using a preconditioner such as:

$$P = \begin{pmatrix} A & 0 \\ B & -S \end{pmatrix} \tag{1.26}$$

where S is the Schur complement of the Stokes operator ($S = BA^{-1}B^T$), which is symmetric and positive definite. In this preconditioner, the inverse matrices A^{-1} and $-S^{-1}$ can be approximated through different means (e.g., Kronbichler et al. 2012; Thieulot 2019), and the Stokes system is then solved with an iterative solver.

- **Scaling of discretized equations**

When solving the linear system in Eq. (1.25), using an iterative solver means the solver will iterate until the residual of the linear equations is below a certain tolerance, i.e. until

$$\left\| \begin{pmatrix} F - AU^{(k)} - B^T P^{(k)} \\ B^T U^{(k)} \end{pmatrix} \right\| < Tol \tag{1.27}$$

The first problem with this residual comes from the units of the physical quantities that are present in Eq. (1.27): the first part of the residual has units of

$$\left[\left(\overline{\nabla}\ \overline{w}, p \right)_\Omega \right] = \left[\int_\Omega d\Omega \right] \ \left[\overline{\nabla} \right] \ \left[\overline{w} \right] \ [p] = \mathrm{m}^{\mathrm{dim}}.\mathrm{m}^{-1}.\mathrm{Pa} = \mathrm{kg}.\mathrm{m}^{\mathrm{dim}-2}.\mathrm{s}^{-2} \tag{1.28}$$

while the second part of the residual has units of

$$\left[\left(q, \overline{\nabla} \cdot \overline{v} \right)_\Omega \right] = \left[\int_\Omega d\Omega \right] \ [q] \ \left[\overline{\nabla} \right] \ \left[\overline{v} \right] = \mathrm{m}^{\mathrm{dim}}.\mathrm{m}^{-1}.\mathrm{m}.\mathrm{s}^{-1} = \mathrm{m}^{\mathrm{dim}}.\mathrm{s}^{-1}. \tag{1.29}$$

This means that taking the norm of the residual would lead to units such as $\mathrm{m}^{\dim-1}\sqrt{(\mathrm{Pa})^2}+(\mathrm{m.s}^{-1})^2$, which is nonsensical. In practice, the only way for this not to be a problem is dealing with variables that are around one or that balance each other. In geosciences, and particularly with the models we are interested in, this is not the case: the viscosity η is around 10^{18} Pa.s, velocities are on the order of 10^{-9} $\mathrm{m.s}^{-1}$, and the diameter of domains of study is likely to be around 10^4 m. This makes the first equation to be in the order of $\overline{\nabla}\cdot\left(\eta\overline{\overline{D}}(\overline{v})\right)\approx 10^{18}\frac{10^{-9}}{(10^4)^2}\approx 10^{-1}$, whereas the second equation is in the order of $\overline{\nabla}\cdot\overline{v}\approx\frac{10^{-9}}{10^4}\approx 10^{-13}$. In terms of numerical solver, it means the focus is made entirely on the first part of the residual, and the second Stokes equation is likely to be more or less ignored, which in turn leads to flow without mass conservation. One way of preventing this is returning to the equations and balancing them with a factor $\frac{\eta_m}{L}$, where η_m and L are typical values for the viscosity and length scale of the numerical models. The Stokes equations become

$$\begin{aligned} -\overline{\nabla}\cdot\left(2\eta\overline{\overline{D}}(\overline{v})\right)+\overline{\nabla}p&=\rho\overline{g}\\ \frac{\eta_m}{L}\,\overline{\nabla}\cdot\overline{v}&=0. \end{aligned} \tag{1.30}$$

A problem appears in this case, as the resulting matrix is not symmetric any more. To resolve this, a scaled pressure $\hat{p}=\frac{L}{\eta_m}$ can be introduced in order to have the scaled equations

$$\begin{aligned} -\overline{\nabla}\cdot\left(2\eta\overline{\overline{D}}(\overline{v})\right)+\frac{\eta_m}{L}\overline{\nabla}\hat{p}&=\rho\overline{g}\\ \frac{\eta_m}{L}\,\overline{\nabla}\cdot\overline{v}&=0. \end{aligned} \tag{1.31}$$

which give a symmetric matrix and for which the pressure can be recovered easily from the scaled pressure $\hat{p}$.

Appendix

1.A Using a Stokes flow code to simulate other types of rheologies

Poliakov et al. (1996) underlined that fluid flow equations can approximate other rheologies in geomechanical simulations. Specifically, later works such as Moresi et al. (2003) and Bangerth et al. (2019) showed how the use of an effective viscosity computed from the internal stress at each time step can make these equations model behaviours such as visco-elasticity or visco-plasticity. In practice, it can be done in this way (Moresi et al. 2003):

In the viscous flow assumption, the deviatoric part of the stress is given by Eq. (1.6), with η the viscosity and $\overline{\overline{D}}$ the infinitesimal strain rate tensor defined by Eq. (1.7). In viscoelasticity, however, the deviatoric part of the stress is the sum of an elastic strain rate tensor $\overline{\overline{D}}^e$ and a viscous strain rate tensor $\overline{\overline{D}}^v$:

$$\overline{\overline{D}} = \overline{\overline{D}}^v + \overline{\overline{D}}^e \quad \text{with} \quad \begin{cases} \overline{\overline{D}}^e = \dfrac{1}{2\mu} \overset{\overline{\overline{\nabla}}}{\overline{\tau}} \\ \overline{\overline{D}}^v = \dfrac{1}{2\eta} \overline{\overline{\tau}} \end{cases} \tag{1.32}$$

where μ is the shear modulus, η is the shear viscosity and $\overset{\overline{\overline{\nabla}}}{\overline{\tau}}$ is the Jauman corotational stress rate for an element of the continuum:

$$\overset{\overline{\overline{\nabla}}}{\overline{\tau}} = \dot{\overline{\tau}} + \overline{\overline{\tau}} \cdot \overline{\overline{W}} - \overline{\overline{W}} \cdot \overline{\overline{\tau}} \tag{1.33}$$

where $\overline{\overline{W}}$ is the material spin tensor:

$$\overline{\overline{W}} = -\frac{1}{2} \left(\overline{\nabla}(\overline{u}) - \overline{\nabla}(\overline{u})^T \right) \tag{1.34}$$

$\overline{\overline{W}}$ accounts for material spin during advection, which reorients the elastic stored-stress tensor. We can express the Jauman stress-rate in a finite difference form in order to have a stress/strain relation in combination with Eq. (1.32):

$$\overset{\overline{\overline{\nabla}}}{\overline{\tau}}^{t+\Delta t^e} \simeq \frac{\overline{\overline{\tau}}^{t+\Delta t^e} - \overline{\overline{\tau}}^t}{\Delta t^e} - \overline{\overline{W}}^t \cdot \overline{\overline{\tau}}^t + \overline{\overline{\tau}}^t \cdot \overline{\overline{W}}^t \tag{1.35}$$

where the subscripts t and $t + \Delta t^e$ indicate values at the current and future time step, respectively. Δt^e is a time step which captures the relevant timescales of the changes

in elastic stresses. It also assures that the infinitesimal strain rate tensor can be used. Equation (1.32) becomes

$$\overline{\overline{\tau}}^{t+\Delta t^e} = \frac{2\eta\Delta t^e}{\alpha+\Delta t^e}\overline{\overline{D}}^{t+\Delta t^e} + \frac{\alpha}{\alpha+\Delta t^e}\overline{\overline{\tau}}^{t} + \frac{\alpha\Delta t^e}{\Delta t^e+\alpha}\left(\overline{\overline{W}}^{t}\cdot\overline{\overline{\tau}}^{t} - \overline{\overline{\tau}}^{t}\cdot\overline{\overline{W}}^{t}\right), \tag{1.36}$$

where $\alpha = \eta/\mu$ is the shear relaxation time. We can simplify the previous equations by defining an effective viscosity η_{eff} and an effective strain rate tensor $\overline{\overline{D_{eff}}}$:

$$\eta_{eff} = \eta\frac{\Delta t^e}{\Delta t^e+\alpha} \quad ; \quad \overline{\overline{D_{eff}}} = \left(2\overline{\overline{D}}^{t+\Delta t^e} + \frac{\overline{\overline{\tau}}^{t}}{\mu\Delta t^e} + \frac{\overline{\overline{W}}^{t}\cdot\overline{\overline{\tau}}^{t} - \overline{\overline{\tau}}^{t}\cdot\overline{\overline{W}}^{t}}{\mu}\right) \tag{1.37}$$

Then the deviatoric stress is given by

$$\overline{\overline{\tau}}^{t+\Delta t^e} = \eta_{eff}\overline{\overline{D_{eff}}} \tag{1.38}$$

Equation Eq. (1.38) is composed of a quasi-viscous part with modified material parameters and a force term depending on values from the previous time step. This formulation can minimize the modifications needed to get from a viscous flow code to a visco-elastic code: instead of using the physical parameter for viscosity, one can use an effective value to take into account elasticity, then, during the computation of the force term at time $t+\Delta t^e$, add the term corresponding to elastic internal stresses from the time step t:

$$\overline{F}^{e,t} = -\frac{\eta_{eff}}{\mu\Delta t^e}\left(\overline{\nabla}\cdot\overline{\overline{\tau}}^{t}\right)^T \tag{1.39}$$

Then the momentum conservation part of Eq. (1.11) becomes:

$$\overline{\nabla}\cdot\overline{\overline{\tau}}^{t+\Delta t^e} - \overline{\nabla}p - \underline{f} + \underline{F}^{e,t} = \underline{0} \tag{1.40}$$

which is solved like the usual viscous creep, by substituting $\overline{\overline{\tau}}^{t+\Delta t^e}$ to give a set of equations for velocity unknowns.
This methodology can also be applied to simulate the visco-elasto-plastic behaviour of a material with a viscous flow code and the application of a specific effective viscosity and an effective strain rate tensor (e.g., Moresi et al. 2003).

Chapter 2

FAIStokes

Contents

Abstract In this chapter, I present the FAIStokes code that I developed to perform numerical simulations based on the Stokes equations. I first describe the different parts of the code and its specificities, with details on each step of its workflow. Secondly, I present the benchmarks that were implemented in the code to ensure the quality of its results.

2.1 Introduction

In order to perform numerical simulations on geological models, one can either use an existing software or develop one. I first considered existing software for the simulation of creeping flow (e.g., Underworld (Moresi et al. 2003; Mansour et al. 2020), LaMEM (Popov et al. 2020), pTatin3D (May et al. 2014; Brown et al. 2018), ASPECT (Bangerth et al. 2019), FEniCS (Alnæs et al. 2015), Elefant (Thieulot 2014)), based on how extensible they are, the language in which they have been developed (e.g., Python, Fortran, C, C++), the method used for solving the PDEs (e.g., FEM, FDM), and the license under which they have been released (if they have). After careful consideration, I decided to develop the code FAIStokes in order to have more flexibility and control for the implementation of creeping flow restoration. This code is built on the deal.II library (Bangerth et al. 2007; Arndt et al. 2019, 2020), which it uses for the FE-related algorithms (see Section 1.4.2 for a recap on the FEM). The geological model material tracking is based on the PIC method (see Section 1.4.1.3 for a review of the method) (e.g., Asgari and Moresi 2012; Thielmann et al. 2014; Gassmöller et al. 2018, 2019; Trim et al. 2020), combined with an ALE part on the computation grid. The general workflow of the code is shown in Fig. 2.1 and details on the implementation are given in the first section of the chapter. In order to test the computation parts of the code and check its results, several benchmarks have also been carried out. Their implementation and the parts of the code that they use are discussed in the second section.

2.2 Code and specificities

The FAIStokes code is written in C++ language and compiles using the deal.II library for the FEM part and the RINGpcl library for the research of neighboring particles in a particle cloud using KDtrees. Simulations are available through an executable and a parameter file (Appendix 2.A shows the parameters that can be changed through this file). Several other executables are available for changing the particle swarm (e.g., modification of the faults shear zone thickness, translation and scaling of the model). The main simulation class can also be derived to restore complex models (including layers that must be removed through the simulation for example), such as the one presented in Chapter 4.

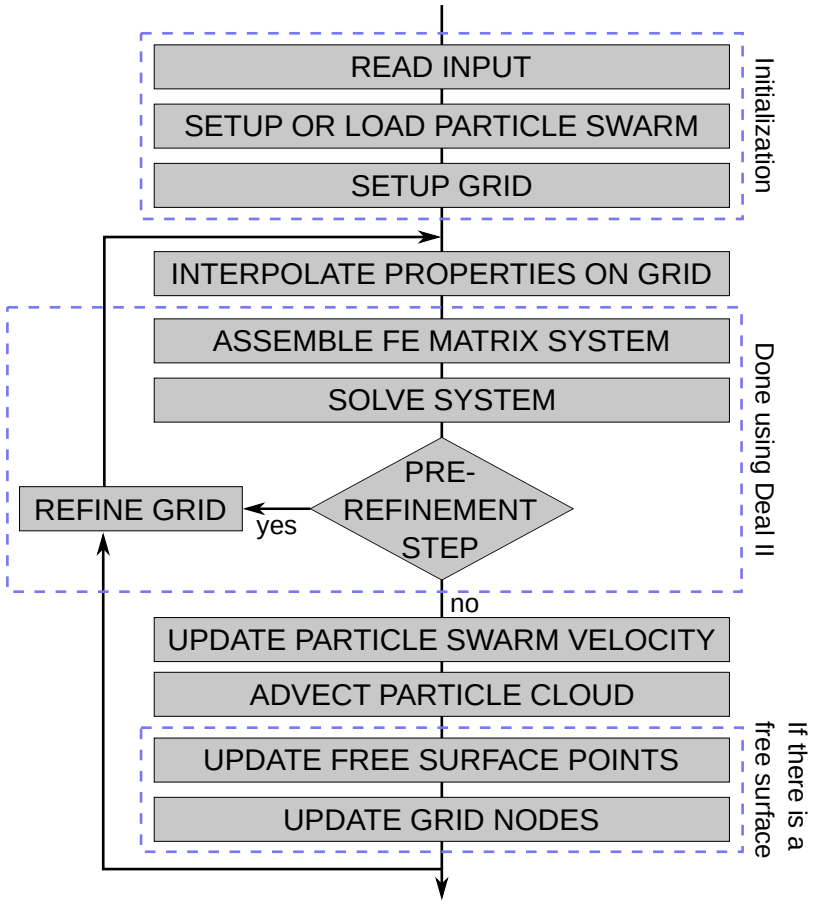

Figure 2.1: Schematic workflow of the FAIStokes code structure. The pre-refinement step occurs at the beginning of the simulation (or during a reinitialization of the grid) to ensure that the velocity used for the advection step is computed using the adaptively refined grid.

2.2.1 Material discretization of a geological model

The geomechanical simulation of a specific domain requires to choose an appropriate kinematic description to follow the displacement inside the geological layers. Continuum mechanics distinguish two main frames: the Eulerian frame of reference, also known as the spatial description, and the Lagrangian frame of reference, also known as the material description (Cornet 2015). Both methods have their advantages and disadvantages, as shown in Section 1.4.1.1, but neither of them is specifically adapted in the case of large displacements over time, such as those studied here. In order to overcome the limitations of the two approaches, the ALE formulation (Fullsack 1995; Donea et al. 2004), which inherits features from both methodologies, was developed (see Section 1.4.1.2). Most of its implementations rely on keeping track of the material properties in a Lagrangian way, while computing the displacement on a grid that can only deform vertically to account for the deformation of a possible free surface. It is particularly useful in geodynamics, in models where the vertical deformation is small compared to the horizontal deformation, and in the case of highly viscous fluids in the mantle, for which the density and viscosity depend mostly on the temperature and depth. In FAIStokes, the computation of the velocity is done by solving the Stokes

equations on a quadrilateral grid. This grid has an ALE part as its nodes can move vertically to follow the movements of the top surface of the model.

During mechanical simulations, the material properties inside the model are tracked using particles; each of these particles discretizes the properties of a small part of the model around it. At the beginning of the simulations, FAIStokes either creates a particle swarm from a distribution of the material parameters or loads it from a file. In the first case, a regularly distributed particle swarm is generated, with a density of particles depending on the size of the smallest element of the computation grid (the two parameters can be tuned in the parameter file, as shown in Appendix 2.A). The given material distribution is then used to associate the material properties to the particles depending on their position. In the second case, one can load a model obtained through previous simulations, or create one. In order to create a model easily, I supervised and worked with two MSc students in a lab internship on the development of a GUI (coded in python and PyQt) for the creation of particle swarms for FAIStokes (Fig. 2.2).

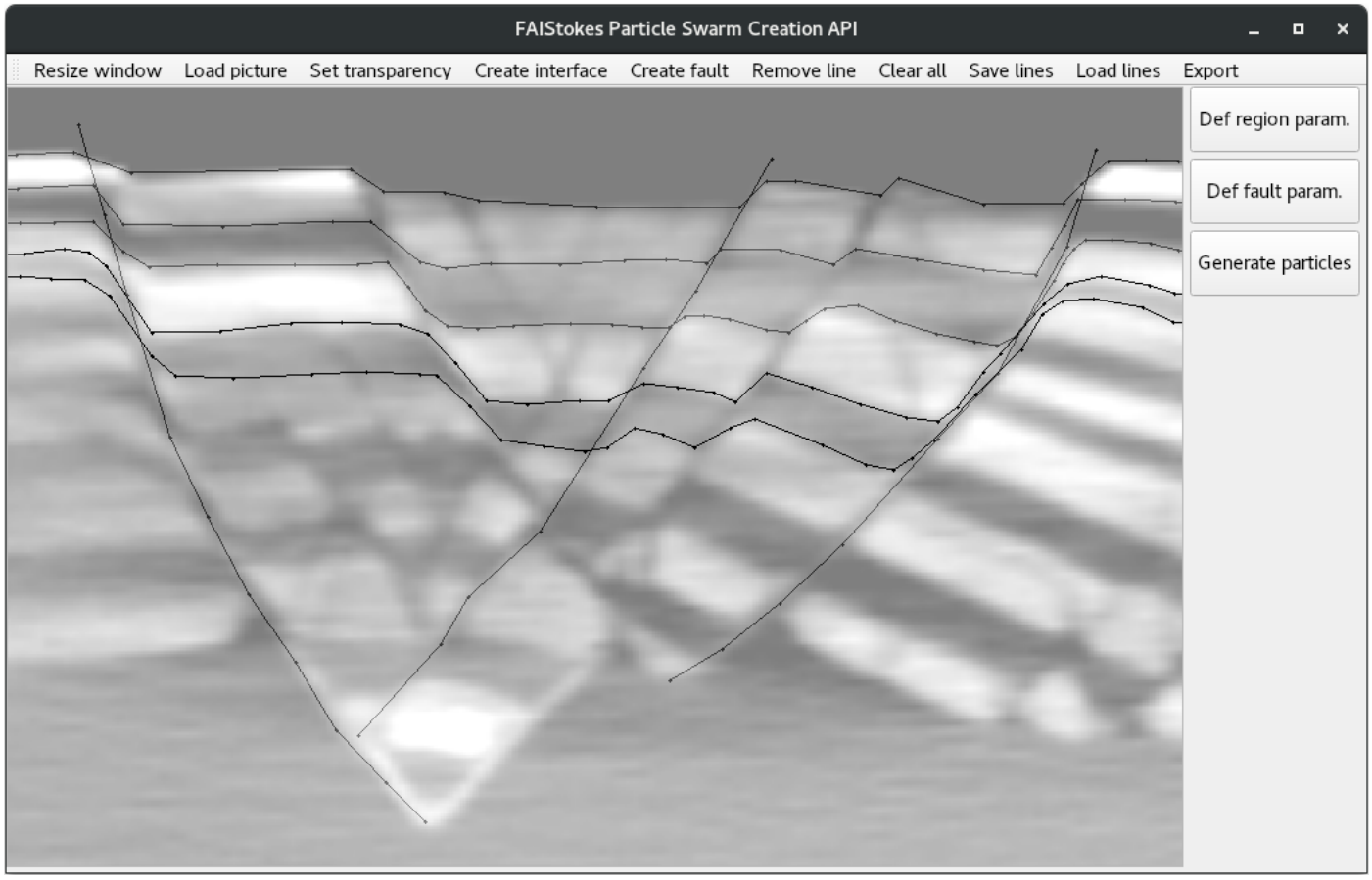

Figure 2.2: Graphical User Interface for the creation of particle swarms to use as input for FAIStokes. In the present example, an image has been loaded, its transparency has been changed, and the user has started digitizing the interfaces and the faults of the cross-section.

Since the particle swarm does not directly track the interfaces, it has to be dense enough to recover accurately the material properties of the model; some parts of the model can be manually densified to keep the appropriate accuracy.

At each time step, the material properties are interpolated from the particle swarm to the grid in order to build the FE matrix and its preconditioner. For each element, the density is interpolated on the quadrature points using an arithmetic mean of the densities of the particles around the quadrature points (closer than a fourth of the diagonal of the smallest elements of the domain). The viscosity is recovered for each element using a harmonic mean of the viscosities of the particles inside the element. This reduces the effect of very high viscosity differences (possibly of several orders of magnitude) on the solver (compared to interpolating it on the quadrature points using the particles nearby), and is more computationally efficient despite the higher grid refinement needed (Deubelbeiss and Kaus 2008; Thielmann et al. 2014; Heister et al. 2017). In the simulations we did with FAIStokes, we have checked that this averaging verifies the conservation of the volume and mass in the model. Subsections 2.3.1, 2.3.2, 2.3.4 and 2.3.5 test the interpolation of the material properties from the particle swarm to the finite element grid and show reasonable accuracy.

2.2.2 FEM discretization

In FAIStokes, the FEM (see Section 1.4.2 for a presentation of the method) algorithms are based on the deal.II library. The domain is discretized on a set of quadrilateral elements, on which FE basis functions are defined. As a review of the application of the FEM to the resolution of Stokes equations is provided in Section 1.4.2, only the specifications of the FAIStokes code are presented here. For solving the Stokes equations, we use quadrilateral Taylor-Hood $Q_2 \times Q_1$ elements that satisfy the LBB conditions for stability (Donea et al. 2004). Contrarily to many creeping flow codes that are used to study the subsurface, the heat transport equation is not solved, both for simplicity and because it is likely to have only a small effect on the strain at the scale at which structural restoration is generally applied (i.e., basin-scale, close to the surface). Moreover, there may be important temperature diffusion at geological timescales, particularly in salt layers, and it is not reversible. As for the boundary conditions, we can use Dirichlet and Neumann conditions that we tune (e.g. rigidity, free-slip, free surface, specific traction or velocity) for each boundary of the different problems at hand. Subsections 2.3.1, 2.3.2, 2.3.4 and 2.3.5 showcase results of the FE benchmarking.

2.2.3 Grid and solvers

The grid and solvers come from the deal.II code, and their use is highly inspired from the deal.II tutorials *step* − *31*[1] and *step* − *32*[2]. The grid is created first as a quadrilateral from the coordinates of the bottom left and top right corners of the domain. This quadrilateral is then split in order to get cells as close to a square as possible, and refined and coarsened adaptively several times to construct the initial grid. One of the advantages of using deal.II is that it ensures the continuity of the solution between the cells at the hanging nodes (nodes that are corners of a refined cell and in the middle of an unrefined cell line) by using specific constraints in the assembly (see lecture 16 from Wolfgang Bangerth's online lectures for more details on the implementation in deal.II).

[1] https://dealii.org/9.0.0/doxygen/deal.II/step_31.html
[2] https://dealii.org/9.0.0/doxygen/deal.II/step_32.html

The FE matrix, its preconditioner and the right-hand side force-vector are constructed using the material properties interpolated from the particle swarm, as described in Subsection 2.2.1. In the right-hand side of Eq. (1.11), the norm of the gravity vector $\overline{g}$ is always 9.81 m.s^{-2} in our simulations. Its direction is downwards by default, but it can be rotated with an angle given in the parameter file, in order to account for tilted models. The matrix system is solved using an iterative FGMReS solver preconditioned by a block matrix involving the Schur complement (Kronbichler et al. 2012). This solution is then used to refine and coarsen the grid adaptively using deal.II's features, based on a gradient estimator in order to minimize the local error. The grid can also be adaptively refined depending on the viscosity changes or the presence of faults in the model. Depending on the input level of refinement, the cycle of building the matrix system, solving it, and adaptively refining and coarsening the grid is repeated several times, as shown in Fig. 2.1. Subsections 2.3.1, 2.3.2, 2.3.4 and 2.3.5 show the results of benchmarks that challenge the computation of the velocity on different setups.

2.2.4 Velocity interpolation

Once the grid refinement has been completed, the particle swarm is advected by the obtained solution. In FAIStokes, the interpolation of the velocity is done separately in each grid cell with a Q_2 interpolation scheme (although Q_1 interpolation is also available). Depending on whether the simulation is forward or backward, the displacement of each particle for a time step Δt is computed using Eq. (1.12) or (1.13). The value of Δt is computed from the CFL condition. The default value for the CFL number is 0.085. This default value is sufficient in the case of simulations with small deformations, but may need to be reduced in the case of very large deformations and very high viscosity contrasts (for example, the results shown in Chapter 3 use a CFL number of 0.0085, while the benchmarks in Section 2.3 use a CFL number of 0.042). The advection is done with a 2^{nd}-order Runge-Kutta scheme in space: at each time step, the particles are first advected by half the computed displacement; the velocity is then interpolated on their new position to update the displacement, and particles are advected then again by half of this new displacement. This scheme reduces the error in the advection process without need for simulation time step refinements. It is computationally efficient because the interpolation of the displacement on the particle swarm is inexpensive as compared to solving the FE matrix system. The CVI scheme presented in Jenny et al. (2001); Meyer and Jenny (2004); Wang et al. (2015) is implemented in FAIStokes for the Q_1 interpolation. It relies on adding specific terms to the interpolation of the velocity on the particles to ensure that it is conservative (i.e., that the divergence of the velocity is zero). Its implementation for the Q_2 interpolation has been studied but is not necessary as Q_2 interpolation is already conservative. Subsections 2.3.3, 2.3.4 and 2.3.5 show the results of benchmarks that test the interpolation of the velocity in time-dependant problems.

2.2.5 Free surface implementation

In order to model the interface between the air and the model, two main approaches are available: the implementation of a free surface, or the "sticky air" method (e.g.,

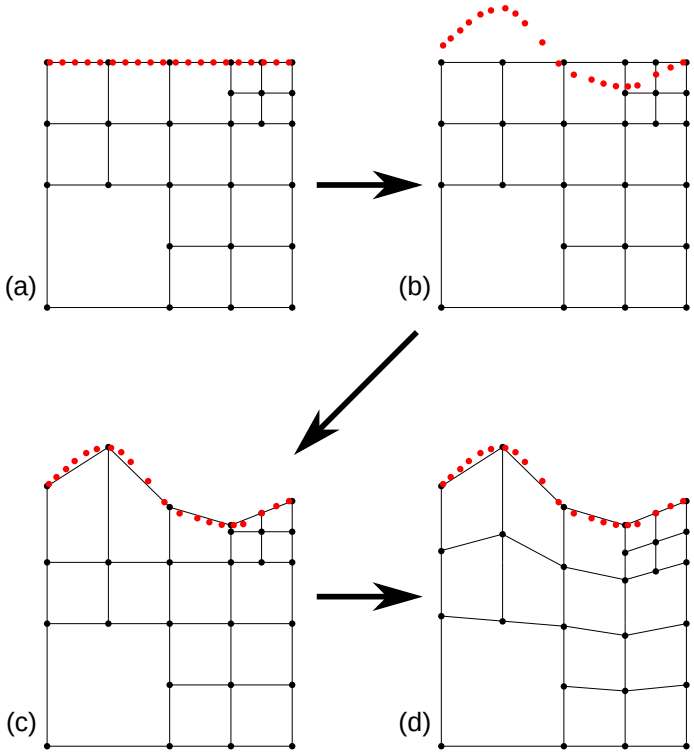

Figure 2.3: Process for the update of the free surface (the motion is exaggerated for the sake of the explanation, and is less extreme in reality): (a) Initial state where the velocity is computed on the grid. (b) The point swarm tracking the free surface is advected according to the computed velocity. (c) The grid nodes at the top of the free surface are moved vertically to match the point swarm. (d) The deformation of the grid is diffused to the rest of the nodes.

Crameri et al. 2012, for a benchmark and a comparison of the two methods). The sticky air method considers a layer of material with a low viscosity and zero density, the difficulty being that this viscosity needs to be sufficiently low to be negligible compared to the rest of the model, but high enough for the solvers to converge. The free surface method considers that no force is applied on the surface of the computational mesh ($\overline{h}_N = 0$ in Eq. (1.22)). While this is theoretically simple, it is numerically complicated to implement, because the computational mesh needs to honor the movement of the free surface.

In FAIStokes, in the case of a free surface on the top of the model, the top surface is tracked by a separate point swarm. This point swarm is denser than the material particle swarm and is one dimension lower (i.e. a line in our 2D cases). It is advected at each time step the same way as the particle swarm that represents the geological model. After its displacement or during the setup of the grid, the free surface point swarm is used as a reference to move vertically the nodes of the grid at the top of the model, so that they match the free surface. This vertical displacement is then propagated to the rest of the grid so that the grid cells stay as close to squares as possible, while not affecting the other boundaries. Figure 2.3 illustrates the whole process. Since our models are isothermal, no special processing is required to correct the temperature field during this process. Subsection 2.3.4 shows the results of a benchmark that tests the

free surface implementation along with other computational parts of the code. The free surface stabilization algorithm (FSSA) developed by Kaus et al. (2010) and showcased in Quinquis et al. (2011) has been implemented in FAIStokes as well; we benchmark it in Subsection 2.3.5. It relies on adding a specific term during the assembly part of the FE matrix to account for the density difference between the two sides of the faces of the elements (in all the elements of the grid).

For test and comparison purposes, the sticky air method has also been implemented and coupled with the FSSA. It uses the moving grid feature of the free surface so that the cells containing air and rock layers are distinct, and performs similarly to the free surface on the benchmarks presented in Subsections 2.3.4 and 2.3.5. In the rest of the manuscript, however, we choose to use the free surface implementation for simulations where an interface with air is considered, as the results are as good and the computation time smaller.

2.3 Benchmarking a creeping flow code

Benchmarks are used in order to check the code and to make sure that the error in the simulation results is lower than the expected threshold. The idea is to test the different parts of the code on simple models where either the analytical solution is known, or on models where several other software have given acceptable results. In FAIStokes, five benchmarks were implemented, each of them testing one or several features presented in the previous section. This section is also available in the appendices of Schuh-Senlis et al. (2020).

2.3.1 Taking into account small scales inside a model : the Rayleigh-Taylor instability benchmark

This benchmark is based on the analytical solution of a Rayleigh-Taylor instability by Ramberg (1968) and was carried out in various numerical studies (Deubelbeiss and Kaus (2008); Thieulot (2011)). It consists of a two-layer system driven by gravity, the density of the bottom layer being smaller. The bottom and top boundaries have a no-slip boundary condition, while the sides have a free-slip boundary condition.

The first layer, made of fluid 1 with properties (ρ_1, η_1), overlays the second layer, made of fluid 2 (ρ_2, η_2). An initial sinusoidal disturbance of the interface between the two layers is introduced, characterized by an amplitude Δ and a wavelength λ, as shown in Fig. 2.4.

Under these conditions, the analytical velocity of the diapiric growth v is given by Ramberg (1968):

$$\frac{v}{\Delta} = -K \frac{\rho_1 - \rho_2}{2\eta_2} h_2 g \tag{2.1}$$

with K the dimensionless growth factor given by

$$K = \frac{-d_{12}}{c_{11} j_{22} - d_{12} i_{21}} \tag{2.2}$$

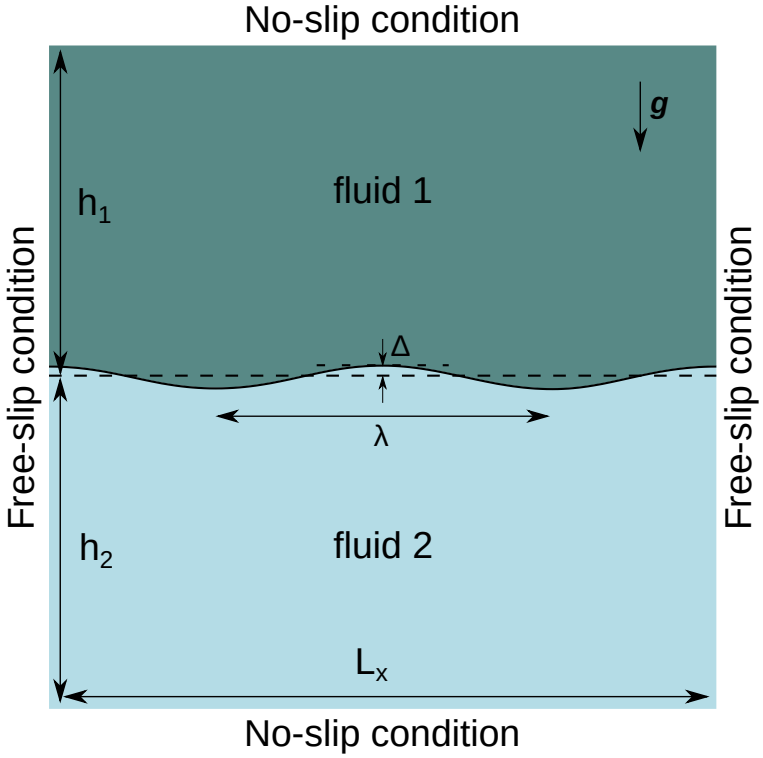

Figure 2.4: Rayleigh-Taylor instability benchmark initial setup.

which involves the following factors:

$$
\begin{aligned}
\phi_1 &= \frac{2\pi h_1}{\lambda} \\
\phi_2 &= \frac{2\pi h_2}{\lambda} \\
c_{11} &= \frac{2\eta_1\phi_1^2}{\eta_2(\cosh(2\phi_1)-1-2\phi_1^2)} - \frac{2\phi_2^2}{\cosh(2\phi_2)-1-2\phi_2^2} \\
d_{12} &= \frac{\eta_1(\sinh(2\phi_1)-2\phi_1)}{\eta_2(\cosh(2\phi_1)-1-2\phi_1^2)} + \frac{\sinh(2\phi_2)-2\phi_2}{\cosh(2\phi_2)-1-2\phi_2^2} \\
i_{21} &= \frac{\eta_1\phi_2(\sinh(2\phi_1)+2\phi_1)}{\eta_2(\cosh(2\phi_1)-1-2\phi_1^2)} + \frac{\phi_2(\sinh(2\phi_2)+2\phi_2)}{\cosh(2\phi_2)-1-2\phi_2^2} \\
j_{22} &= \frac{2\eta_1\phi_1^2\phi_2}{\eta_2(\cosh(2\phi_1)-1-2\phi_1^2)} - \frac{2\phi_2^3}{\cosh(2\phi_2)-1-2\phi_2^2}
\end{aligned}
\tag{2.3}
$$

We set $\rho_1 = 3300$ kg.m^{-3}, $\rho_2 = 3000$ kg.m^{-3}, $\eta_1 = 10^{21}$ Pa.s, $L_x = h_1/2 = h_1 + h_2 = 512$ km, and $\Delta = 3$ km. We make η_2 vary between 1.25×10^{20} and 2.5×10^{23} Pa.s, while λ takes three values: $L_x/2, L_x/4, L_x/8$ (Fig. 2.5).

A first run is done, where the FEM grid is fixed to 80×80 elements, each containing 10^2 regularly spaced particles. In order to test the influence of adaptive refinement, we conduct a second run with a grid starting at 80×80 elements and three levels of adaptive refinement. We also refine the particle swarm adaptively: each initial cell (before the adaptive refinement) is first filled with 5^2 regularly spaced particles, and then the swarm is densified to 64 times more particles around the interface between the two fluids. For each deformation wavelength, the velocity is computed in the model at

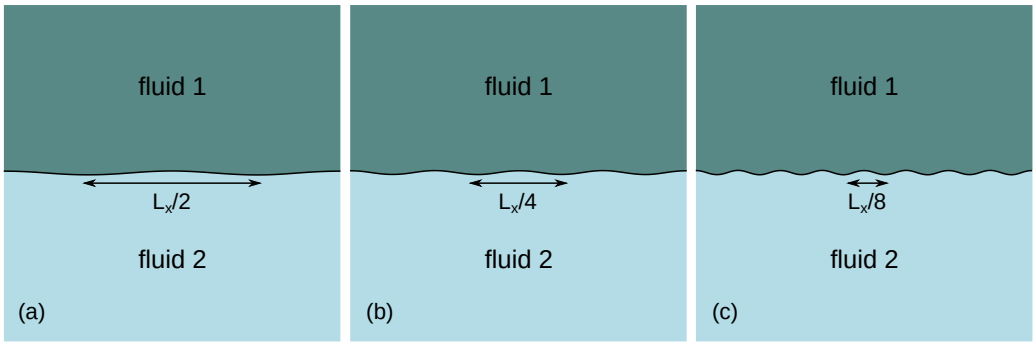

Figure 2.5: Initial setup of the Rayleigh-Taylor instability benchmark with 3 different wavelengths: a) $\lambda = L_x/2$, b) $\lambda = L_x/4$, c) $\lambda = L_x/8$

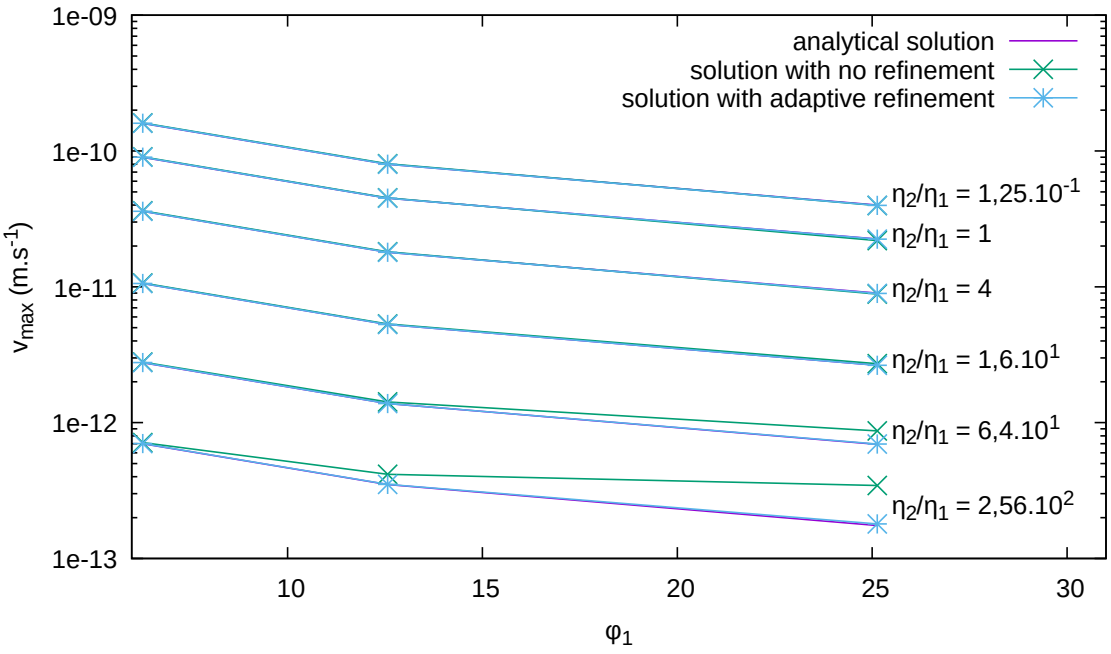

Figure 2.6: Comparison between numerical and analytical results for the Rayleigh-Taylor instability benchmark. The numerical results are computed for a 80×80 element grid and for the same grid with three levels of adaptive refinement.

the first time step, for different viscosity ratios η_2/η_1, to compare it to the analytical velocity. The results are shown along with the analytical ones in Fig. 2.6.

Overall, results show a good agreement between the computed solution and the reference, especially in the case of adaptive refinement, where the relative error falls beneath 2.5% for all the curves. Since ϕ_1 is inversely proportional to the wavelength λ, it means that the code can account well for small disturbances, especially with the use of adaptive refinement on the parts with higher velocity and high contrasts in viscosity.

This benchmark ensures the validity of the code in the presence of large viscosity contrasts, even if those contrasts are located on objects that are small compared to the size of the model. It also validates the averaging of the density and viscosity from the particles to the finite element grid.

2.3.2 Taking into account viscosity changes : the falling block benchmark

This benchmark appears in Gerya (2019) and in Thieulot (2011). It consists in modeling the fall of a block of fluid of properties (ρ_1, η_1) inside another fluid of properties (ρ_2, η_2), with $\rho_1 > \rho_2$. The domain is a square of size $L_x = L_y = 500$ km, and the block (a square in 2D) of size 100×100 km is initially centered at point ($x = 250$ km, $y = 400$ km), as shown in Fig. 2.7.

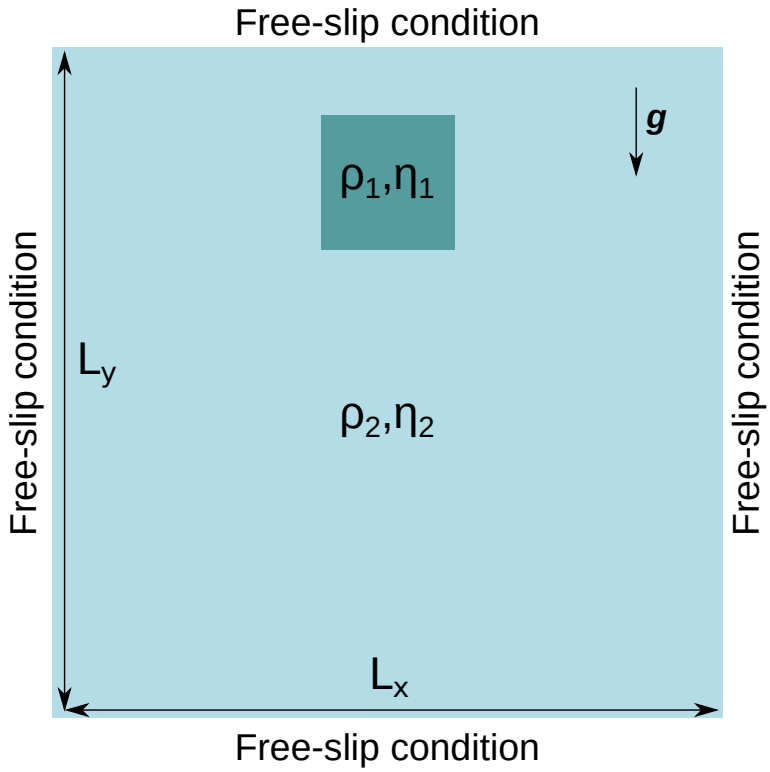

Figure 2.7: Falling block benchmark initial setup.

The simulation is carried out on a 50×50 element grid that is adaptively refined three times. Like in the previous benchmark, the particle swarm is created by first introducing 5^2 particles in each initial element, and then densifying it up to 64 times more particles around the zone of interest (i.e. the falling block). Free-slip boundary conditions are imposed on all sides of the domain. We carry out five experiments:

- Exp.1: $\eta_2 = 10^{20}$ Pa.s, $\rho_1 = 3220$ kg.m^{-3};
- Exp.2: $\eta_2 = 10^{21}$ Pa.s, $\rho_1 = 3300$ kg.m^{-3};
- Exp.3: $\eta_2 = 10^{22}$ Pa.s, $\rho_1 = 6600$ kg.m^{-3};
- Exp.4: $\eta_2 = 10^{23}$ Pa.s, $\rho_1 = 3300$ kg.m^{-3};
- Exp.5: $\eta_2 = 10^{24}$ Pa.s, $\rho_1 = 9900$ kg.m^{-3};

In all the experiments, the density of the surrounding fluid is $\rho_2 = 3200$ kg.m^{-3} and the viscosity of the block is varied between 10^{19} and 5×10^{27} Pa.s. The velocity of the

falling block is measured in its center at $t = 0$ for all experiments. Following physical intuition, one expects the velocity of the block to: (a) decrease when the viscosity of the surrounding fluid η_2 increases (i.e. when going from Exp.1 to Exp.5), and (b) increase with the density contrast $(\rho_1 - \rho_2)$ in each experiment. To check this behavior, we measure $v\eta_2/(\rho_1 - \rho_2)$ as a function of the viscosity contrast $\log_{10}(\eta_2/\eta_1)$. The results of the benchmark are plotted in Fig. 2.8.

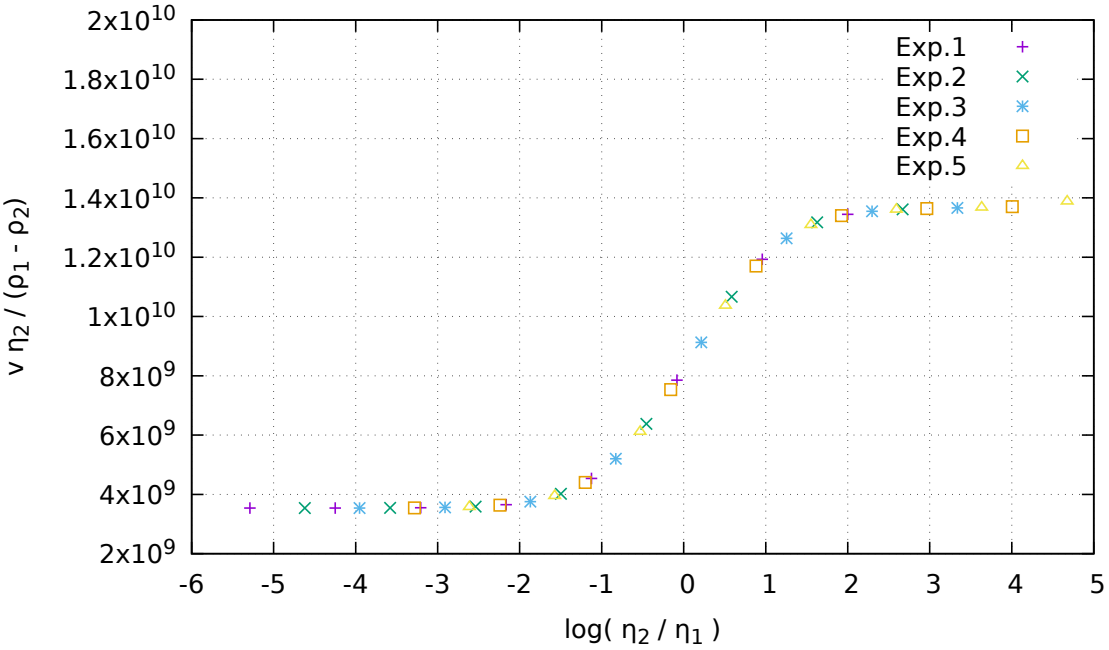

Figure 2.8: Velocity measurements as a function of the viscosity contrast between surrounding medium and block for the experiments of the falling block benchmark.

We can see that the experimental points line up on a single curve. This concurs with the results obtained by Gerya (2019) and Thieulot (2011). This shows that FAIStokes can deal with gravity-driven simulations where $0.6\% \leq (\rho_1 - \rho_2)/\rho_2 \leq 210\%$ and the viscosity contrasts are as strong as $10^{-6} \leq \eta_2/\eta_1 \leq 10^5$ in a consistent manner.

2.3.3 Advecting particles : the rotation benchmark

This benchmark aims at assessing the error in the advection part only (Section 2.2.4). The setup of the model is a square of size 10×10 km, where we study the advection of a single particle, starting at coordinates $(8\text{ km}, 5\text{ km})$ and doing a 2π rotation around the center point $(5\text{ km}, 5\text{ km})$ (Fig. 2.9). A velocity field is prescribed in the domain and discretized on the grid: on each grid point, the velocity has a constant norm and is always normal to the line connecting the point to the model center:

$$\overline{v} = v_0.\overline{e_\theta} = \begin{pmatrix} v_0.sin\theta \\ v_0.cos\theta \end{pmatrix} \tag{2.4}$$

The grid is not adaptively refined here, and is composed of 16×16 elements. In order to have scales that are geologically relevant, we choose $v_0 = 3$ cm.year^{-1} and vary the

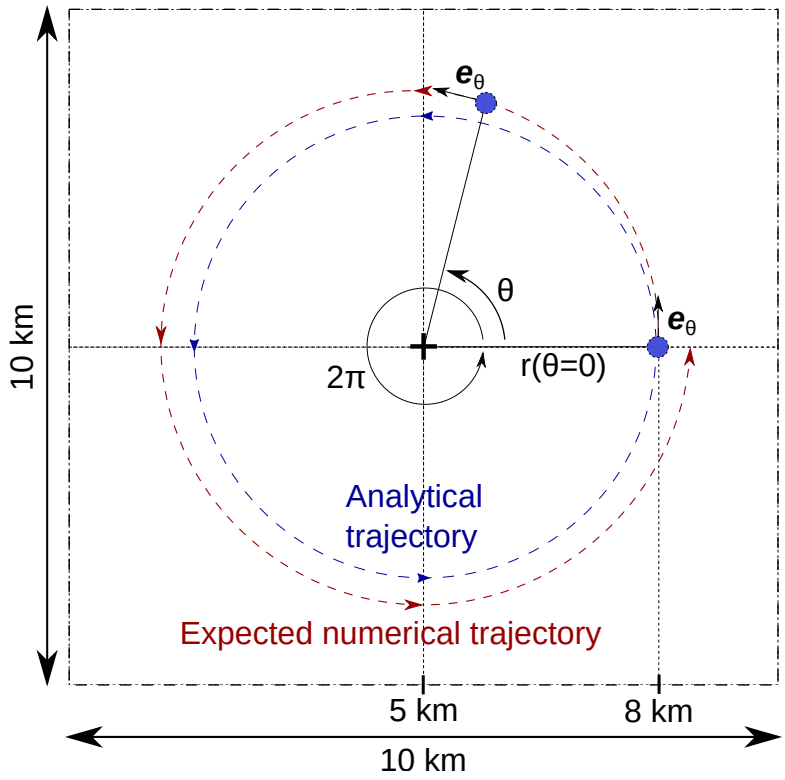

Figure 2.9: Setup for the rotation benchmark, assessing errors on the advection of particles.

time step Δt between 500 and 2000 years (in this setup, the CFL numbers chosen for our simulations would give a time step between 175 years for the lowest CFL number and 1753 years for the highest CFL number). The second order Runge-Kutta scheme presented in Section 2.2.4 is used at all time steps. We then evaluate the distance $\Delta r = |r(\theta = 0) - r(\theta = 2\pi)|$. This distance gives us a measure of the error made in the computation of the particle advection, and allows us to compare different advection schemes. Figure 2.10 shows the results obtained for a 2π rotation of the particle with different interpolation schemes. We can see that reducing the time step linearly reduces the error on the radius $r(\theta)$. In this setup, the type of interpolation mostly impacts the stability of the interpolation, and not the accuracy. In the simulations presented in the rest of the manuscript, the Q2 interpolation scheme was chosen, for its precision and stability.

2.3.4 Taking into account the top surface in contact with air : the free surface benchmark

This benchmark is presented in Crameri et al. (2012), where it is applied on several numerical codes to compare their implementation of the free surface, and evaluate the use of the 'sticky air' method. It will be used here to evaluate the quality of our approximation and interpolation of the free surface. It consists on a cosine-shaped layer of homogeneous lithosphere overlaying a homogeneous layer of mantle. For this type of model, Ramberg (1981) gives an analytical solution for the maximal height of the

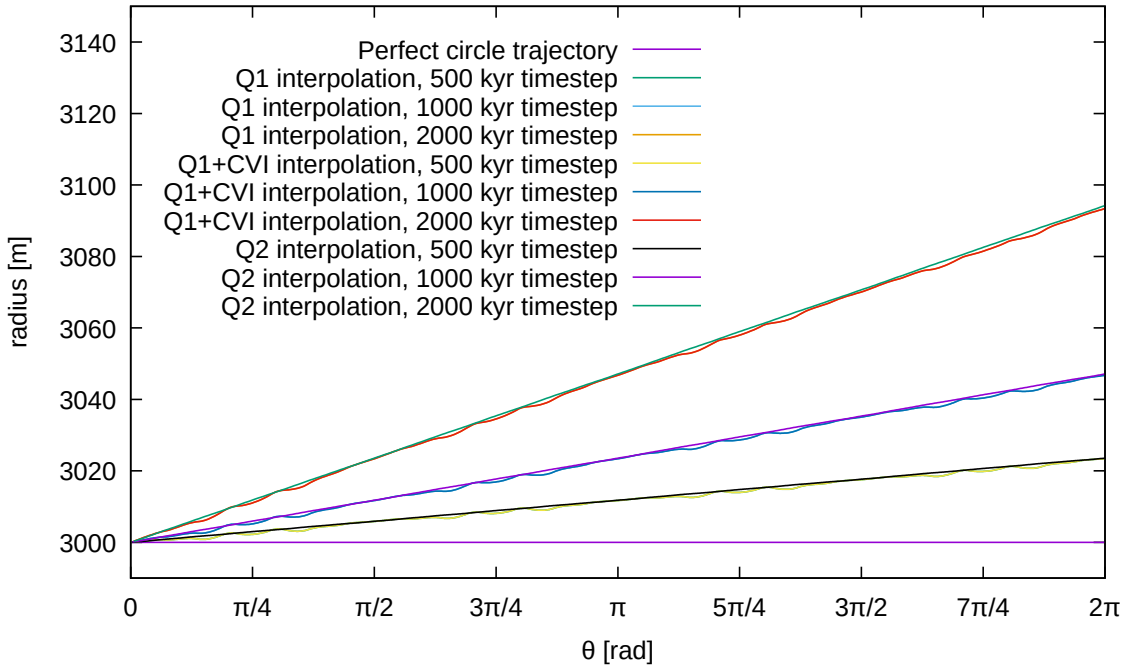

Figure 2.10: Results for the rotation benchmark obtained with different time steps and advection schemes.

topography at each time t :

$$h_{analytical}(t) = h_{initial}\ \exp(-\gamma t) \tag{2.5}$$

where γ is the relaxation rate and $h_{initial}$ is the value of h at the beginning of the simulation. The model setup for the benchmark is shown in Fig. 2.11.

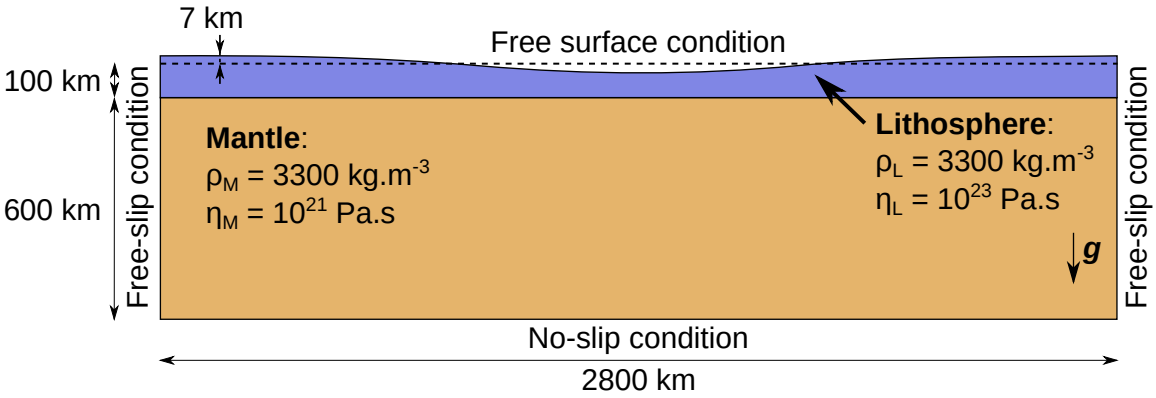

Figure 2.11: Model setup for the 2D free surface benchmark.

The bounding box of the model spans 2800 km by 707 km. The underlaying mantle layer is 600 km thick, while the lithosphere has a thickness between 93 and 107 km. The lithosphere's top surface is cosine-shaped with an amplitude of 7 km and a wavelength of the size of the domain. The mantle and lithosphere have a density of $\rho_M = \rho_L = 3300$ kg.m^{-3} and a viscosity of $\eta_M = 10^{21}$ Pa.s and $\eta_L = 10^{23}$ Pa.s, respectively. We set free-slip boundary conditions for the sides and a no-slip condition on the bottom of the

model. The initial grid is made of 16×64 elements and is adaptively refined 3 times. The particle swarm contains 484 160 particles; it is constructed by first sampling regularly the domain, and then adaptively densifying the swarm to 64 times more particles in the lithosphere and upper part of the mantle. In this setup, Crameri et al. (2012) give a characteristic relaxation rate $\gamma = 0.2139 \times 10^{-11}$ s^{-1} and a characteristic relaxation time $t_{relax} = 14.825 \times 10^3$ years. The results obtained with FAIStokes are given in Fig. 2.12.

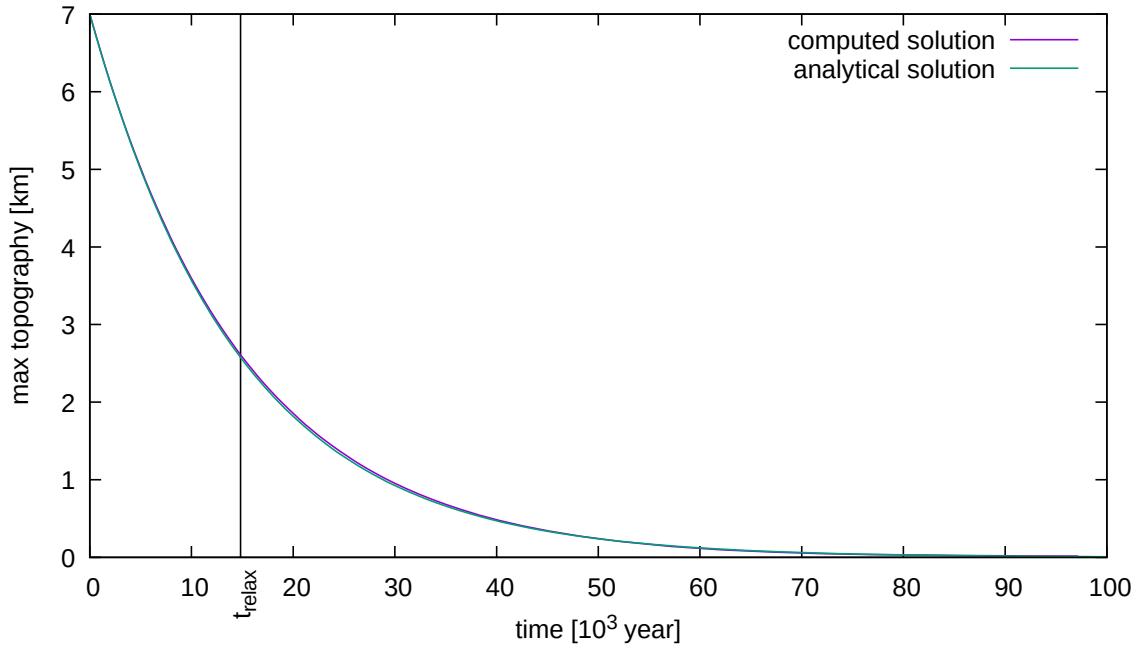

Figure 2.12: Comparison between the analytical and numerical results of the maximum topography over time for the free surface benchmark.

The numerical results are close to the analytical ones, with only a 1.3% error at the characteristic relaxation time. This shows the capacity of FAIStokes to compute the solution of Stokes equations with a free surface for small vertical deformation, and to advect the particles inside the model. It also gives another evaluation of the handling of gravity-driven flow, this time with the addition of evolution inside the model.

2.3.5 Upgrading the free surface movement : the sloshing benchmark

This benchmark is presented in Kaus et al. (2010), where it is used to assess the results of the FSSA presented in the same article. It is used here to verify the implementation of the same algorithm in our code, as well as check the behavior of the free surface in another setup. The benchmark model is another Rayleigh-Taylor instability with a dense, more viscous layer sinking into a less dense fluid (Fig. 2.13).

The model span is 500 km $\times$ 500 km; the side boundaries have a free-slip condition, the lower boundary has a no-slip condition, and the top boundary is a free surface. The initial perturbation between the two layers is sinusoidal with an amplitude of 5 km. The computation is carried out on a grid with 25×25 initial elements and three adaptive refinement steps. The particle swarm counts 25 000 particles; it is constructed by first

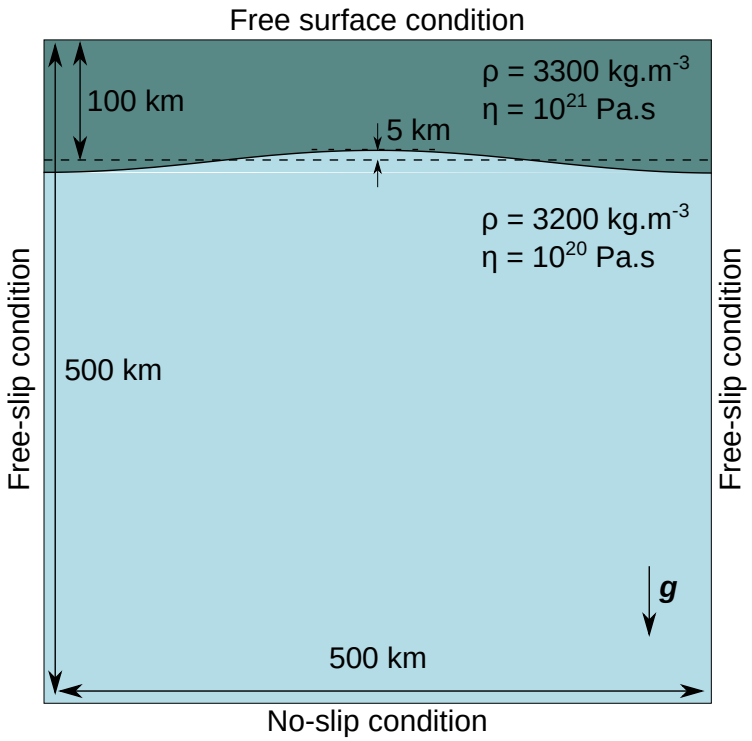

Figure 2.13: Sloshing free surface benchmark initial setup.

sampling regularly the model and then densifying it to 64 times more particles around the interface. The specificity of this benchmark is the apparition of a sloshing instability (also referred to as the "drunken sailor" instability) if the simulation time step is too large. Specifically here, without the FSSA, the forward simulation is stable with a time step Δt of 2500 years, but with $\Delta t = 5000$ years, an instability emerges as the velocity pattern changes direction from one time step to the other (cf. Fig. 2.14).

In order to follow the evolution of the free surface, we keep track of the altitude of the most top-left point over time. Results of a 0.5 Myr simulation, for different time steps Δt, with and without the FSSA, are shown in Fig. 2.15. We can see that the implementation of the FSSA removes the sloshing behavior of the free surface that appeared with a time step Δt of 5000 years, and keeps the free surface stable even with larger time steps. Moreover, the results show great similarities to those of Kaus et al. (2010) and Thieulot (2019). This validates the implementation of the free surface stabilization algorithm. It also gives another evaluation of the handling of gravity-driven flow with a free surface, this time with the additional resolution of an instability that can occur with free surfaces.

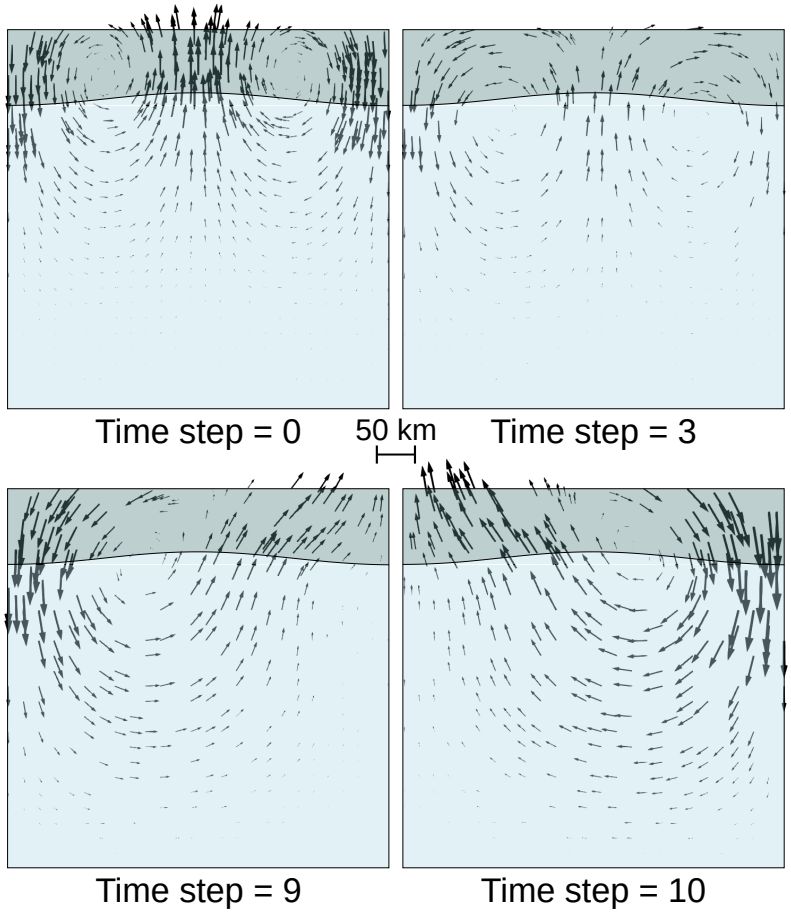

Figure 2.14: Simulation evolution for $\Delta t = 5000$ years, showing the sloshing instability: the velocity pattern changes from one time step to the other, the velocity norm increasing each time.

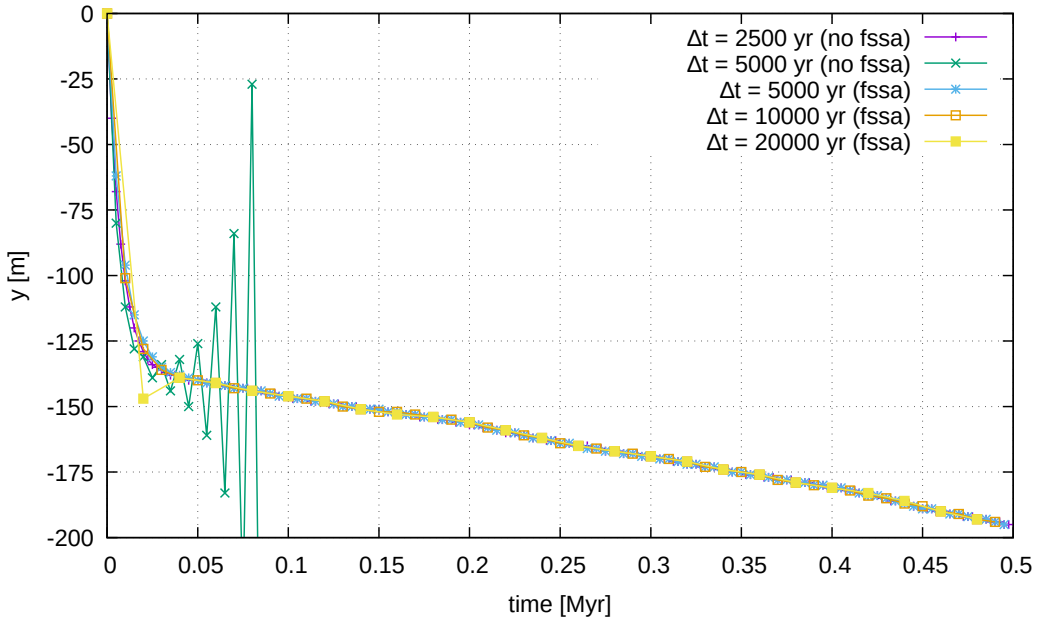

Figure 2.15: Altitude of the most top-left point of the grid over time, for the sloshing free surface benchmark, for different time steps with and without the FSSA.

Appendix

2.A FAIStokes parameter file

The main FAIStokes executable launches a creeping flow simulation, for which a parameter file is used to set some simulation parameters, or change them from the default value, without recompiling the C++ code (Table 2.A.1).

Table 2.A.1: Parameters that can be set in the FAIStokes parameter file, and their default value if they are not changed.

Parameter	Default value	Description
Model bottom left point	(0,0)	Model bounding box
Model top right point	(50 km,10 km)	
Time flow	Forward	Forward or backward (restoration)
Model to load	no model (default properties distribution)	Path to the file to load (supports vtu and vtk point files)
Top surface to load	flat top surface	
Passive tracker swarms	no passive trackers	Path to particle swarms to advect passively in the simulations
Model tilt angle	0	angle to rotate the gravity vector $\overline{g}$ to account for tilted models
Number of particles	3	The number of particles per direction to have in the most refined elements
Paint pattern on points	disabled	Paints an additional parameter on the points to have a graphical idea of the deformation of the model
Grid initial subdivisions	(1,1,1)	Initial subdivision of the grid, to have cells as close to a square as possible
Grid global refinement	2	Global refinement of the grid after the initial subdivision
Grid adaptive refinement	2	Number of adaptive refinement steps after the global grid refinement
Adaptive refinement interval	5	Number of time steps between each call to the refinement and coarsening function on the grid
Grid reset interval	0	Number of steps between each rebuild of the grid from scratch (0 as value disables it). Can be useful to rebuild the grid if it is too deformed

Free surface update propagation	enabled if there is a free surface	Propagates the deformation of the top grid nodes to the rest of the grid.
Start time	0	Starting time of the simulation (in years; can be used to restart a simulation after a break for example)
End time	100 million years	Time after which the simulation stops (in years)
Min time step	0	Minimum time step duration (in years)
Max time step	100 million years	Maximum time step duration (in years)
CFL divider	1	Number to divide the CFL number with
Max Velocity	-1	Maximum velocity accepted (disabled if negative). Can be useful to stop the simulation if it becomes unstable (because of the free surface for example)
Top surface type	Free slip	Can either be No slip, Free slip, Free surface, Free surface with the FSSA, Sticky air or Flattening condition
Right boundary type	Free slip	Can either be No slip, Free slip, Fixed flow or Neumann traction condition
Left boundary type	Free slip	
Bottom boundary type	No slip	Can be Free slip or No slip
IO type	.vtu files	In/Out type of files. .vtu and .vtk files are supported
Graphical output interval	5	Number of time steps between in output of the model geometry
Pressure scaling	10^{17}	Pressure scaling to apply. See Section 1.4.2.2 for more details
RK scheme order	1	Runge-Kutta scheme order
Viscosity interpolation type	Harmonic	Interpolation used for the viscosity. Minimum, Harmonic, Geometric, Arithmetic and Maximum Interpolation are available.
Density interpolation type	Arithmetic	Interpolation used for the viscosity. Minimum, Harmonic, Geometric, Arithmetic and Maximum Interpolation are available.
Solver type	FGMRes	GMRes and direct solvers are also available
Use full block preconditioner	disabled	Default uses a simplified version of the assembly block for the preconditioner, but the full block can also be used. It is more expensive but can be better in the case of large viscosity contrasts.
FEM space degree for the velocity	2	Degree of the polynomials used for the velocity elements. Pressure elements are always one degree lower.
Use locally conservative discretization	enabled	Uses a discretization that is locally conservative for the mass, at the expense of a higher number of degrees of freedom. It is based on using DGPk elements for the pressure.

Chapter 3

First results and first issues

Contents

Abstract In this chapter, I show the results obtained with the creeping flow restoration method introduced in Section 1.3.2 and applied with the FAIStokes code presented in chapter 2. I first introduce the results obtained on some models with simple boundary conditions and forward-backward simulations. While these models bring nothing new to the creeping flow restoration method, they show that the code and method allow the restoration of synthetic models with simple boundary conditions. Secondly, I present the problems linked to the use of a free surface at the top of the models in the restoration scheme, and show a model that bypasses these problems with the help of lateral flow boundary conditions. Those results go beyond what has been done up till now, as they show that the method can be applied to models including faults and where the topography is considered as being a free surface. Finally, I show a first assessment of the choice of material parameters inside a model where the forward deformation is not known. Even if the boundary conditions and material discretization are simplified, it gives an idea of how to determine them in geological models. Those results were used to prove the concept of applying the creeping flow restoration method to models of sedimentary basins including salt, faults and a non-flat topography, and were published in Solid Earth (Schuh-Senlis et al. 2020).

3.1 Introduction

The aim of structural restoration is to make a structural model go backwards in time, with the help of different methods. One of the underlying difficulties, however, is that while the method can help verifying the validity of a structural model, the validity of the restoration methods themselves is hard to ascertain. Indeed, the deformation in geological models is linked both to large and small scales heterogeneity, as well as complex boundary conditions. As such, the results of a restoration scheme on a real-case geological model usually cannot be compared to the past states of the model, as they are not known. This makes the validation of restoration simulations results quite complicated. To check the restoration process nonetheless, we first use it on synthetic models. A forward simulation run is done, and the resulting model is used as a starting point for a restoration simulation. This allows an assessment of the restoration validity by comparing the models at the beginning of the forward simulation and at the end of the restoration. This process was used on models with simple setups and simple boundary conditions, where it proved to work well. We then show the issues that can appear with more complex boundary conditions, and how we dealt with them. Finally, we introduce a first assessment of the impact of material properties on the restoration simulation by using a model setup produced from a seismic image, where these properties are not known.

3.2 Results on simple models

This first section aims at testing the restoration method on simple models (i.e., simple geometry and simple boundary conditions).

3.2.1 The upscaled Van Keken model

The first test model is scaled up from van Keken et al. (1997). The setup consists of a simple two-layered system driven by gravity, as shown in Fig. 3.1.

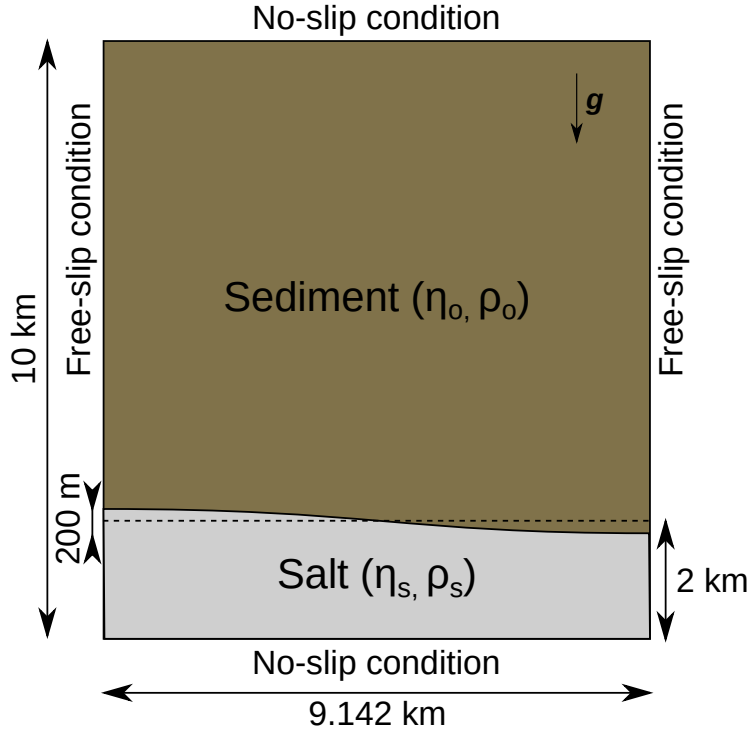

Figure 3.1: Setup of the model scaled up from van Keken et al. (1997).

The upper layer represents sediments that are denser than the lower layer which contains salt ($\rho_o = 2600$ kg.m^{-3} for the sediment layer and $\rho_s = 2150$ kg.m^{-3} for the salt layer). A sinusoidal instability initiates the movement at the beginning of the simulation. The model is limited to a 10 km $\times$ 9.142 km domain (the width value is given by van Keken et al. (1997) to yield the largest growth rate for the diapir) with free-slip boundary conditions on the sides and no-slip boundary conditions on the top and bottom sides. The grid has 32^2 initial elements and two levels of additional adaptive refinement. The particle swarm has a heterogeneous particle density: it is first sampled regularly in the model and then densified to five times more particles around the interface between the two layers to facilitate the tracking of material properties. The average distance between two particles near the interface is 14.3 m. The total number of particles is 64 000. Two experiments were performed in this model: the first one as a test with isoviscous materials ($\eta_o = \eta_s = 10^{19}$ Pa.s), and the second one with material properties closer to reality with a lower viscosity for salt ($\eta_o = 2.8 \times 10^{19}$ Pa.s for the sediment layer and $\eta_s = 1.4 \times 10^{17}$ Pa.s for the salt layer).

For each experiment, we first did a forward simulation, and then we applied the

restoration scheme to the results obtained at the end of the simulation. The state obtained after 6×10^6 years for the first test and 1.5×10^6 years for the second test, as well as the restored models, are shown in Fig. 3.2. The duration of the restoration simulation is the same as the forward simulation, for each experiment. A video of the restoration of the first experiment is also available at doi: 10.5446/46388.

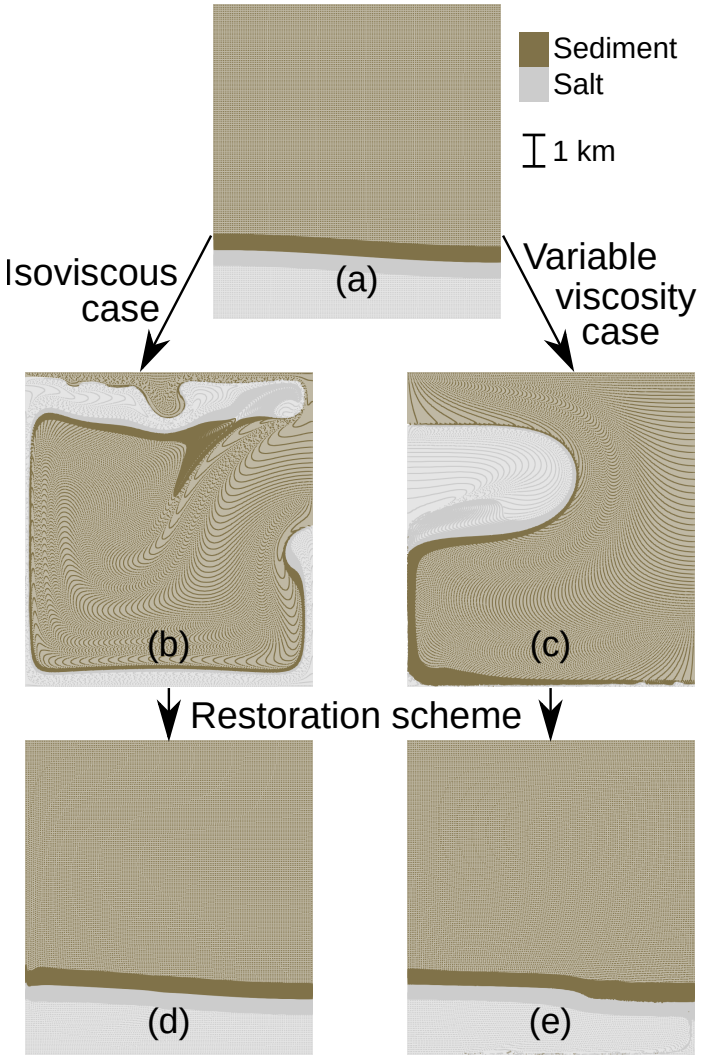

Figure 3.2: Particle swarms for the two synthetic diapiric growth experiments for the upscaled van Keken model. The darker grey and brown parts on the swarms are due to the higher density of particles around the interfaces. The particles have the same initial position (a) in the two experiments, with different material properties. The result of the forward simulation after 6×10^6 years for the first experiment is shown in (b). (c) shows the result of the forward simulation for the second experiment after 1.5×10^6 years. The results for the restoration simulations are shown in (d) and (e) for the first and second experiments, respectively.

We can see that while the isoviscous experiment has a rather smooth forward result, the second experiment with a less viscous salt leads to the creation of a salt weld (surface where the salt layer thickness has reached or almost reached zero, the salt having creeped away) at the bottom and on the left-hand side of the model.

To check the quality of the restoration in the two experiments, we compute for each

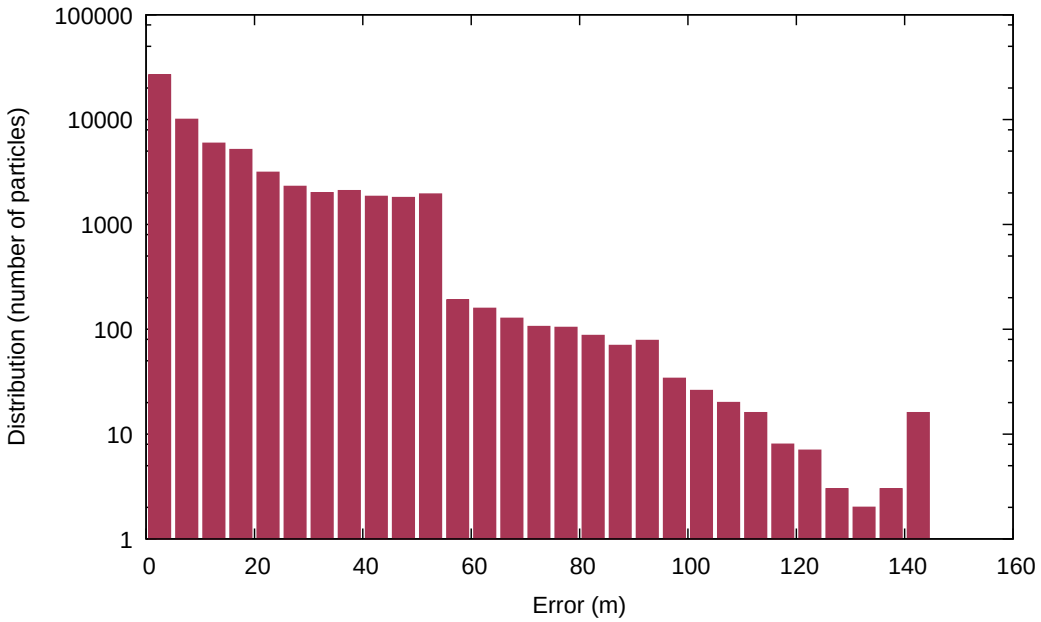

Figure 3.3: Error logarithmic distribution for the first experiment (isoviscosity) on the upscaled van Keken model.

particle the distance between its original position before the forward simulation and its position at the end of the restoration process. The mean value for this distance is 14 m (0.1% error) for the isoviscous case and 201 m (2% error) for the variable viscosity case, and the maximum value is 143 m (1.5% error) for the isoviscous case and 4947 m (49% error) for the variable viscosity case. While these results are quite good for the isoviscous case, we could think that the variable viscosity case restoration is too inaccurate. Histograms for the errors in the two experiments are given in Fig. 3.3 and Fig. 3.4, and help explain this phenomenon. The high error values in the variable viscosity case are due to the creation of a basal weld, which mixes the particles at the bottom of the model. Some of these particles are not well restored and stay at the bottom of the model, creating very large errors (hence the error bars of 1 to 20 particles with an error higher than 500 m in Fig. 3.4). The basal weld in itself creates large distortions which explain the overall large errors at the interface. This issue is also discussed by Ismail-Zadeh et al. (2001), who state the impossibility of the practical restoration of structures where the salt layer has spread in a horizontal layer near the surface. However, if we look at the model at the end of the experiments in a global way, not taking into account small irregularities, and study only the boundary between the two layers, the maximum distance between the initial model and the restored model is only 50 m (0.5% error) for the first experiment and 125 m (1.25% error) for the second, which is acceptable considering the large amount of total deformation.

3.2.2 The stratified overburden diapir model

In this second model, a salt layer is enclosed between a basement layer and an overburden that consists of multiple layers. The top of the salt layer is slightly deformed to enable movement. The domain size is 30 km horizontally and 10 km vertically. The repartition

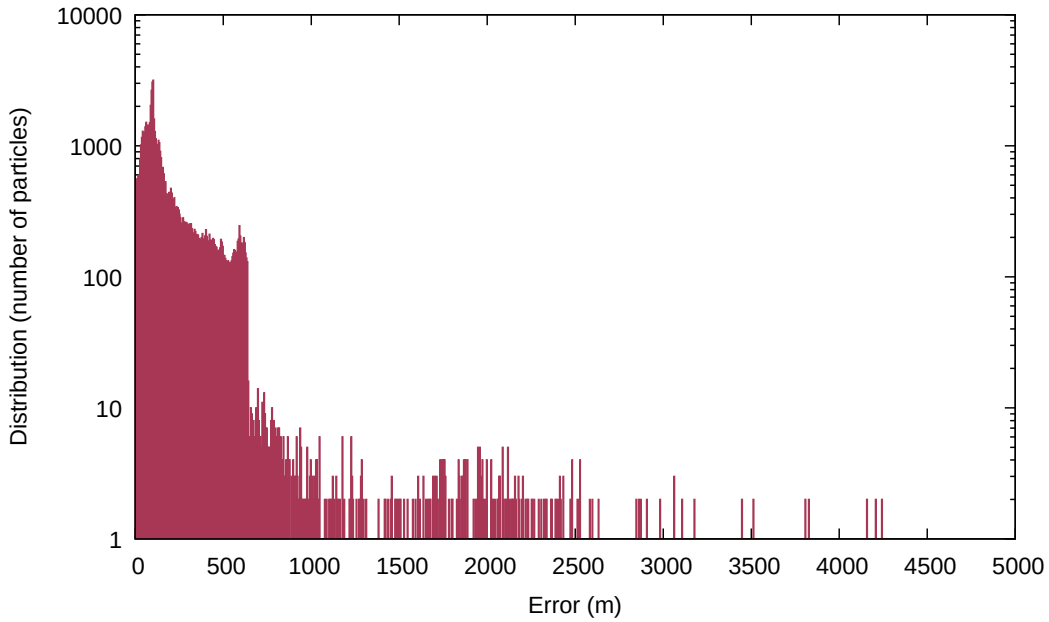

Figure 3.4: Error logarithmic distribution for the second experiment (variable viscosity) on the upscaled van Keken model.

of the material properties (ρ, η) in the layers is shown in Fig. 3.5 (a) and (b). The values are relatively similar to those of the previous experiment with the van Keken model, but the overburden has layers with slightly different material properties. Moreover, the top boundary condition is set to free slip, and the bottom of the salt layer is constrained by the basement layer. The side boundaries have a free-slip condition. The grid has 16×48 initial elements and two levels of additional adaptive refinement. The particle swarm is composed of 307 200 regularly distributed particles.

Like in the previous model, we first did a forward simulation spanning 350×10^3 years, and then we restored it. The results are shown in Fig. 3.5. We see that the restored model fits the initial state very well.

In the present setup, the movement of the salt layer depends on the folding and thinning of the sediment overburden. On both sides of the diapir, small basal welds are created. The distance between the initial position and restored position of the particles is computed, and its mean and maximum values are respectively 3 m and 639 m. A close look at the restored model shows that the particles with a high error are actually very few (Fig. 3.6) and come from the welds (Fig. 3.7). If we look at the layer interfaces, the maximum distance between the initial and restored state is 90 m, and is localized around the area of the welds (Fig. 3.8).

3.3 Introducing more geological conditions

A significant issue with the boundary conditions in geomechanical simulations is the difficulty to estimate the paleo-forces at play several kilometers deep in the underground. Because of that, they are usually simplified to fit the tectonic knowledge about the region in study. In the two models of the previous section, however, the applied free-slip and no-slip conditions may over-simplify the influence of the boundaries on the model. For

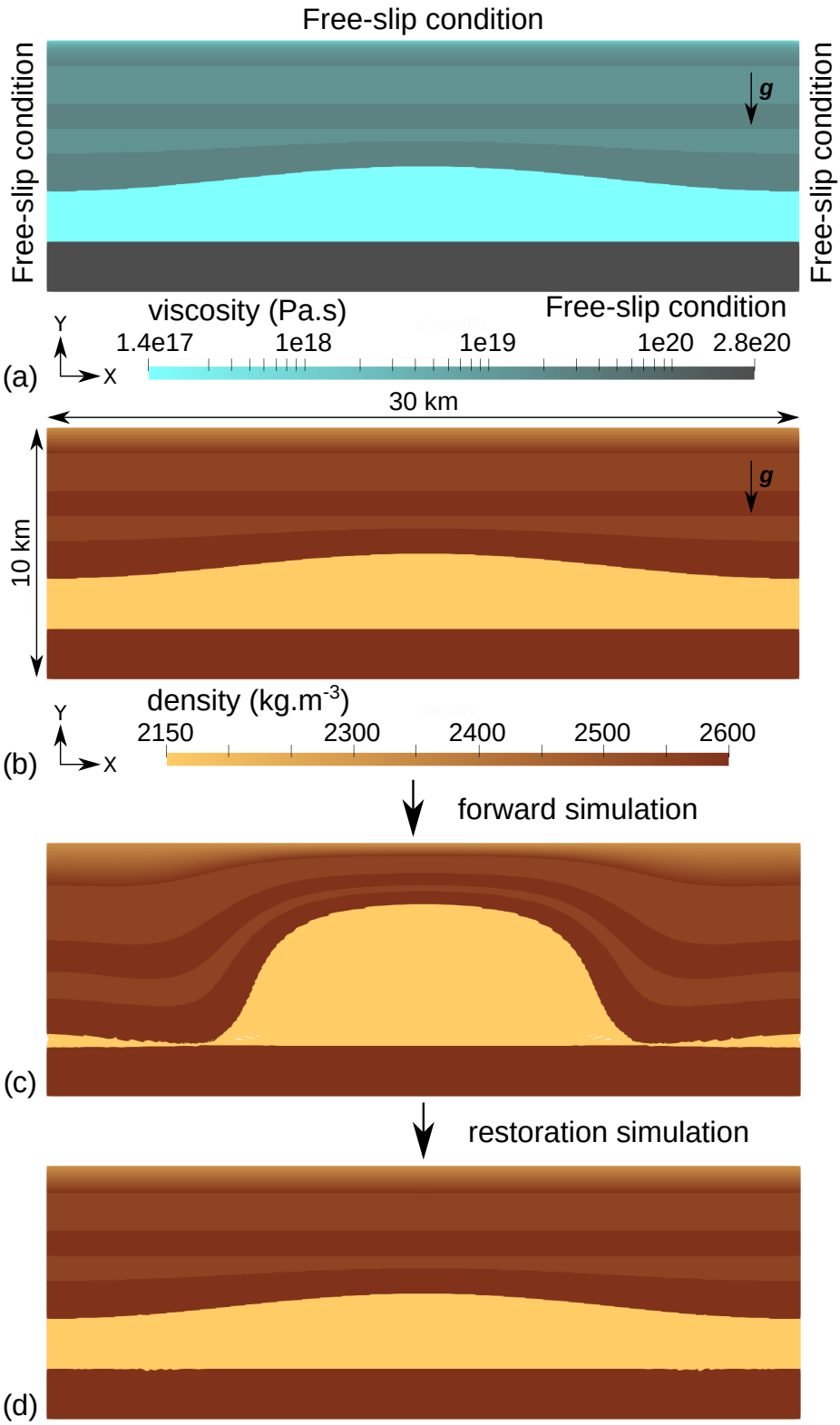

Figure 3.5: Setup and evolution of the layered overburden diapir model. (a) and (b) show the material properties in the model, with the viscosity in logarithmic scale. The results of the simulations are shown at (c) the end of the forward simulation and (d) the end of the restoration simulation.

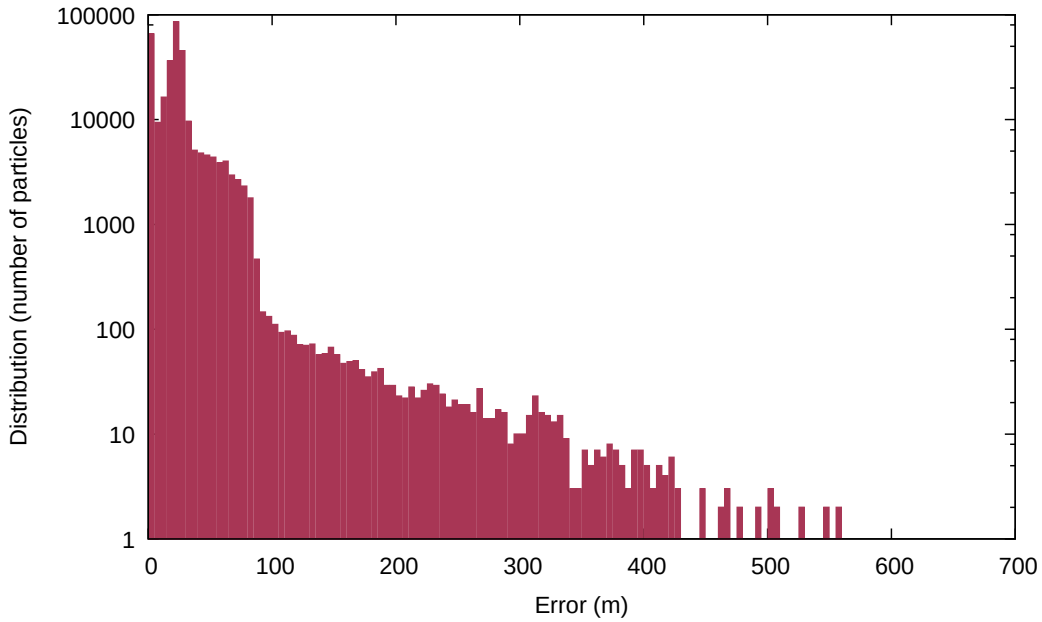

Figure 3.6: Logarithmic distribution of the error between the initial and restored model for the stratified overburden diapir model.

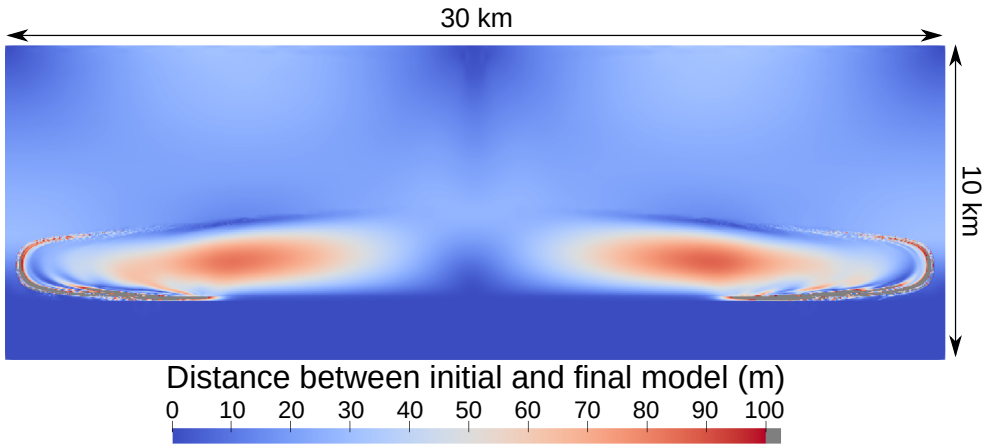

Figure 3.7: Distance between the initial and restored model for the stratified overburden diapir model. In grey, the points where the distance is larger than 100 m (1% error). We can see that those points are only located where the welds appear near the interfaces of the salt layer.

example, deformation is generally strongly influenced by the horizontal stress state, implying compressive or extensive structures and the need for corresponding conditions on the side boundaries (Chauvin et al. 2018). Another example is the top surface of the models, which can be considered as being on ground level, and is therefore in contact with air. In this section, we consider realistic boundary conditions to go further than the free-slip or no-slip boundary conditions of the previous section. First, we analyse the numerical instabilities that can appear at the air-rock interface when restoring Rayleigh-Taylor instabilities. Second, we present a model with a lateral flow boundary condition, which also includes faults, and we show how such a flow can mitigate top free surface

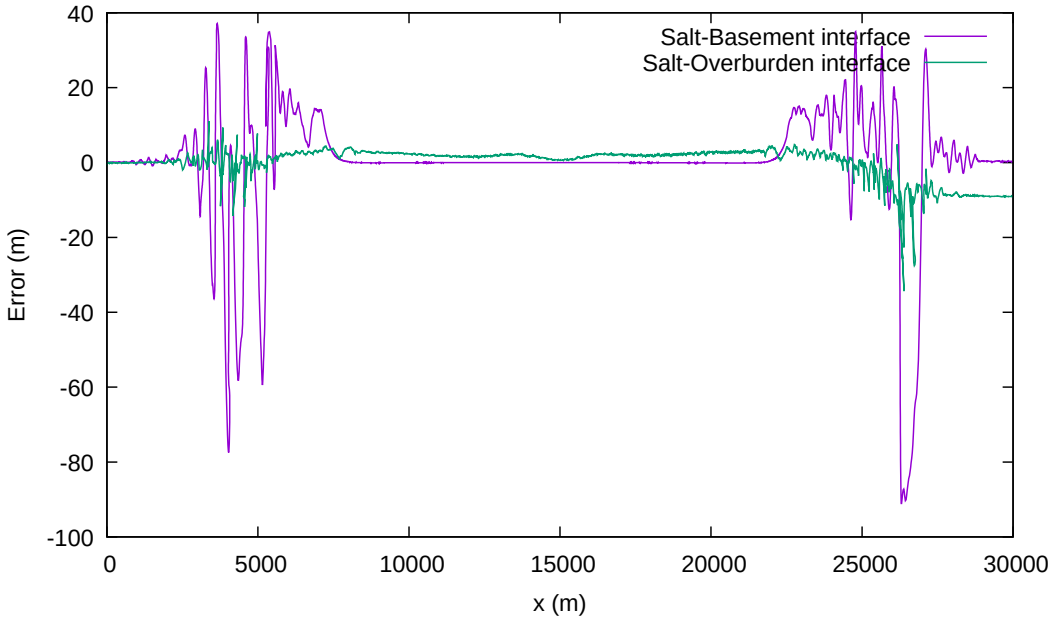

Figure 3.8: Difference between the initial and restored interfaces for the stratified overburden diapir model. The overall error is relatively small, the highest errors appear at the position of the welds for the interface between the salt layer and the basement layer (highest viscosity contrast).

instabilities.

3.3.1 Dealing with the free surface in a backward creeping flow scheme

The interface between air and the top surface of a model is complicated to handle due to the several orders of magnitude in the material property contrast (very high density and viscosity for rocks versus almost null density and viscosity for the air). In geomechanical simulations, several approaches exist to model its behavior. The simplest topographic surface solution is to set a free-slip condition which removes the normal component of the velocity at the boundary. This simplification is mostly used in cases where the movement of the top surface is negligible compared to the rest of the model, such as the two test models presented in previous Section 3.2. A more physical way of considering this interface is to use a free surface on the top of the model. The free surface implementation presented in Section 2.2.5 performs well in forward simulations (e.g., benchmarks 2.3.4, 2.3.5), but in restoration simulations the results are more mitigated. Indeed, in models where the only drive is a density contrast (such as the models in previous Section 3.2), the free surface shows instabilities, as can be seen in Fig. 3.9.

This appears particularly when working with models that have a near-horizontal top surface. In those setups, any small computational error in the vertical part of the velocity can lead to instabilities that increase exponentially in reverse time. This increase is due to the fact that the problem is gravity-driven: if part of the model rises too high or low (compared to the real retro-deformation state), the computed velocity inside the model will be respectively negative or positive in the vertical direction. In forward simulations, this behavior naturally removes the instabilities, and the model

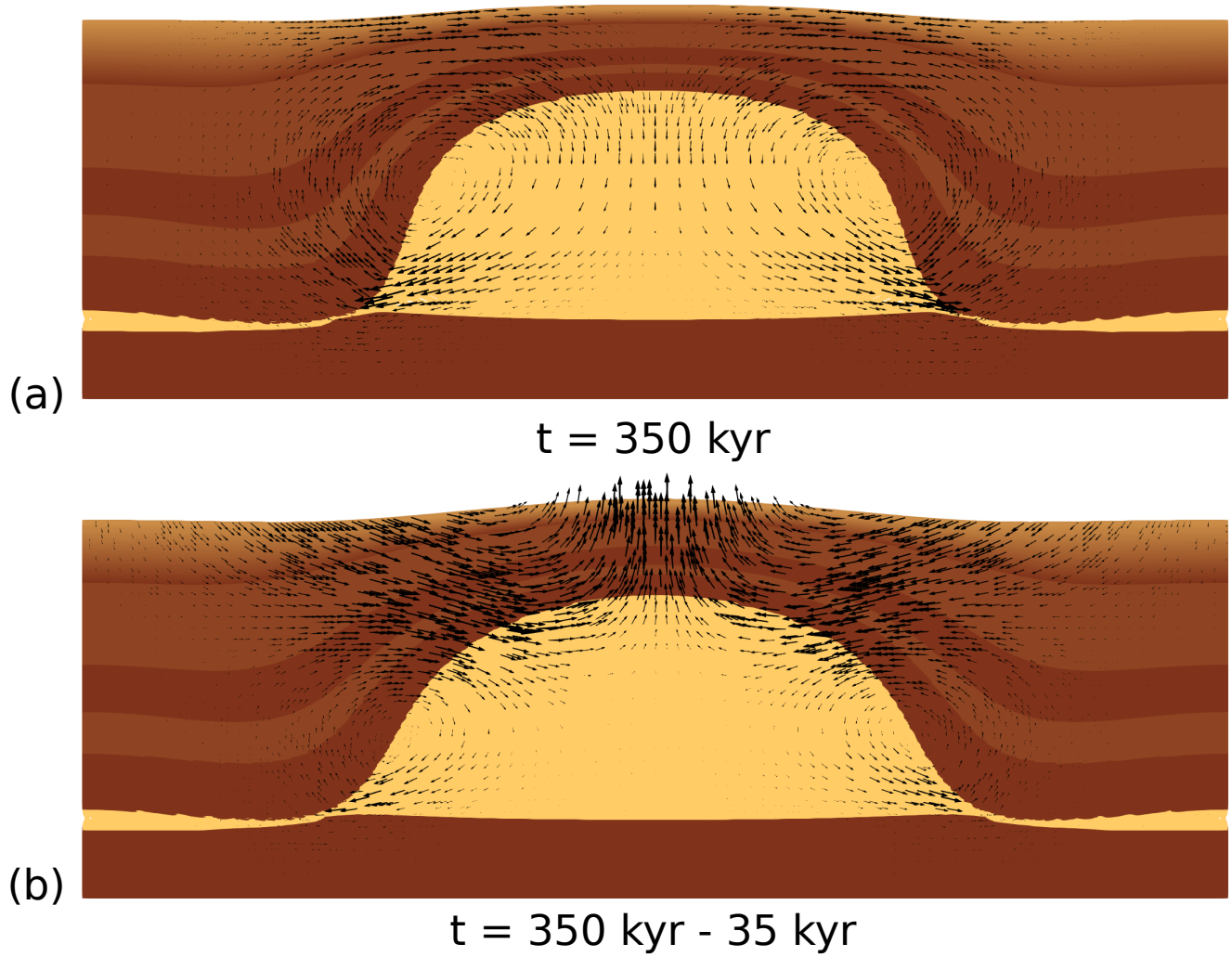

Figure 3.9: Example of the instability that appears in the restoration of the stratified overburden diapir model (Section 3.2.2) with a free surface on top. The black arrows show the movement applied by the backward advection scheme. In (a), the state of the model presented in Section 3.2.2, after 350 kyr of forward simulation with a free surface. The top surface is quite flat, but we see in (b) that after a few timesteps of backward simulation, instabilities appear at the near-flat free surface, which cause the middle of the top surface to rise up, making the computed velocity to increase exponentially.

continues towards an equilibrium state. When applying a backward scheme, however, the velocity is applied with a negative sign, like in Eq. (1.13), and the parts of the top surface that are too high or too low end up even higher or even lower, respectively. This leads to a cycle of the velocity increasing exponentially to bring down (or up) the parts of the model where the free surface altitude exponentially increases (or, respectively, decreases).

Several approaches involving specific tractions on the top surface have been tested to remove this instability. These tests include using various values of a homogeneous traction on the top, an adaptive traction aiming at flattening the top surface, and a traction aiming at removing instabilities on the velocity values. We have, however, not yet devised any efficient means to prevent it in such setups. In particular, the FSSA

delays this phenomenon, but does not suppress it altogether. Similarly, the sticky air approach can delay the instabilities that appear in some models driven exclusively by gravity, but does not remove them. In the next chapter, we introduce a horizontality criterion on the top surface. While we use it for checking the quality of the restoration results, it can also be used to detect the appearance of such instabilities in the model (and stop the simulations at this point).

3.3.2 The simplified graben model

In order to test the free surface behavior on setups where deformation is not driven only by Rayleigh-Taylor instabilities, boundary conditions including lateral flow are introduced, to model an extensive context. In such setups, the boundary conditions may create strains that damp the free surface instabilities. As the deformation in this kind of extensional behavior is highly driven by faults appearing in the sedimental layers, shear zones are also added. This makes the conditions used here more realistic, as faults and horizontal displacements have been acknowledged to play a key role in salt tectonics (e.g., Daudré and Cloetingh 1994; Brun and Fort 2011).

The model designed to adress this issue is a simplification of the creation of a graben in sediments submitted to lateral flow in an extensive context, as shown in Fig. 3.10.

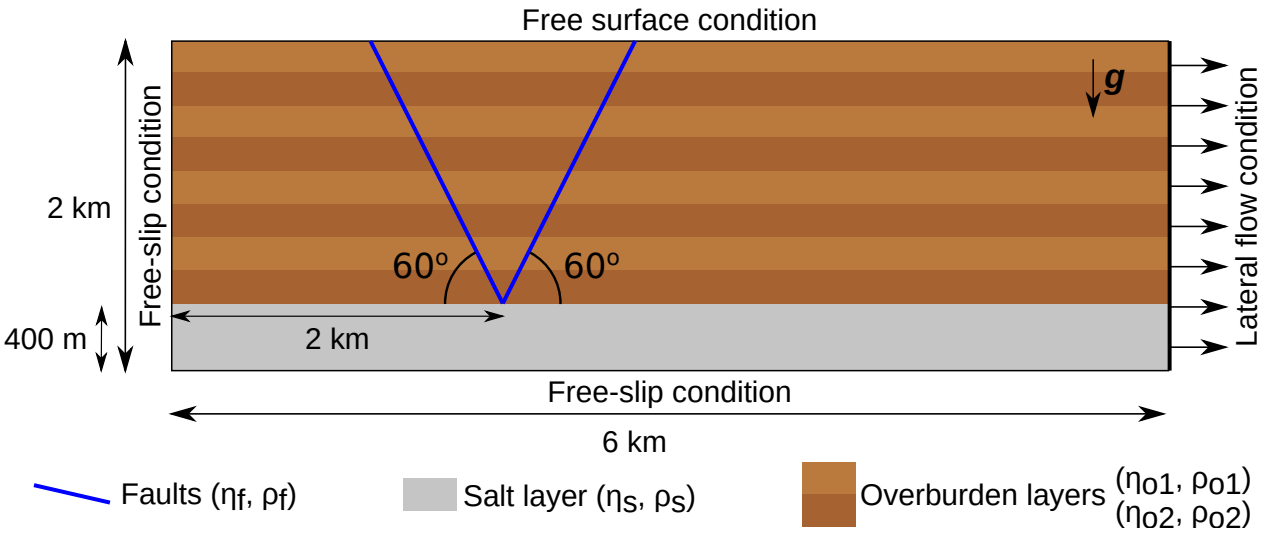

Figure 3.10: Setup of the simulation for the simplified graben model. The initial particle swarm is densified near the faults and at the interface between salt and sediment.

It consists of a layered overburden underlain by salt and cut by two 60° faults. As the intent of the manuscript is to focus on the restoration of structural models, we do not consider the formation of the faults with plasticity, but rather start with two faults already present. The faults are considered as shear bands with a thickness of 10 m where the viscosity and density are lower than the rest of the overburden. The overburden is layered with two types of rocks with slightly different density and viscosity. Material properties inside the model are as follows:

- Overburden type 1 layer : $\eta_{o1} = 1.5 \times 10^{19}$ Pa.s, $\rho_{o1} = 2550$ kg.m^{-3}
- Overburden type 2 layer : $\eta_{o2} = 5.0 \times 10^{19}$ Pa.s, $\rho_{o2} = 2600$ kg.m^{-3}

- Salt layer : $\eta_s = 1.0 \times 10^{17}$ Pa.s, $\rho_s = 2160$ kg.m^{-3}
- Faults : $\eta_f = 1.0 \times 10^{16}$ Pa.s, $\rho_f = 2200$ kg.m^{-3}

The domain size is 6 km horizontally and 2 km vertically, and the right boundary is subjected to lateral flow. This is modeled by a Dirichlet condition applying a specific value for the velocity in the horizontal direction (the vertical value for the velocity is still free, as with free-slip boundary conditions). The left and bottom boundaries are set to free-slip, and the top boundary is a free surface. For the model to evolve without interference with the lateral flow on the right boundary, the faults are positioned at one third of the model width from the left. In order to capture the geometry of the faults, which is essential in this setup, the adaptive refinement of the grid is an important feature of the FAIStokes implementation. As such, the grid is refined specifically near the faults, with 60×20 initial elements and four levels of adaptive refinement (up to 6.25 m $\times$ 6.25 m cells near the faults), as shown in Fig. 3.11 for the first time step.

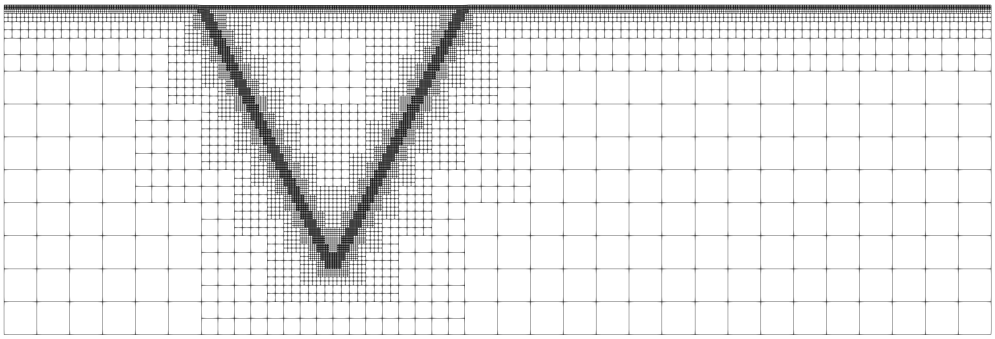

Figure 3.11: Adaptively refined grid for the first time step of the simulation on the simplified graben model. We can see that the grid is refined to a high level near the faults, where the velocity gradient is high. On the contrary, it is coarsened where the velocity has small gradients, particularly in the lower right and left corners.

Like in the models of Section 3.2, a forward simulation is run first, and then the restoration scheme is applied on the obtained model. The lateral flow is set to 10 mm/year outwards and the model is observed for 35 000 years, both in forward and backward simulations, to have sufficient deformation. The particle swarm has a heterogeneous particle density, with a regular sampling in most of the model and eight times more particles near the faults and around the interface between the salt and the overburden. The average distance between two particles in the densified zone is 2.5 m. The total number of particles at the first step of the simulation is about 330 000. This number decreases during the forward simulation, as the particles are removed once they flow outside of the model. During the restoration simulation, new particles are added near the right boundary when the particle swarm flows inward due to the negative time stepping. Their material properties are determined from the particles moving inwards and their motion. The model at the end of the forward and backward simulations is shown in Fig. 3.12.

Figure 3.13 shows the difference between the position of the interfaces before the forward simulation and at the end of the backward simulation. The numbering of the interfaces follows their position in the model, interface 0 being the lowest salt-sediment

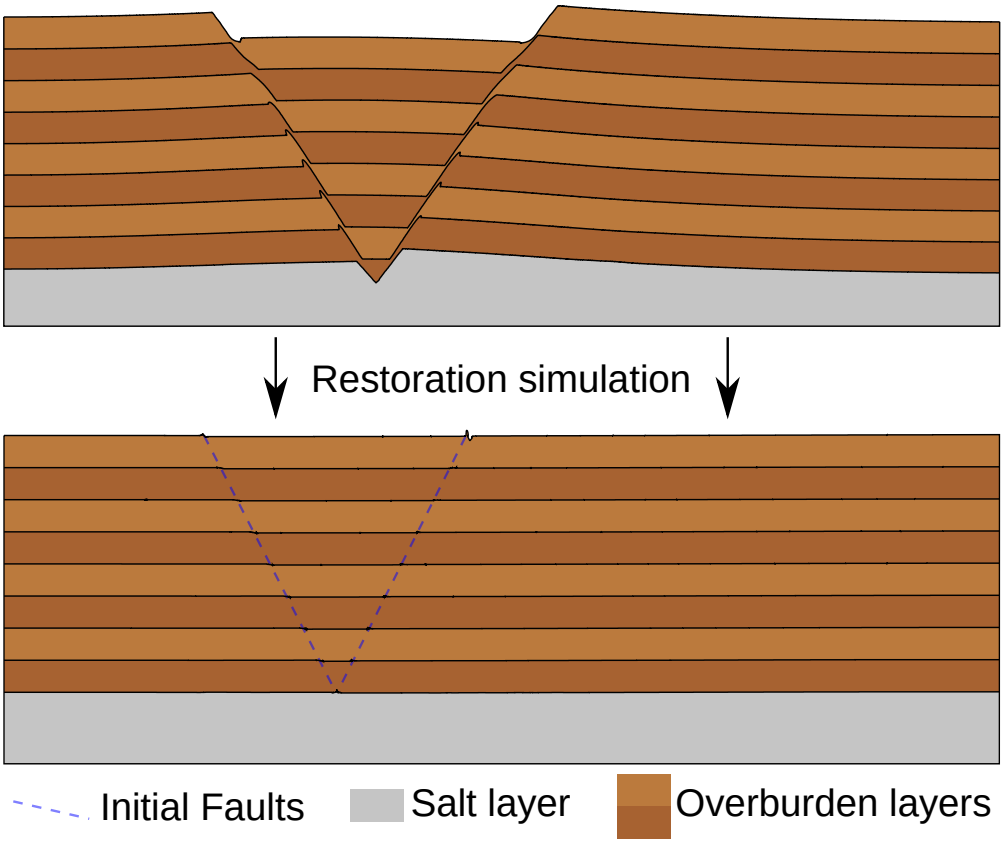

Figure 3.12: Results of the simulations for the simplified graben model at (a) the end of the forward simulation and (b) the end of the restoration simulation.

interface. The mean and maximum errors for each interface are given in Table 3.1.

Table 3.1: Mean and maximum errors for the restoration of each interface of the simplified graben model.

	Mean error (m)	Max error (m)
Interface 0	1.5	16.5
Interface 1	1.7	7.2
Interface 2	1.9	10.9
Interface 3	2.1	9.8
Interface 4	2.3	9.1
Interface 5	2.4	8.6
Interface 6	2.6	8.5
Interface 7	2.7	7.1
Top Surface	2.9	31.4

Overall, the results for the restoration simulation are satisfying, with mean errors around 1% of the forward deformation for the layer interfaces. Figure 3.13 shows that the graben part of the model (between the two faults) is approximatively 7 m lower than it should be at the end of the restoration. This is due to the model topography being slightly tilted from the right-hand side of the model towards the faults at the end of the restoration.

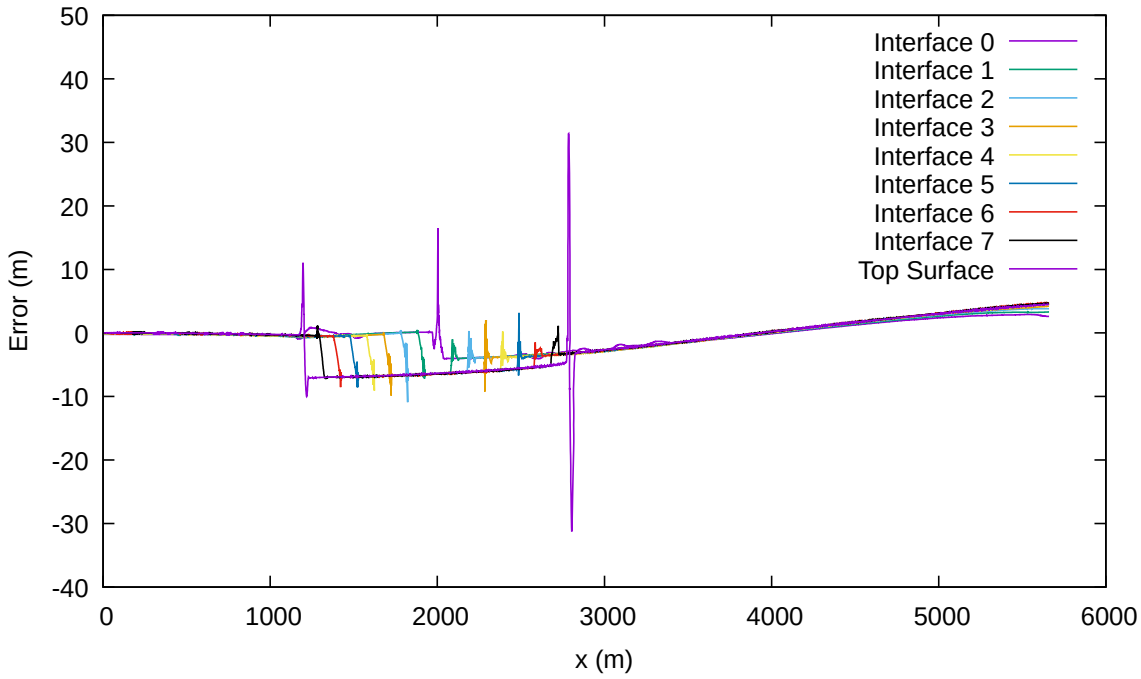

Figure 3.13: Error on the restoration of the interfaces in the simplified graben model. The lower the number of the interface, the lower the interface it corresponds to. For example, interface 0 is the interface between the salt and the lowest sediment layer.

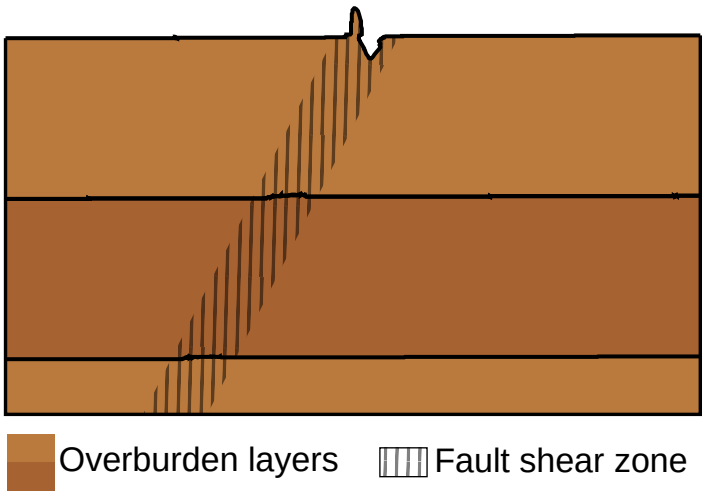

Figure 3.14: Zoom on the top of the right fault of the model at the end of the restoration simulation, for the simplified graben model.. While the sediments on both sides of the fault stay mostly flat, instabilities appear at the top of the fault due to the higher viscosity of the shear zone material.

The largest errors are located on the two faults. In particular, the free surface behaves quite well during the simulation, except at the upper tip of the faults where some instabilities occur. These instabilities are the same as those presented in previous Subsection 3.3.1, and appear at this point due to the faults' higher viscosity (cf Fig. 3.14). The error resulting from these instabilities, however, is quite small compared to the amount of deformation in the model (around 200 m of slip on the faults).

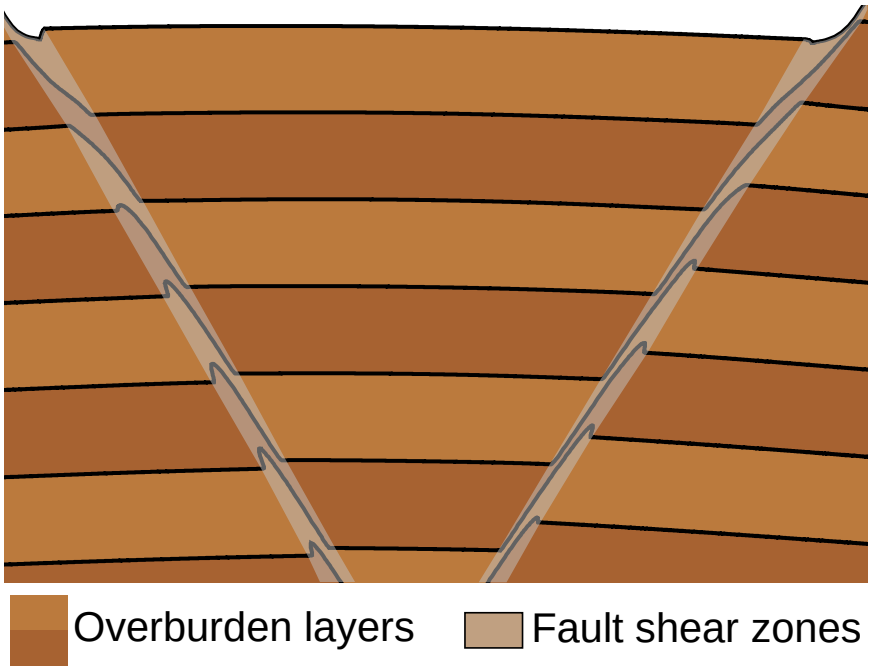

Figure 3.15: Zoom on the fault shear zones after the forward simulation. We can see that the flow of the sediments is inhomogeneous, and some interfaces flow higher than others inside the shear zone modeled by a lower effective viscosity.

Another interesting feature of the model is the behavior of the fault shear zones: while the faults have the expected effect on the global model, the flow inside the shear zones modeled by a higher viscosity is peculiar, as can be seen in the zoom of the forward simulation result in Fig. 3.15. One could think that this is due to errors in the velocity computation or the particle advection steps. If it was the case, however, we would expect these errors to grow during the restoration simulation. However, the interfaces go back to a flat state inside the shear zone during the restoration process, so we can dismiss this hypothesis. To understand this phenomenon, I think it is necessary to take a step back and look at the global deformation of the model. Looking at the middle part of the graben, we can see it folds slightly in an anticlinal way. This minor folding does not affect the rest of the model, but may be compensated by a succion flow inside the fault shear zones that have a lower viscosity. This could explain the non-homogeneity of the flow inside the faults: the interfaces closer to the middle of the graben are pulled upwards to fill the gaps created by the graben folding.

3.4 First assessment of the choice of parameters

In the previous sections, the model setups were designed and built to address specific questions, and the model geometry at the beginning of the restoration simulation came from the forward simulation of a known model. The material properties to apply inside the model were known, as well as the deformation the model underwent. While this allowed to compute a measure of the error during the restoration process, things are more complicated in real-case applications. Indeed, the material properties inside a model are usually not known. Likewise, the geological knowledge of an area can only give us a

rough idea of its deformation history. The model we introduce in the present section has a simple setup but is interesting for two reasons. First, it was not created by a forward viscous simulation, and the deformation history is not known. Second, it is uncertain whether the rheology applied on the sand and sediments and the boundary conditions will restore it. Therefore, this test case can be assimilated to the simplification of a real case application.

The model was generated with the method proposed by Clausolles et al. (2019). It consists of a salt diapir that mimics passive diapirism structures created by syn-deformation differential sediment loading. The input for the salt diapir is a seismic image interpreted to segment it in three regions: salt, sediment, and uncertain. The salt-sediment interface is then generated in the uncertain zone, from available data, geological knowledge and a random scalar field that takes into account the uncertainties. The initial particle swarm contains 102 510 particles sampling the model regularly, and we apply free-slip boundary conditions on the top and side model boundaries, and a no-slip boundary condition on the bottom. Figure 3.16 shows the initial state of the model. The grid has 48×80 initial elements and three levels of additional adaptive refinement. In order to assess the influence of the value of the parameters on the results of the restoration, we tested different possibilities. For the density, the value for salt rock is $\rho_{salt} = 2160$ kg.m^{-3}, while the value for sediments can vary depending on the type and origin of deposition mechanisms; we considered here a value $\rho_o \in [2600; 3300]$ kg.m^{-3}. For simplicity, we set the viscosity of the salt layer at $\eta_{salt} = 10^{17}$ Pa.s and only vary the viscosity of the sediments $\eta_o \in \left[10^{19}; 10^{21}\right]$ Pa.s in order to test the effect of the contrast. As a result, we did five experiments with different values of ρ_o and η_o:

- Exp.1: $\rho_o = 2600$ kg.m^{-3}, $\eta_o = 10^{19}$ Pa.s
- Exp.2: $\rho_o = 3300$ kg.m^{-3}, $\eta_o = 10^{19}$ Pa.s
- Exp.3: $\rho_o = 2950$ kg.m^{-3}, $\eta_o = 10^{20}$ Pa.s
- Exp.4: $\rho_o = 2600$ kg.m^{-3}, $\eta_o = 10^{21}$ Pa.s
- Exp.5: $\rho_o = 3300$ kg.m^{-3}, $\eta_o = 10^{21}$ Pa.s

As this is a simplification of a real case application, and because there is no information on the type of sediments, in each experiment the density and viscosity are homogeneous in the sediment and salt layers.

The results for the five experiment simulations are given in Fig. 3.17. A video of the restoration of Exp. 3 is also available at doi: 10.5446/47889. Depending on the experiment, we choose to stop the restoration process after different durations t_{end}. Indeed, as the viscosity and density vary from one experiment to the other, so does the model relaxation time.

Overall, the restoration process removes the diapir and leaves a salt scar, while the sediment layers remain globally flat. Since this setup is generated by a method for syndeformation diapirs, a more relevant restoration of the model should have taken into account the deposition of the sediments simultaneously the formation of the diapir, by removing the sediment layers one by one. For simplification purposes, such sedimentation processes were not implemented. In this case, the stress state inside the model

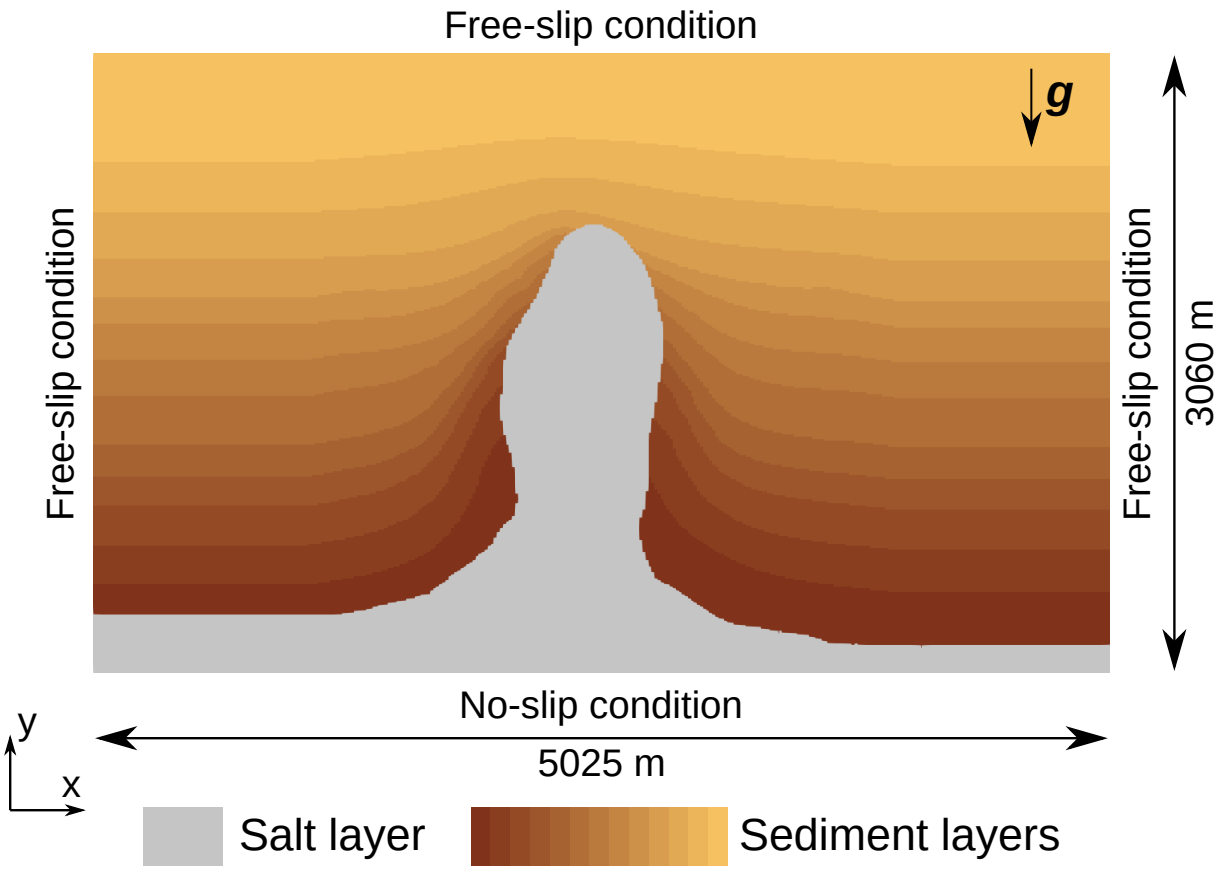

Figure 3.16: Setup of the simulation for the model generated with the method proposed by Clausolles et al. (2019). The initial model is sampled on a regularly spaced particle swarm.

being incorrect, the sediment and salt layers could not be restored to a completely flat state. For example, the shallow sediments should have been removed early in the restoration process. Because they have not, their backward deformation continues at times when they should not have been deposited in the model yet. Despite such a high level of simplification, the results are convincing, and we see that the salt diapir is a result of upbuilding and not downbuilding.

The analysis of the five experiments shows that in this setup, the viscosity contrast between salt and sediment and the density of the sediments do not have a big impact on the shape of the model after the restoration process. Only the shape of the sediments at the base of the diapir is slightly different from one experiment to the other. Experiments 4 and 5 have serrated shapes that are not geologically probable, probably because of the four orders of magnitude of viscosity contrast between the salt and sediments. The main difference between the experiments is the relaxation time for each restoration process. If the duration of the formation of the diapir was known, it could then be used to reduce the uncertainty on which density and viscosity to use. The curvature of restored layers also changes between the simulations, which could provide another criterion to further evaluate the results (but would call for variable sediment viscosity testing). However, this is a difficult path forward, because sediment deposition clearly plays a major role during salt displacement, and conversely (e.g., Giles and Lawton

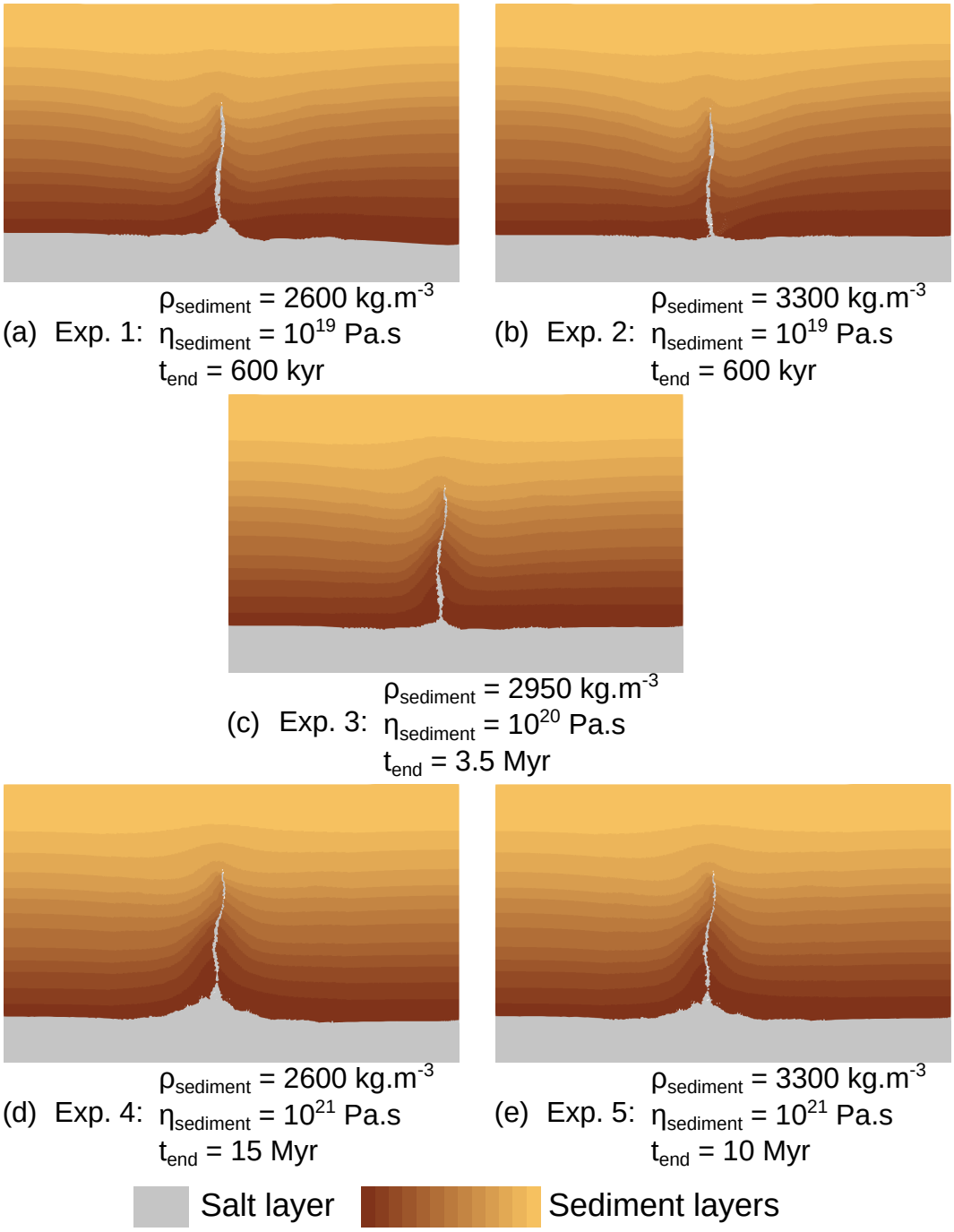

Figure 3.17: Results of the five restoration experiments done on the salt model setup of Fig. 3.16, after different time spans t_{end}.

1999; Hudec and Jackson 2007; Rowan et al. 2012).

3.5 Discussion on the results

When applying a reverse-time Stokes restoration scheme, two important questions appear: what are the material properties of the geological objects inside the model, and what type and intensity of boundary conditions should be applied to these geological

objects? Regarding the material properties, the diapir test model of Section 3.4 gave a first idea of how to choose them, and previous articles have considered the question on specific setups (e.g., Lechmann et al. 2010). The density of the subsurface depends on the type of rocks involved and their burial history, and its estimation is relatively easy. The viscosity, however, is not trivial, as laboratory observation timescales are too short to reflect the slow movement occurring at geological timescales. The values we took are inspired from numerical simulations, but they have a large uncertainty (at least one order of magnitude) (e.g., Massimi et al. 2006; Kronbichler et al. 2012), as they are calibrated using postglacial rebound data for example. Moreover, the effective viscosity to use may change through time, with temperature and the level of compaction for example. Working on analogue sandbox experiments and further experiments on models with more geological knowledge should be useful in estimating a proper viscosity for the restoration of different rock rheologies. In particular, the duration over which the geologic phenomena occur could guide the choice of viscosity values in subsurface models.

Regarding the rheology of faults, we cannot directly use their usual forward modeling implementation considering the rock as having a plastic behavior. Indeed, the previous stress history is needed to simulate such a behavior, and it is not available in restoration, which studies backward movement. In Section 3.3.2 we used a specific viscosity for the implementation of faults in restoration, which holds two advantages. First, since all the faults are already identified at the beginning of the restoration process, we do not need to allow the creation of faults in backward simulations. Second, using an effective viscosity allows for a more realistic simulation of the faults, compared to previous geomechanical restoration schemes. Indeed, viscous behavior may model both the shear band and the damage zone, and simulate the friction inside them, which considering the faults as free-slip surfaces cannot.

A significant issue with the boundary conditions in geomechanical simulations is the difficulty to estimate the paleo-forces at play several kilometers underground (Lovely et al. 2012). We therefore need to choose Dirichlet and Neumann boundary conditions that best fit the tectonic knowledge about the region of study. In the two test models of Section 3.2, boundary conditions are either free-slip or no-slip, which is a strong simplification of reality. Considering the top surface of the models, which usually is in contact with air, as a free surface would be a great improvement, but is challenging in practice. In models driven only by Rayleigh-Taylor instabilities, particularly, any small error or instability at the top free surface grows exponentially, as seen in Section 3.3.1. Introducing more geological factors such as horizontal displacements, whose importance in the deformation of salt structures has been proven, may provide a solution. Indeed, we have shown here that conditions such as lateral flow introduce other drives for the simulation, which can damp such instabilities in an efficient way. It does not remove them completely, however, once the top surface is restored.

Overall, this chapter showed that using Stokes flow for structural restoration produces consistent results on different analytical model setups. A first assessment of ways to model fault with an effective viscous rheology was also introduced, as well as the influence of material parameters on restoration simulations where they are not known.

Chapter 4

Restoration of an analogue model

Contents

Abstract In this chapter, the creeping flow restoration method is applied to the restoration of a laboratory analogue experiment. I first present the analogue experiment, the available data and the model which was created. Secondly, I introduce the first tests that were done on the model, in order to assess the impact of the conditions that are chosen for each boundary. Lastly, I show the tests that were done in order to determine the effective material properties inside the model which allow the best restoration simulation.

4.1 Introduction

In basin studies and structural geology, laboratory analogue experiments, also called sandbox experiments, are boxes filled with different materials which represent geological layers or objects (Hall 1815; Willis 1894). The idea is to choose materials which are sufficiently weak to have the same deformation mechanisms as areas that are geologically interesting, but at laboratory scale (Ramberg 1981; Cobbold et al. 1989). For example, the experiment we use here has a size around 30 cm $\times$ 5 cm and lasts about 3 hours, but the properties of its materials are such that its deformation is similar to that of a sedimentary basin several kilometers wide, over several hundreds of thousands of years.

The advantage of using a model of a laboratory analogue experiment, in our case, is that the state of the model before the deformation is known and can be compared to the restored model. This allows a validation of the restoration process where the model in study does not come from a forward simulation based on the same physical equations, rheology, material properties and boundary conditions. Moreover, as some parameters are already known, it allows a more precise assessment of the impact of the other parameters. In the first section of this chapter, I present the analogue experiment and the available data to show how the particle swarm to input in FAIStokes was built and distinguish the parameters which are known from those that need to be estimated. I then present the tests that were focused on the conditions at the boundaries of the model, and on the way to make them as physical as possible. Finally, I use the boundary conditions determined as the most 'natural' to estimate the effective viscosity to apply to the sediment layers and to the fault shear zones.

4.2 From the laboratory experiment to the numerical model

The model used here comes from the deformation of a structural sandbox experiment made by IFPEN[1] and C&C Reservoirs[2], 2016, DAKS ^{TM} (Digital Analogs Knowledge

[1] https://www.ifpenergiesnouvelles.fr
[2] https://www.ccreservoirs.com

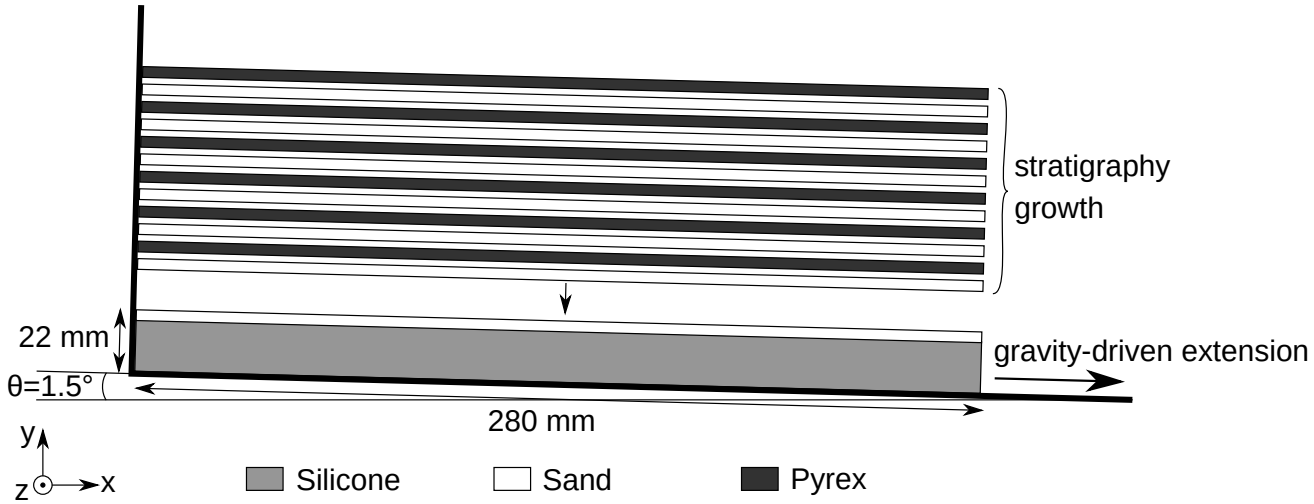

Figure 4.1: Setup of the creation of the laboratory analogue model. A layer of 18 mm of silicone and a layer of 4 mm of sand are first deposited on a slab with an open boundary. The slab is then tilted with an angle $\theta = 1.5°$, and the layers start to deform with gravity in the direction of the open boundary. During the 256 min of the experiment, 12 new layers of alternatively pyrex and sand are deposited, flattening the topography and simulating stratigraphy growth.

System) to reproduce extensional salt structures (Fig. 4.1). Two initial layers were deposited in the model box, forming the pre-growth strata: a layer of 18 mm of silicone SMG 36 and a layer of 4 mm of sand. The model box was then inclined with a 1.5° angle to simulate a basinward tilt, inducing gravity-driven extension. The experiment lasted for 256 min, during which 12 new layers of alternatively pyrex and sand were deposited to simulate stratigraphic growth. These new layers flattened the topography by filling the depressions. The model resulting from the experiment was analyzed with X-ray computerized tomography. This method allows the computation of cross-sections without physically cutting it. As such, it is non-destructive, does not need the consolidation of the model beforehand and avoids the deformation that could occur during the cutting. Moreover, it is dynamic, so it can be used to track the evolution of the experiment. The differentiation of the layers in the cross-sections is done using the difference in density and X-ray attenuation.

Analogue experiments can be used for the validation of structural models, for fracture and fault analysis, and for understanding the evolution of the structures resulting from the imposed conditions. In our case, the analogue experiment is used to validate the restoration process and find the best restoration parameters in the case of sedimentary basins including salt and processes of sedimentation and lateral extension. I made the choice of working at the scale of the laboratory experiment (width of 280 mm and duration of 256 min), where the viscosity of the silicone layer (mimicking salt rock) is known, to reduce the amount of parameters to test.

4.2.1 Available data

Various data are available for this analogue experiment. First, the experiment setup is given, as shown in Fig. 4.1. Second, the physical properties of the silicone, sand and

Table 4.1: Physical properties of the silicone, sand and pyrex layers for the analogue experiment. In dark red, the properties that are not relevant due to the difference in rheology between brittle and ductile layers. From the IFPEN documentation on the analogue model experiment (IFP and Reservoirs 2006).

Physical properties	Sand	Pyrex	Silicone SGM36
Rheological behaviour	Brittle		Ductile (Newtonian)
Density	1.3 - 1.5	1.2	0.97
Grain size (μm)	100-120	80-120	
Internal friction angle	40°	32-36°	
Cohesion (mPa)	0.001-0.002	> 0.005	
Viscosity (Pa.s)			5.10^4
Natural analogue	brittle rocks (sandstones, limestones)		ductile rocks (salt, undercompacted shales)

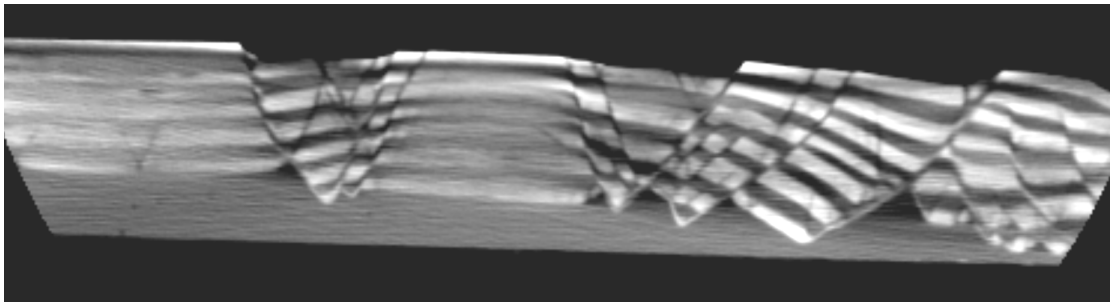

Figure 4.2: Cross-section of the analogue experiment at its end. The image has been obtained using X-ray tomography, a non-destructive method for structural analysis of the sandbox experiment. The resolution is 0.62 mm per pixel. As the range of the imaging is limited, the borders of the experiment are not present on the image.

pyrex layers are known (cf Table 4.1). Third, X-ray tomography images are available; they have been taken every two minutes and their resolution is 0.62 mm per pixel. No images have been taken during the deposition of sand and pyrex layers, so there are small time gaps at these moments. As X-ray tomography is sensitive to density, layer interfaces can be hard to pinpoint where the density contrast is weak. In this case, the analysis of the images at previous times can help to discern the position of the interfaces throughout the deformation. The state at the end of the experiment has been analysed with a series of cross-sections made with tomography, so a 3D structural model can be built. In the present work, we used only one of the cross-sections (shown in Fig. 4.2) to test the method. While this ignores out-of-plane displacements, it reduces significantly the computation time for the restoration process, so that more tests on the impact of the different restoration settings can be performed.

4.2.2 Creation of the numerical model

To digitize the cross section in Fig. 4.2, this latter was first rotated (to get rid of the tilt of the experiment, later added directly in FAIStokes, as explained in Section 2.2.3) and cut to a rectangular shape. The GUI presented in Section 2.2.1 was then used to

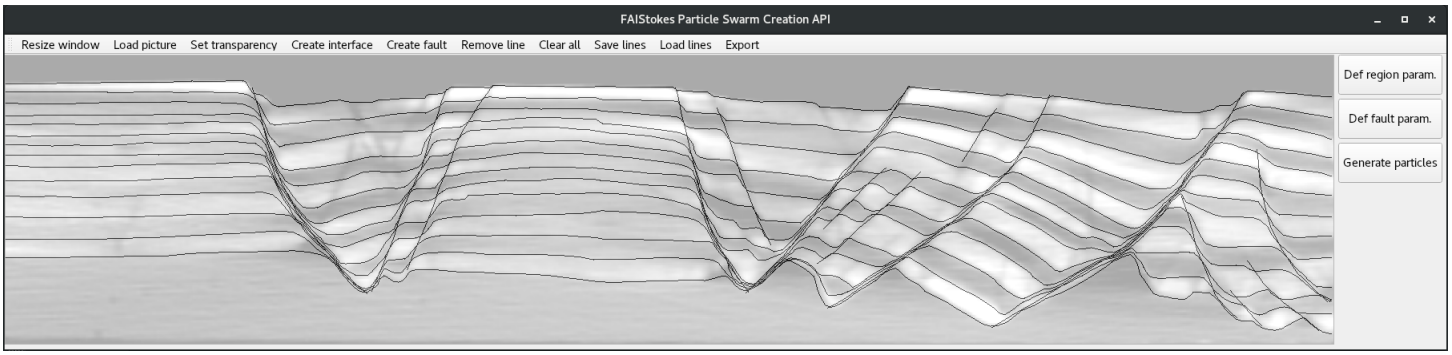

Figure 4.3: Digitization of the cross-section of interest with the FAIStokes GUI. The interfaces and faults were digitized to create the particle swarm to input in FAIStokes.

digitize the interfaces and the faults in the cross-section (Fig. 4.3). Finally, a particle swarm was created, and the fault and interface lines were used to define the layers and determine the material properties of the particles. The layers and faults were indexed and their indices were also kept as parameters (to remove specific layers, for example). The particle swarm contains 667 087 particles at the beginning of the restoration, with a distance of 0.14 mm between each particle.

In the faults, the viscosity of the particles is minimal at the position of the fault line (representing the fault core), and increases with a power-law until reaching the fault border. The distance between the fault core and the fault zone border, defining the shear band thickness, is different for each fault (cf Table 4.2). Indeed, a close look to the cross-section Fig. 4.2 shows that each fault has a different range of deformation around its core.

The final model can be seen in Fig. 4.4.

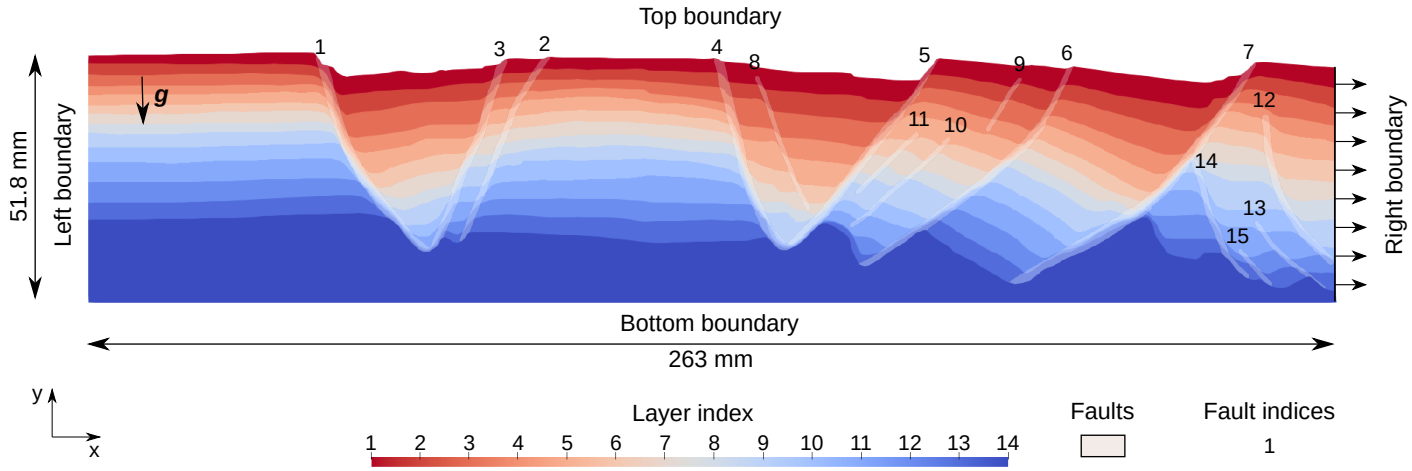

Figure 4.4: Setup of the analogue model to input in FAIStokes for the restoration simulations. The model boundary conditions are not specified here, as their choice and impact on the simulations is discussed in the next section. During the simulations, the tilt of the model is introduced by rotating the gravity vector, as explained in Section 2.2.3.

As the time between the deposition of two layers varies and could not be found in the available report, it was determined from the number of images taken between the deposition of one layer and the next (as the images are taken every 2 min). This also

Table 4.2: Fault shear band thickness in the analogue model. The values come from the analysis of the cross-section Fig. 4.2. The index of each fault is given in Fig. 4.4. The faults with two values have a shear thickness that is reduced at the top of the model because they have a lower deformation range there.

Fault index	Fault shear band thickness (mm)
1	2.2
2	1.4
3	1.8
4	2.1
5	1.2-2
6	1.2-1.8
7	1.6-3
8	1
9	1
10	1
11	1
12	1.6
13	1
14	1.4
15	1

allowed us to estimate the time gaps during the deposition of each layer; we found that each gap lasts around 5 min. This missing time and the evolution of the experiment during the deposition of the layers has not been taken into account in the restoration simulations, for simplicity purposes. The time between each layer deposition was used as the restoration duration (Table 4.3), after which the particles with the index corresponding to the layer deposited at this point were stripped off. The X-ray tomography images were also used to determine the height of the topography after the deposition of each layer. This height can then be used, for example, to impose a flattening condition on the top surface of the model.

4.3 Choosing the boundary conditions

In geomechanical restoration, specific boundary conditions have been used, such as flattening the top surface or tying the fault lines to remove fault throw (Muron 2005; Chauvin 2017). Because viscous behavior cannot be handled by elastic motion, the interface with basal salt layers were usually considered as free surfaces (e.g., Stockmeyer and Guzofski 2014). Here, we start with simple boundary conditions and show their impact on the motion inside the model and how they can be upgraded to more physical assumptions. The material properties of the layers are not studied here (they will be covered in section 4.4), so we consider them as constant in the simulations presented in this section (Table 4.4).

The density of the layers comes from the data (Table 4.1), and the density of the particles inside the faults is the same as in the rest of the layer they belong to. The

Table 4.3: Duration of the restoration simulation and topography height after deposition, for each layer of the analogue model. The number of the layer corresponds to the one given in Fig. 4.4.

Layer index	Simulation time (min)	Topography height (mm)	Layer type
1	18	52.6	sand
2	12	50.06	pyrex
3	16	48.26	sand
4	16	45.71	pyrex
5	16	44.68	sand
6	14	42.38	pyrex
7	14	40.09	sand
8	12	38.55	pyrex
9	10	37.27	sand
10	18	33.7	pyrex
11	14	31.14	sand
12	16	26.8	pyrex
13	14	22	sand
14	(pre-growth layers)	18	silicone

Table 4.4: Material properties of the silicone, sand and pyrex layers for the restoration simulations used in assessing the impact of different boundary conditions in the analogue model. In red, no specific density is used for the faults. The grey cells are the values that come from the data.

Material properties	Sand	Pyrex	Silicone SGM36	Fault core
Density	1.4	1.2	0.97	
Viscosity (Pa.s)	5.10^5	5.10^5	5.10^4	5.10^4

viscosity of the silicone is known, and we set the viscosity of the sand as ten times higher. The viscosity at the fault core is set to be the same as inside the silicone.

4.3.1 Restoration using kinematic boundary conditions

The first boundary conditions we tested were kinematic. The bottom and left boundaries were set to free slip. For each layer, the top surface was flattened using a Dirichlet condition: the vertical part of the velocity on the top nodes of the grid at time t was set to

$$v_y(n,t) = -\frac{Y_{final} - y(n)}{T_{simulation} - t}, \tag{4.1}$$

with n the index of the node, $y(n)$ its altitude, $T_{simulation}$ the duration of the restoration for the current top layer, and Y_{final} the height of the topography at the end of the restoration of the layer (determined from the tomography images and shown in Table 4.3). The applied velocity is in the opposite direction of the final altitude, as it is then applied with a backward advection scheme. The right boundary was set to a fixed flow. As we consider incompressible flow, the kinematic conditions must ensure the conservation of model volume during the simulation. This means that the volume

change due to the topography evolution ΔV_{top} must be compensated by the volume entering at the right boundary ΔV_{right}:

$$\Delta V_{top} = \Delta V_{right}. \tag{4.2}$$

Using the CFL condition, the time step is computed from the velocity field at each timestep. This is an issue here, because ΔV_{top} depends on the timestep (computed from the velocity field), and the velocity determining ΔV_{right} is necessary for the computation of the velocity field. To remove this dependency, we imposed a fixed time step Δt, in order to have a fixed volume change

$$\Delta V_{top} \simeq \frac{V_f - V_i}{T_{simulation}} \Delta t = \text{constant}. \tag{4.3}$$

The horizontal flow at the right boundary is then applied as

$$v_x(t) = \frac{\Delta V_{right}}{Y(t)\Delta t} = \frac{V_f - V_i}{Y(t) T_{simulation}}, \tag{4.4}$$

with $Y(t)$ the altitude of the upper right corner of the model.

The result at the end of the restoration of each layer is shown in Fig. 4.5. As imposed by the boundary conditions, the topography at the end of each layer restoration is flat, and the fault throw is reduced for all the faults. The restoration behaves well for the first layers, but has more difficulty restoring the oldest layers, which accumulated more deformation. For exemple, the sand and pyrex layers are expected to become increasingly flat during the restoration, but instead accumulate more folding. Likewise, the silicone diapirs tend to go upwards when they are expected to go downwards to flatten the sand/silicone interface. This is due to the model accumulating computation errors, as well as errors coming from the simplifications that were made (on the interfaces during the digitization of the model, on the material flowing from the right boundary and on the material properties inside the different layers for example). Another issue with the use of complete kinematic conditions is the resulting over-parameterization of the system, making it prone to over-steps in the velocity if the volume flow is not perfectly balanced. Since the time step is fixed, this can, for example, result in particles moving out of the model boundary in the advection step (because the CFL condition is not applied to avoid this phenomenon).

Overall, these first results are motivating, as they show the potential of the creeping flow restoration method when applying it to sedimentary basin analogues. One downfall of these results is that the boundary conditions are not natural, which makes it unclear if the resulting strain in the model is physical.

4.3.2 Upgrading the kinematic conditions to natural boundaries

In the previous section, the boundary conditions were not natural. Indeed, the right boundary was considered as having a constant flow, where the flow should in principle depend on the altitude. Moreover, the top surface was set to flattening where it corresponds to a free surface.

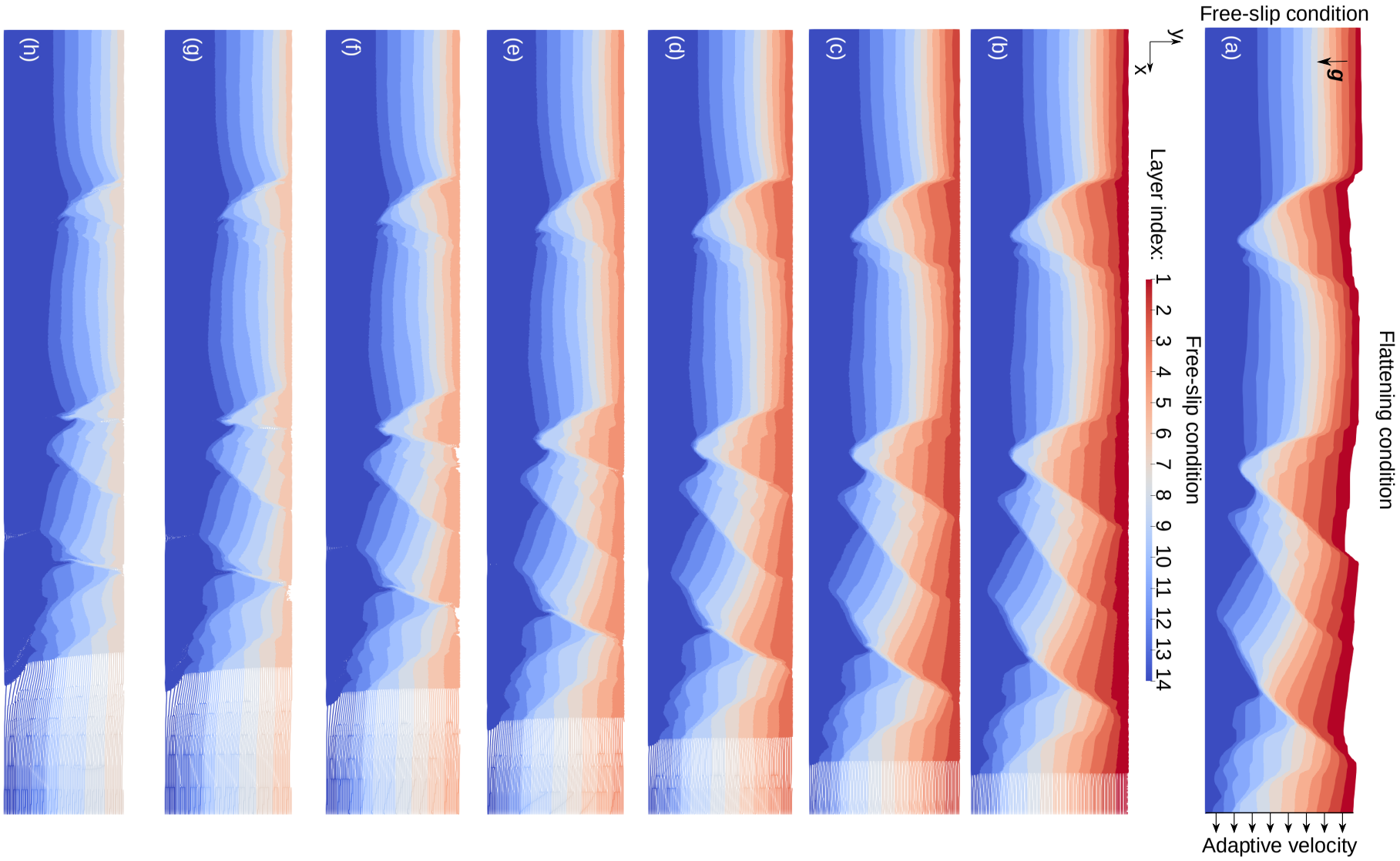

Figure 4.5: Results of the restoration of the successive layers of the analogue model. In this case, the bottom and left boundaries have a free-slip condition, the top is flattened to the topography height at layer deposition, and the right boundary has a velocity condition which adapts to the flattening condition, based on Eq. (4.4). (a) shows the setup at the beginning, and (b) to (h) show the state of the model at the end of the restoration of each layer.

- **Relaxing the right boundary condition**

In order to remove the over-parameterization of the model and add more natural boundary conditions, one can change the right boundary condition to a Neumann traction condition instead of a Dirichlet velocity condition. This lets the model evolve with more freedom relatively to the right boundary, as the velocity is then only imposed on the top surface. The question then arises, of the correct traction to impose at the right boundary. A first idea could be to consider the right boundary as a free surface, but it would neglect the weight of the rocks on the other side of the boundary. This leads to a subsiding of the right boundary, resulting in erroneous flow in restoration, as can be seen in Fig. 4.6.

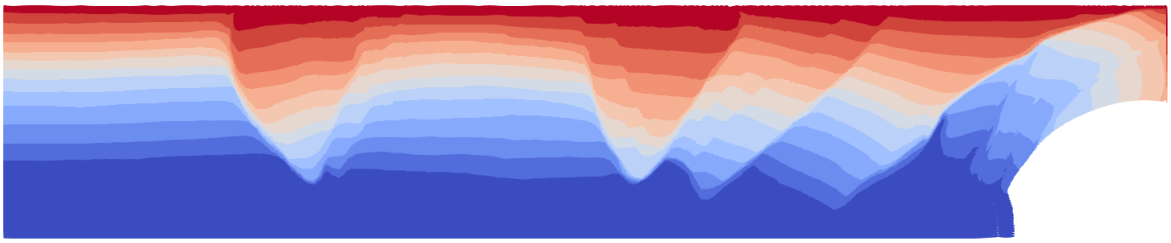

Figure 4.6: Result of the restoration of the first layer of the analogue model. In this case, the bottom and left boundaries have a free-slip condition, the top is flattened to the topography height at layer deposition, and the right boundary is considered as a free surface. It shows that considering the right boundary as a free surface ends in completely erroneous deformation close to it.

To upgrade the physical assumptions on this boundary, one has to account for the weight of the materials on the right side of the model, introducing a traction based on the pressure on the right boundary. As the pressure increases linearly with depth in a homogeneous media, first tests were done with a constant vertical gradient for the pressure and the resulting compression on the right boundary. Fig. 4.7 shows, however, that this over-simplifies the model, as the results of the velocity at the right boundary are very sensitive to the value of the pressure vertical gradient. To mitigate this, we can use a more accurate traction based on the lithostatic pressure $p(x, y)$ inside the model:

$$p(x, y) = p_0 + \int_y^{y_{max}(x)} \rho(x, y)||\overline{g}||ydy, \tag{4.5}$$

with p_0 the pressure at the surface of the model (neglected here). In the case of the analogue model, we consider a constant gravity vector $||\overline{g}||$ and the density as constant in each layer, which makes the lithostatic pressure piecewise linear (Fig. 4.8). As the model is tilted, the weight of materials above a given point is slightly shifted. Here, the model tilt angle is small ($\theta = 1.5°$), so its effect can be approximated to dividing the value given in Fig. 4.8 by $cos(\theta)$. The Neumann traction condition applied on the right boundary is then defined as:

$$\overline{h}_N(y) = -\nu * p(x_{max}, y) * \overline{n} \tag{4.6}$$

where the Poisson coefficient is taken as $\nu_{overburden} = 0.4$ in the sand and pyrex layers and $\nu_{silicone} = 0.5$ in the incompressible silicone layer, and $\overline{n}$ is the outward unit normal

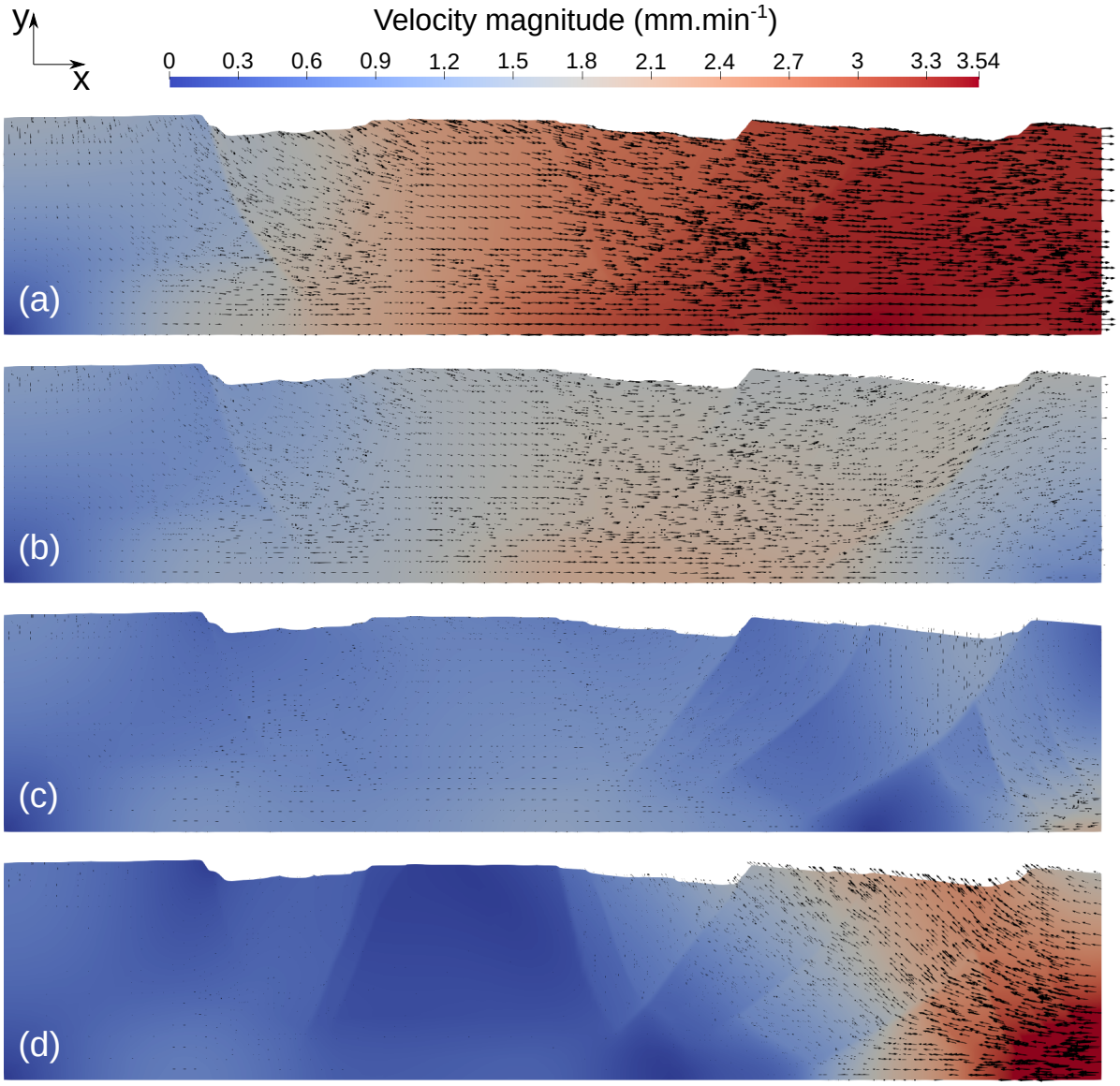

Figure 4.7: Velocity inside the analogue model, for different values of pressure vertical gradient at the right boundary. The bottom and left boundaries have a free-slip condition, the top is flattened to the topography height at layer deposition, and the right boundary has a traction which increases linearly with the depth. The pressure gradient between the top and the bottom is respectively 12 kg.mm^{-2}.s^{-2} for (a), 13 kg.mm^{-2}.s^{-2} for (b), 14 kg.mm^{-2}.s^{-2} for (c) and 15 kg.mm^{-2}.s^{-2} for (d). The black arrows show the velocity field in each test. We can see that even small variations at the right boundary have a big impact on the overall behavior of the material flow inside the model.

vector of the right border.

The results for the successive restoration of the layers with this traction are shown in Fig. 4.9.

- **Relaxing the top surface condition**

  In the previous simulations, the topography of the model was flattened for the

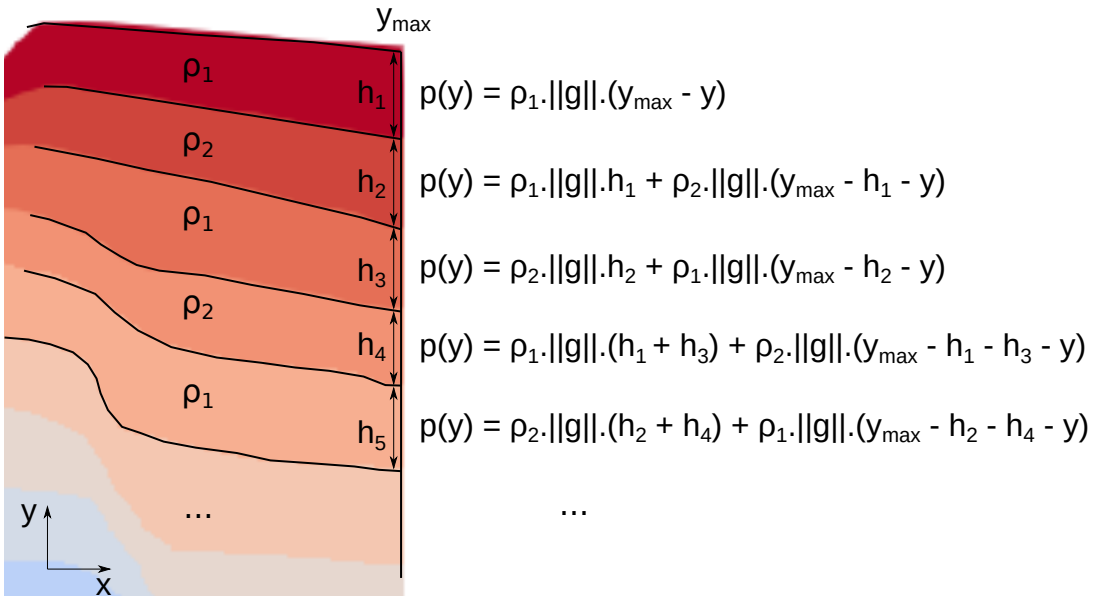

Figure 4.8: Computation of the lithostatic pressure at the right boundary of the analogue model. The value is then multiplied by a $cos(\theta)$ factor to take into account the impact of the model tilt on the boundary.

restoration of each layer. This condition was used to test if the model could be restored with creeping flow simulations and specific boundary conditions, and to test the impact of the right boundary condition. While it makes the top surface go back to the state it was in at deposition time, it is quite unphysical. Indeed, as the topography of the model is in contact with air during the analogue experiment, a free surface condition should be set on it. Moreover, the flattening imposes a Dirichlet condition, but the velocity of the topography through time is not known (and so it implies imposing a velocity which is assumed homogeneous). The enforcing of velocity conditions also makes it unsure if the rest of the model parameters are relevant, or if they just scale well with the imposed deformation. For example, Fig. 4.10 shows the top surface of the model after some time steps, with different conditions on the right boundary. We can see that the traction of Eq. (4.6) imposed on the right boundary is necessary to balance the model properly, or the topography ends up becoming steeper instead of coming closer to being flat. When the condition on the right boundary is set to a traction based on the lithostatic pressure, the fault throws of all the faults are reduced during the simulation, and the topography comes closer to being flat. While this is encouraging, the model still is not restored properly, as the model deformation is not consistent with the analogue experiment, where the velocity is lower. This is due to the material properties inside the model being incorrect, and particularly the sand and pyrex viscosities being too low.

4.4 Choosing the model parameters

In the previous section, I discussed the impact of the boundary conditions on the restoration of the analogue model. Here, I focus on finding relevant effective properties of the materials involved in the restoration.

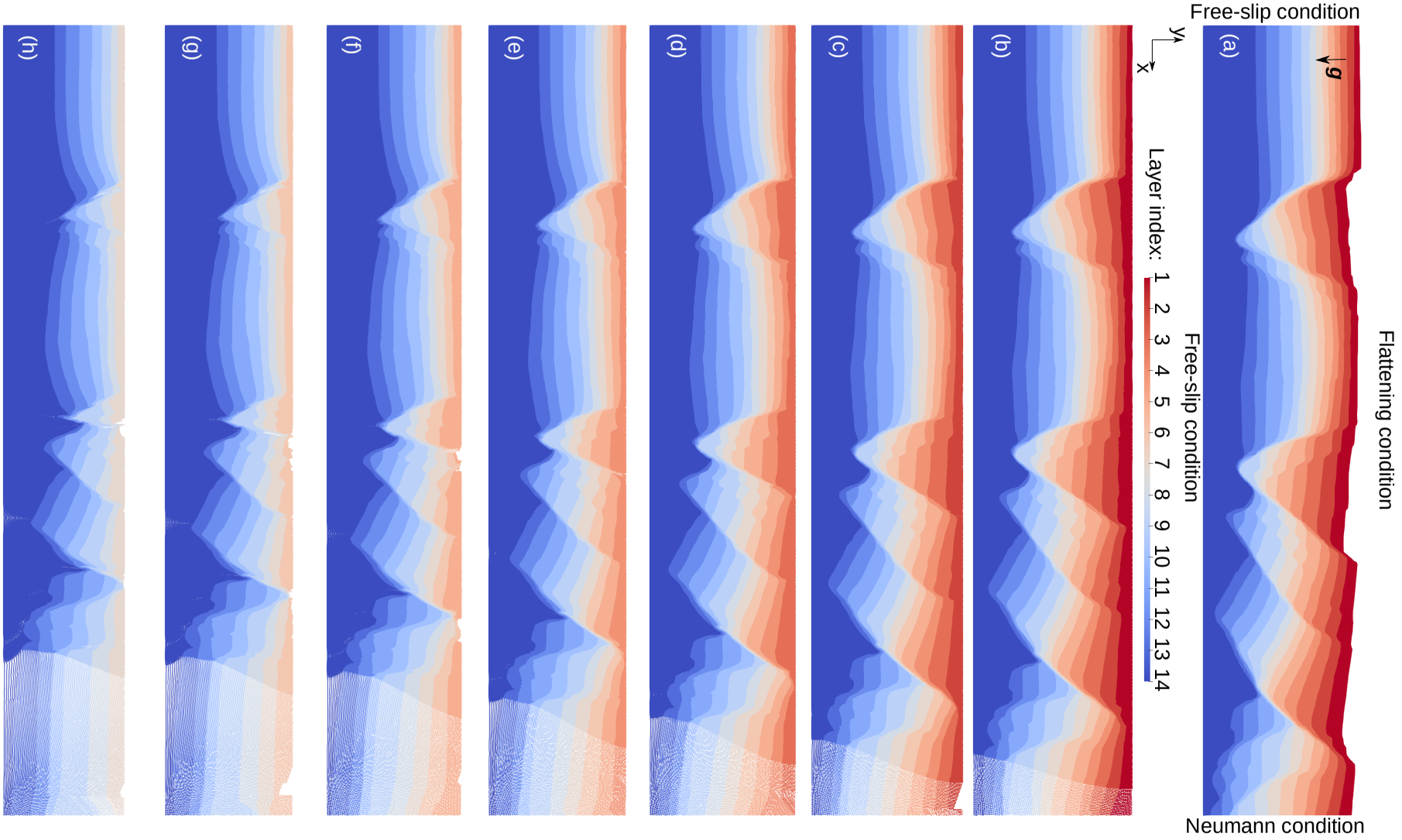

Figure 4.9: Results of the restoration of the successive layers of the analogue model. In this case, the bottom and left boundaries have a free-slip condition, the top is flattened to the topography height at layer deposition, and the right boundary uses the Neumann condition defined in Eq. (4.6).

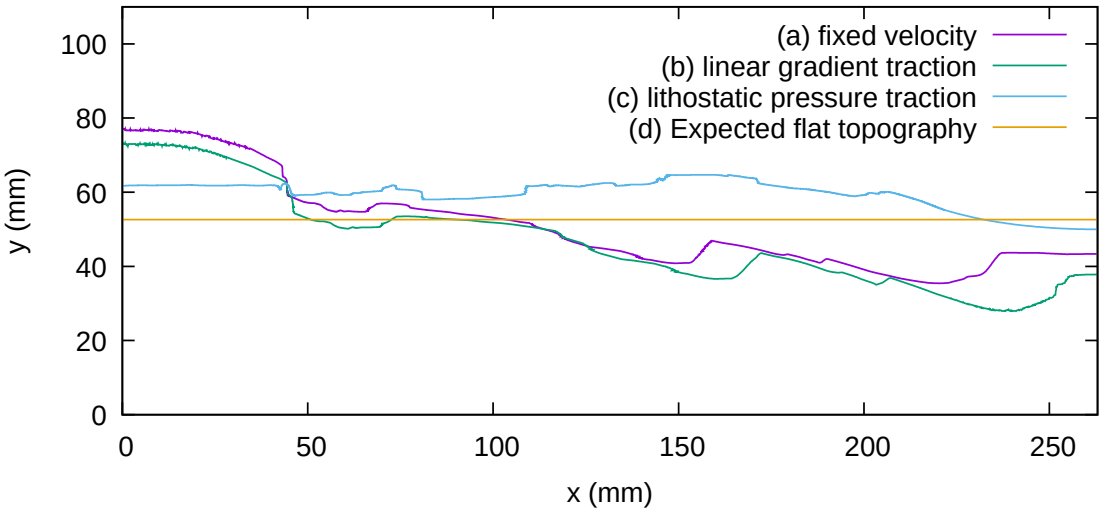

Figure 4.10: Comparison of the top surface of the analogue model, after a few hundred time steps of restoration. In those cases, the bottom and left boundaries have a free-slip condition and the top is a free surface. The right boundary is considered with a constant flow based on Eq. (4.4) in (a), a traction based on a constant pressure gradient in (b), and a piecewise linear traction based on the lithostatic pressure (Fig. 4.8) in (c). The expected flat topography is given in (d) as a reference. We can see that without the correct traction on the right boundary, the model deforms by bringing up the left part of the model and bringing down the right part of the model. On the contrary, with the traction based on the lithostatic pressure, the whole model is brought up and the fault throws are reduced. We can see, however, that the material properties inside the model do not restore it properly: the top surface ends up higher than expected.

The material properties that come from the data (shown in the grey cells of Table 4.4) were considered as known and do not change in this section. Based on the previous section, the boundary conditions were set as shown in Fig. 4.11. The left

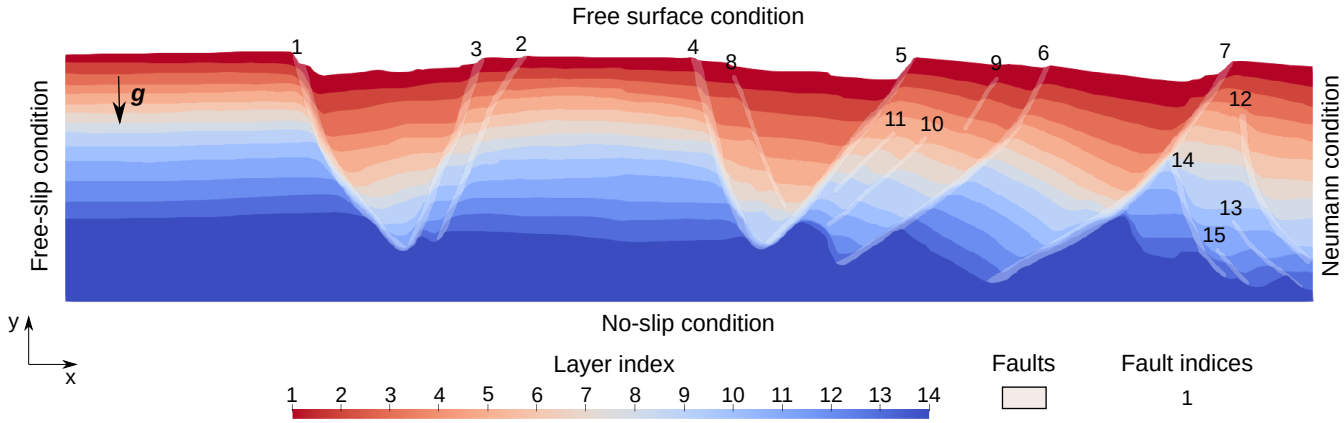

Figure 4.11: Setup of the analogue model to assess the impact of the material properties on the restoration simulations. The right boundary uses the Neumann condition defined in Eq. (4.6).

boundary had a free-slip condition, as the analogue experiment left side was cut in the tomography image used to create the model. The bottom boundary had a no-slip condi-

tion, since I considered it closer to the friction of the silicone against the bottom of the model (which hasn't been implemented) than a free-slip condition. The right boundary used the Neumann traction condition defined in Eq. (4.6). The top boundary condition was set to a free surface, to assess the impact of the choice of material properties on the simulation without enforcing the velocity on any boundary.

As most of the material properties were given as data, only the viscosity of the sand and pyrex layers were left as unknowns. For simplicity purposes, the viscosity was considered as constant in each layer (outside the faults), with the same value in all the layers no matter whether they are in sand or pyrex. In the faults, the applied viscosity is minimal at the fault core and increases with a power law to ten times its value at the contact with the rest of the layers. The range of the viscosity of the sand and pyrex (hereafter called "overburden viscosity") was chosen as $[10^5 : 10^7]$ Pa.s, in order to have a ratio of viscosity between the silicone and overburden in the range of $[2 : 2.10^2]$. The range of the fault viscosity was chosen as $[5.10^3 : \eta_{overburden}/2]$ Pa.s. Eight experiments were conducted, following the design of experiment shown in Fig. 4.12 for the viscosity of the overburden and faults.

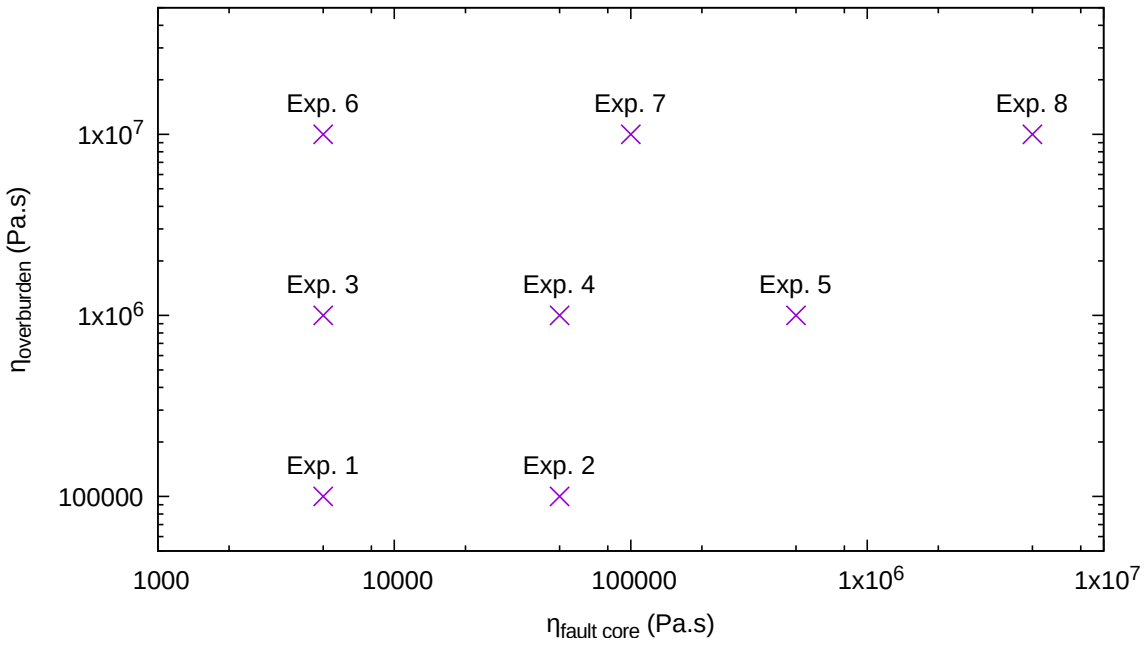

Figure 4.12: Design of experiments to roughly estimate the effective material properties of the analogue model.

To check the quality of the restoration for each experiment, various criteria can be applied. Here, given the difference in viscosity and the resulting velocity, I needed a criterion that can be tracked and compared throughout the simulation. The criterion I implemented corresponds to the area between the current topography of the model and the expected topography after the restoration of the first layer. It is computed as:

$$C_{expected\ horizontality}(t) = \int_0^{x_{max}} |y_{top}(x,t) - y_{expected}|\, dx, \tag{4.7}$$

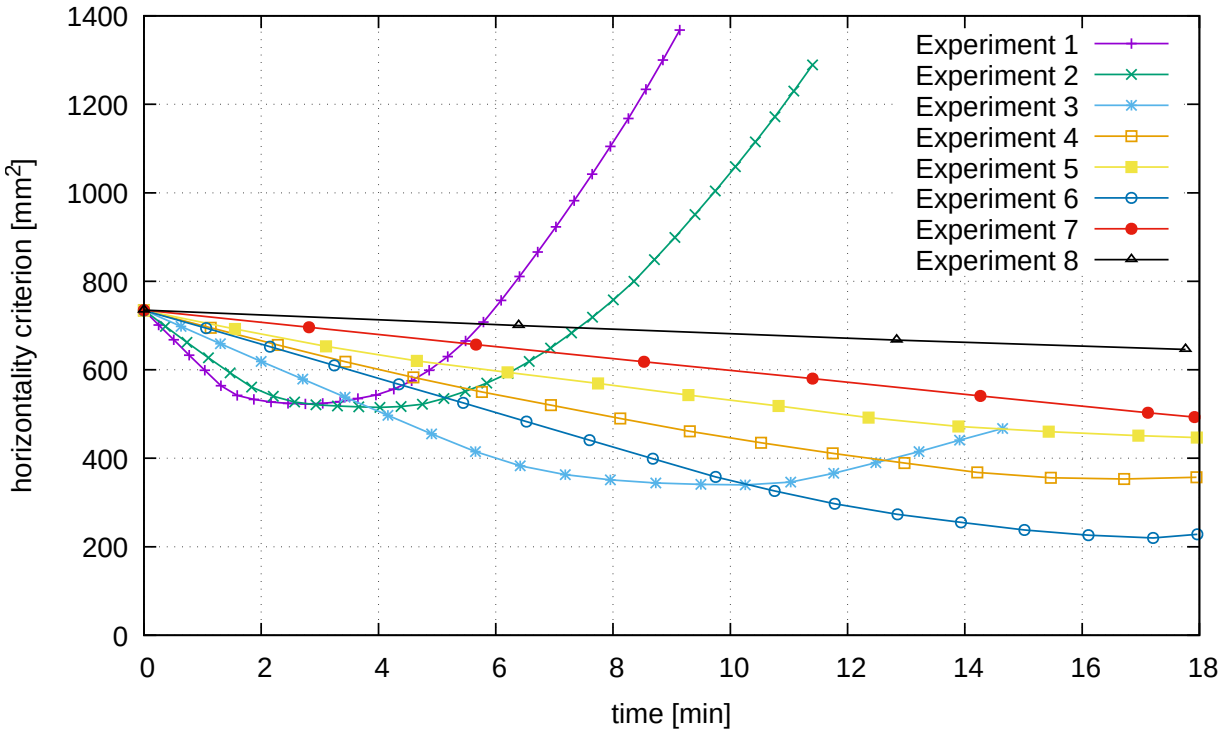

Figure 4.13: Values of the expected horizontality criterion (Eq. (4.7)) throughout time for the simulations of the design of experiments (Fig. 4.12) to find the effective material properties inside the analogue model.

where x_{max} is the domain length, $y_{top}(x)$ is the altitude of the topography along the x axis, and $y_{expected}$ is the expected altitude of the topography at the end of the restoration of the layer (from Table 4.3). This criterion is hereafter referred to as the expected horizontality criterion, and has several advantages: first, it is relatively simple to compute and track throughout the restoration simulations. Second, it gives a value of the global difference between the model and the expected restoration result with a flattened top layer. Third, it can be used to compare simulations which evolve at different velocities, and to check when they start to evolve in the wrong direction. As a downfall, the criterion is global, so it cannot be used to compare local differences between models, and it is only based on the topography, so it cannot be used to check the validity of the interior of the model during the restoration.

The values of the expected horizontality criterion through time for the eight experiments are given in Fig. 4.13. In all the experiments, we can see that the model deformation starts by going towards a flat topography at the expected altitude (the expected horizontality criterion decreases towards zero). In experiments 1 to 3, after some time this behavior changes and the model topography evolves away from the expected altitude. In the other experiments, the expected horizontality criterion decreases, but does not reach zero before the end of the layer restoration. In experiments 1 to 3, we let the simulations continue after the criterion started to increase, for test purposes. It could also be used, however, as a condition to spot when a restoration simulation is wrong (for example because of computational instabilities like those shown in Section 3.3.1) and stop the simulation.

While the expected horizontality criterion is good to determine the global distance between the simulations and the expected result, it is not enough to determine the 'best' material parameters for the restoration. Figures 4.14 and 4.15 show the state of the model for each experiment after the time t_{final} of their last point in Fig. 4.13, in order to analyze the impact of each parameter involved in the design of experiments in a more global and quantitative way.

In experiments 1 and 2, the rapid increase of the expected horizontality criterion is explained by the right part of the model going up. The overall restoration also shows that the thicknesses of the overburden layers increase too much, while the faults throws are not reduced much during the simulation. It can be explained by the viscosity of the overburden being too low compared to the viscosity of the faults. In experiment 3, we can see that the fault throws have overall been reduced, but some fault throws have been inverted (on faults 2, 6 and 7, with the numbering of Fig. 4.4), suggesting that the viscosity of these faults is too low. In experiment 4, as in experiments 1 and 2, the deformation of the left and right parts of the model is too important, while the fault throws are not reduced much, showing that the viscosity of the faults is not low enough, while the viscosity of the overburden is too low. In experiment 6, the faults throws have overall been reduced or canceled. Although it shows the best results in the design of experiments, like in experiment 3, faults 2, 6 and 7 (with the numbering of Fig. 4.4) have started to invert their fault throw, showing that their viscosity is too low compared to the viscosity of the overburden. On most faults, a new phenomenon also appears: the particles inside the shear zones move to a higher altitude than those of the layers around them. It could suggest that the effective density inside the faults is lower than in the rest of the overburden. Another specificity of this experiment is the very high local viscosity difference between the faults and the overburden (ratio of about 2.10^3 between the two): while simulations can still be run in the model, and show the most promising results, it highly increases the computation time compared to the other experiments (about ten times as long as experiment 7). In experiments 7 and 8, the overall deformation is too small, showing that the viscosity of both the overburden and faults is too high.

Given the results on the design of experiment, the 'best' effective properties should be a viscosity between 10^6 Pa.s and 10^7 Pa.s (but closer to 10^7 Pa.s) for the sand and pyrex layers, and a viscosity between 10^3 Pa.s and 5.10^4 Pa.s (but closer to 10^3 Pa.s) for the core of the faults. The viscosity in the faults numbered 2, 6 and 7 in Fig. 4.4 should also be higher than in the rest of the faults. More tests will have to be done, however, as we can see that the results are intricately linked to both the viscosity of the sand and pyrex layers and the viscosity applied in the faults, and these two parameters must be determined at the same time.

4.5 Discussion on the analogue model results

In the previous chapter, we showed that creeping flow restoration can be applied to geological models which include faults and in which the top surface is considered with a free surface condition. A first assessment of the impact of material properties was also done, but using overly simplifying assumptions on the model setup and its boundary

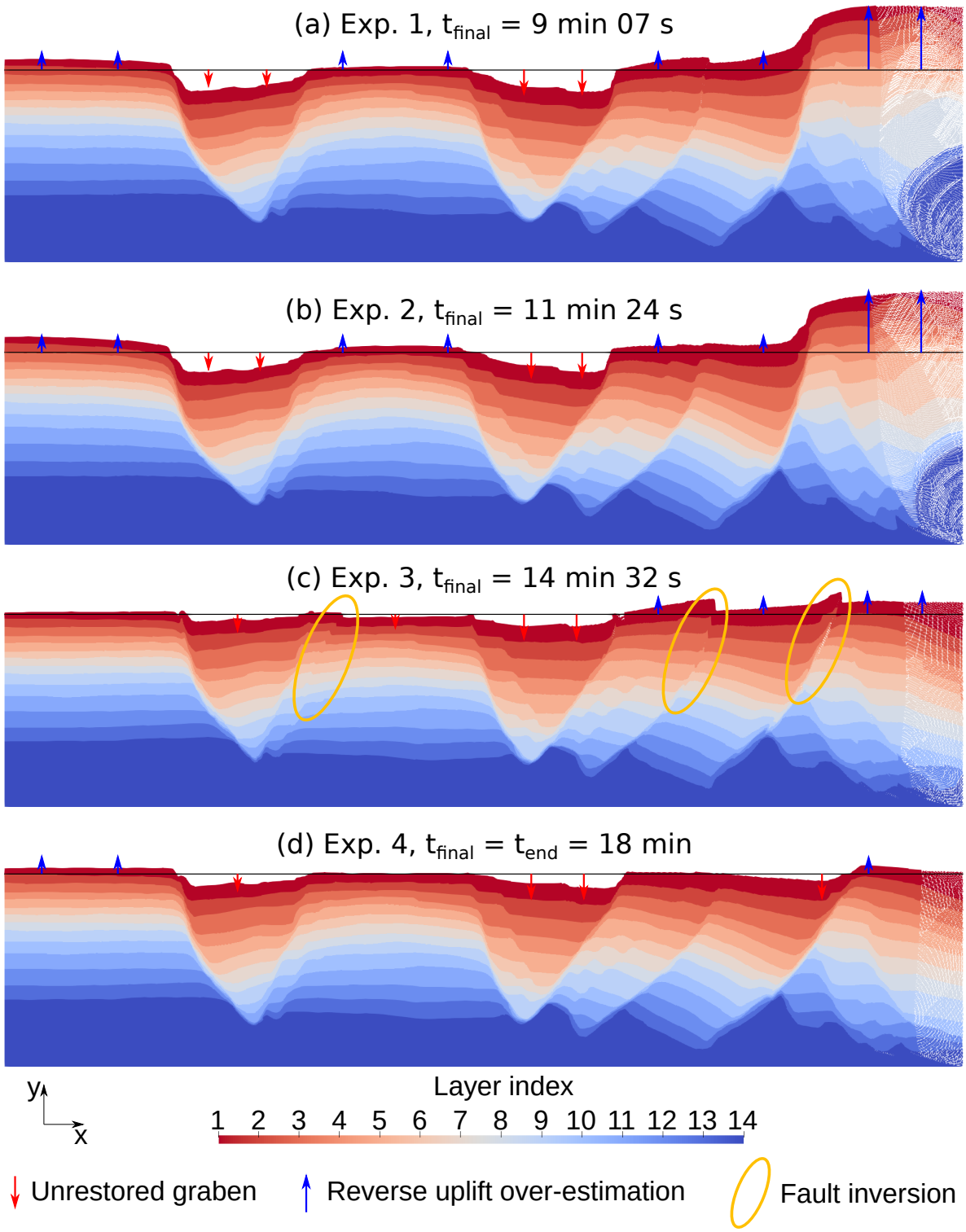

Figure 4.14: Results for the simulations of experiments 1 to 4 in the design of experiments (Fig. 4.12), to find the effective material properties inside the analogue model. For each experiment, t_{final} is the restoration time after which the simulation is stopped, and for which the model is shown. t_{end} is the time at the end of the restoration of the first layer. The black line on each result is the expected position of the topography at the end of the restoration of the first layer.

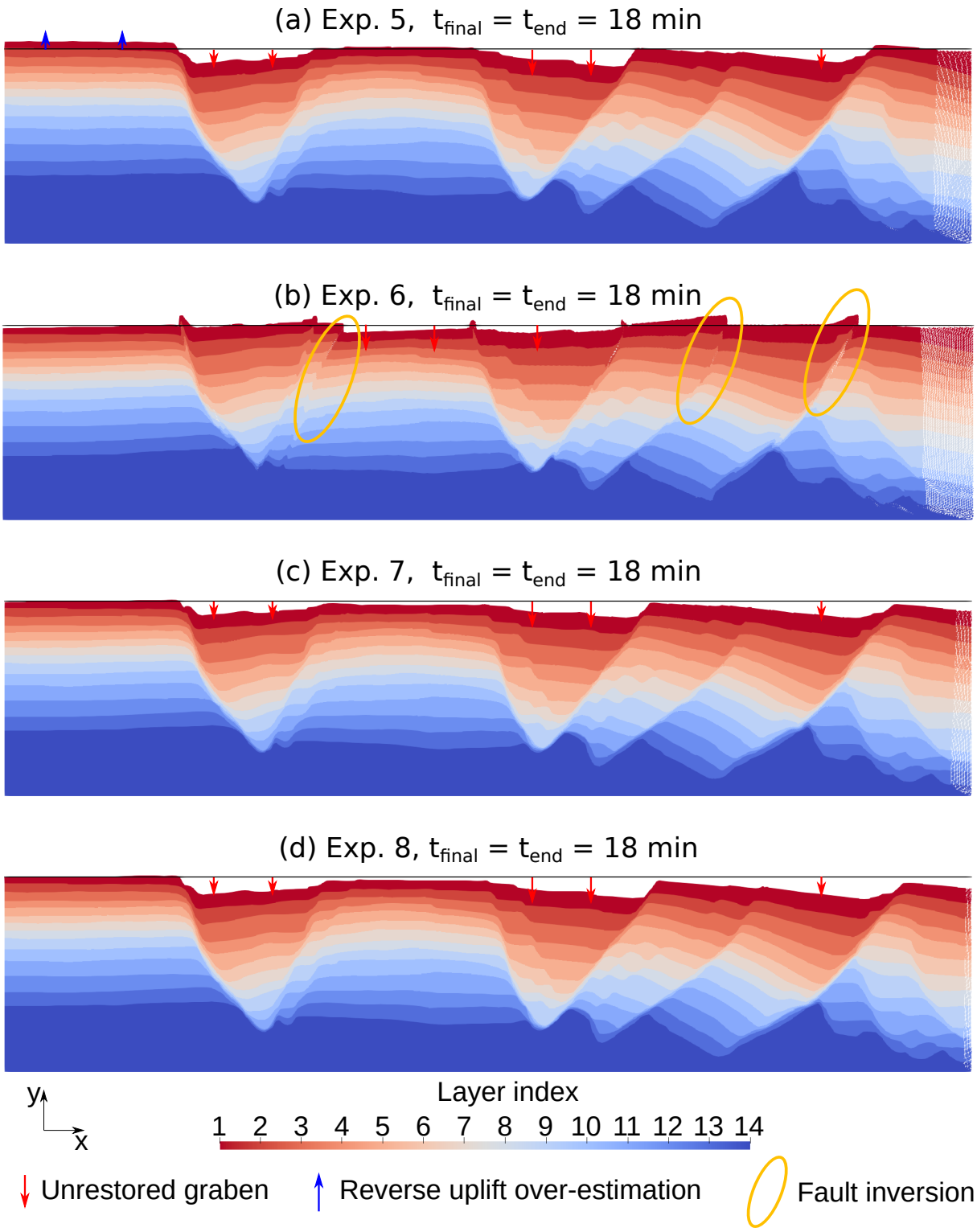

Figure 4.15: Results for the simulations of experiments 5 to 8 in the design of experiments (Fig. 4.12), to find the effective material properties inside the analogue model. For each experiment, t_{final} is the restoration time after which the simulation is stopped, and for which the model is shown. t_{end} is the time at the end of the restoration of the first layer. The black line on each result is the expected position of the topography at the end of the restoration of the first layer.

conditions. Here, using an analogue experiment model had three main advantages. First, it showed the results of the creeping flow restoration method on a model where the initial state for the restoration was not obtained synthetically with a forward simulation, but by the deformation of an actual material. Second, the previous states in the history of the model were known, so the results of the restoration could still be compared to them to assess the validity of the method. Third, various parameters were set for the laboratory experiment, which simplified considerably the field of parameters for which the values are not known, and which need testing.

- **Boundary conditions**

The first tests on the analogue experiment model showed that the first layers of the model could be restored properly with kinematic boundary conditions such as those used in standard geomechanical restoration. In order to add more physics in the process, as was the intention with creeping flow restoration, other more 'natural' boundary conditions and their impact were then studied. It showed first that to use a Neumann traction condition on the right boundary, the distribution of the lithostatic pressure has to be accounted for. It also showed that using a free surface condition on the topography is not only more physical, but can serve to detect when the model parameters make it unbalanced (because of the other boundary conditions, or because of the material properties for example). Several simplifications have been done, however, leaving some considerations out of the testing range.

The case of the left and bottom boundaries has not been discussed much, for example. Here, the first tests used a free-slip condition on both surfaces, and the simulations on the design of experiments changed the bottom boundary to a no-slip condition. These assumptions are simplifications, and a friction condition on the bottom and a Neumann condition on the left side may have been more physical. Several tests showed, however, that the difference between a free-slip and no-slip condition on the two boundaries really impacted the simulations only if they were otherwise unbalanced (by a wrong traction on the right boundary, for example).

For the right boundary traction, the Poisson coefficient was set from reference values for the type of materials in the model, but its value may have to be estimated more properly and more precisely. In Appendix 4.A, we show that while the Poisson coefficient value does not impact the general behavior of the model in the design of experiment, it impacts the value of the 'best' effective viscosity inside the model. Another possible issue with the traction at the right boundary of the model is the account of the tilt and its implications on the material on the other side of the boundary. Here, I did not consider the impact of the movement of this material, as the Stokes equations ignore the inertia of the model. It poses, however, the following question: does the movement of surrounding materials impact the horizontal pressure applied by them on the boundaries of the model ? In which case, the traction would have to be changed accordingly.

- **Material properties**

The tests done on the boundary conditions of the analogue experiment model also showed that the material properties used at this point did not allow the restoration of the model. To study their impact and to find the 'best' effective properties inside

the model, a design of experiment was used, and the restoration scheme was applied to eight models with different properties. As the values of the other material parameters were known, the parameters that were studied were the viscosity inside the faults and the viscosity in the sand and pyrex layers. While these parameters have a large impact on the restoration, the results help narrow down their effective value, as well as point out some issues with the simulations.

In the different restoration simulations done on the analogue model, the shear band thickness changed depending on the fault, but the viscosity at their core was considered as being the same in all the faults and the same through time. The results, however, showed that this assumption simplifies the model too much. Indeed, while the fault throws were reduced overall, the model deformation was either not large enough on all faults, or not large enough on some faults and too large on others. This resulted in some fault throws inverting while other faults were not yet restored, in two of the experiments. To properly restore the analogue model, a more physical management of the faults is needed, where a different effective viscosity is used for each fault. Several factors could be studied to guide the choice of this variable viscosity, such as the age of the fault or the thickness of the shear band. A local criterion to measure the fault throw for each fault may then be necessary to study this phenomenon further.

In order to add yet more physics, other simplifications could also be lifted, but would need tests to assess the impact of their removal. For example, here the viscosity was considered as independent from time and from the layering of the model. It could be interesting, however, to study the influence of accumulated strain (by considering the sand and pyrex layers as visco-elastic materials), or of a variable viscosity in the layers (depending on the type of layer, or on the age and altitude, for example). Other than viscosity, the density could also be studied more. Here, the values that were used came from the data available on the analogue experiment. The documentation, however, mentions a bulk density variation of up to 30% inside the faults of the analogue model. Using such a density variation may provide more physical results for the restoration, and avoid uplifts of the shear band particles such as those seen in experiment 6. The impact of this change on the velocity field inside the shear bands would then have to be assessed as well.

- **Scaling to real-size geological models**

While analogue experiments simplify the deformation of rocks at geological time and space scales, they are useful tools to understand the deformation history of various areas. In the case of restoration, their construction brings additional advantages that can be used. First, a large amount of data is available on the model, including its state at various times in its history. It can be used, as we have done here, to ascertain the quality and uncertainties linked to a specific restoration method. Second, their deformation is analogue to the deformation that can happen in areas of geological interest. It means that finding the effective material parameters inside an analogue model brings us closer to determining the effective material parameters inside these areas of geological interest. The advantage here lies in the controlled environment in which the analogue experiment is run, which implies in turn that the effective material parameters inside it are easier to determine. It also allows various tests on the impact of other parameters, as we have

done here with the boundary conditions for example.

- **Conclusion**

This chapter showed the results obtained with the creeping flow restoration method on a complex structural model including various faults. The first results start with fully kinematic boundary conditions, then show that they can be relaxed to more physical ones. Conclusive results were obtained here with only the flattening of the top surface as a kinematic drive of the restoration (change side velocity and fault throw removal conditions to more physical ones compared to previous geomechanical methods). The consideration of the topography with a free surface condition was shown to be difficult, but the results obtained by the simulations on a design of experiments are promising. They show that tuning the effective material properties inside the domain should allow the simulations to go towards the state expected after the restoration of the model layers. More tests, however, are needed, as the method has not yet been able to restore the analogue model to a state with a fully flattened topography.

Appendix

4.A Impact of the Poisson coefficient

In order to test the impact of the traction on the right boundary, other tests were done with a different Poisson coefficient for the application of this traction. Figure 4.A.1 shows the horizontality criterion through time for the simulations on the design of experiment used in Section 4.4, with a Poisson coefficient of $\nu = -1$. Figure 4.A.2

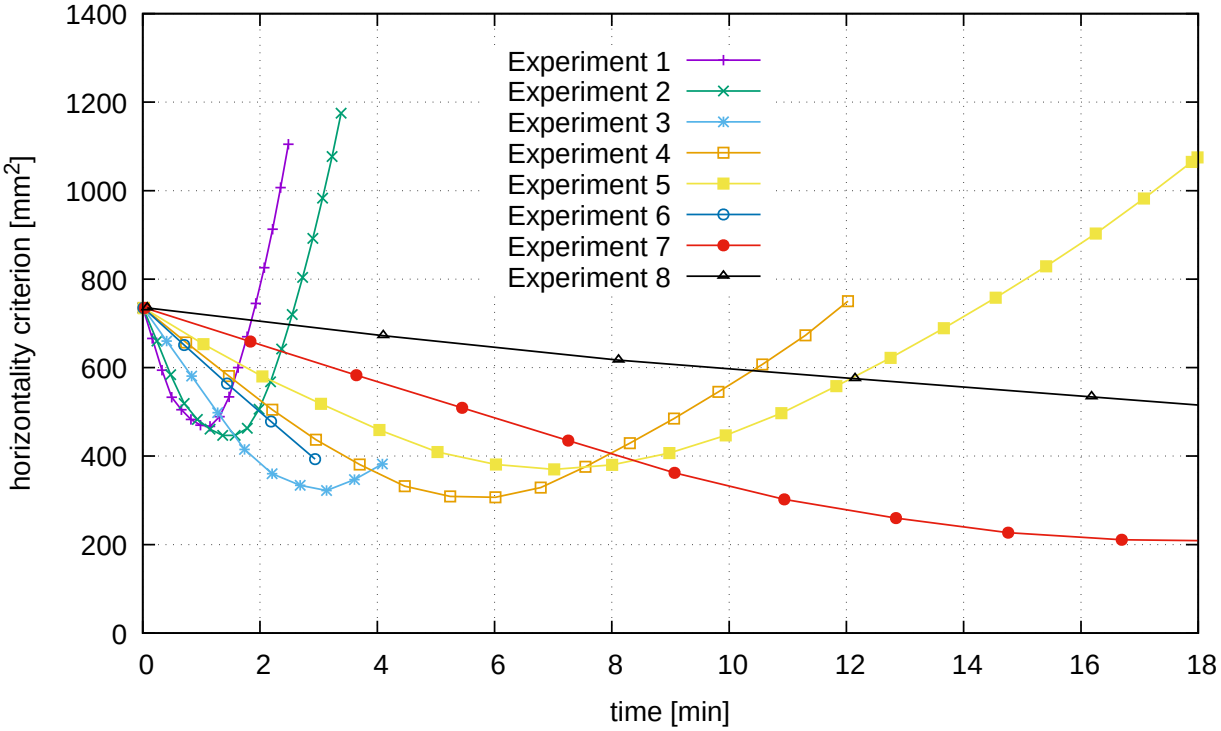

Figure 4.A.1: Values of the expected horizontality criterion throughout time for the simulations of the design of experiments (Fig. 4.12) with a Neumann traction on the right boundary using a Poisson coefficient of $\nu = -1$. Although this Poisson coefficient is highly unlikely, the model behavior is similar, but the 'best' material properties for its restoration are not the same.

shows the same curves for a Poisson coefficient of $\nu = 0.75$.

While those values for the Poisson coefficient are very unlikely, or even unphysical, they show that the trend of the results on the design of experiment does not change much. What changes is the impact of the viscosity inside the model: given how much traction is applied on the right boundary, if it is well distributed, the model deformation

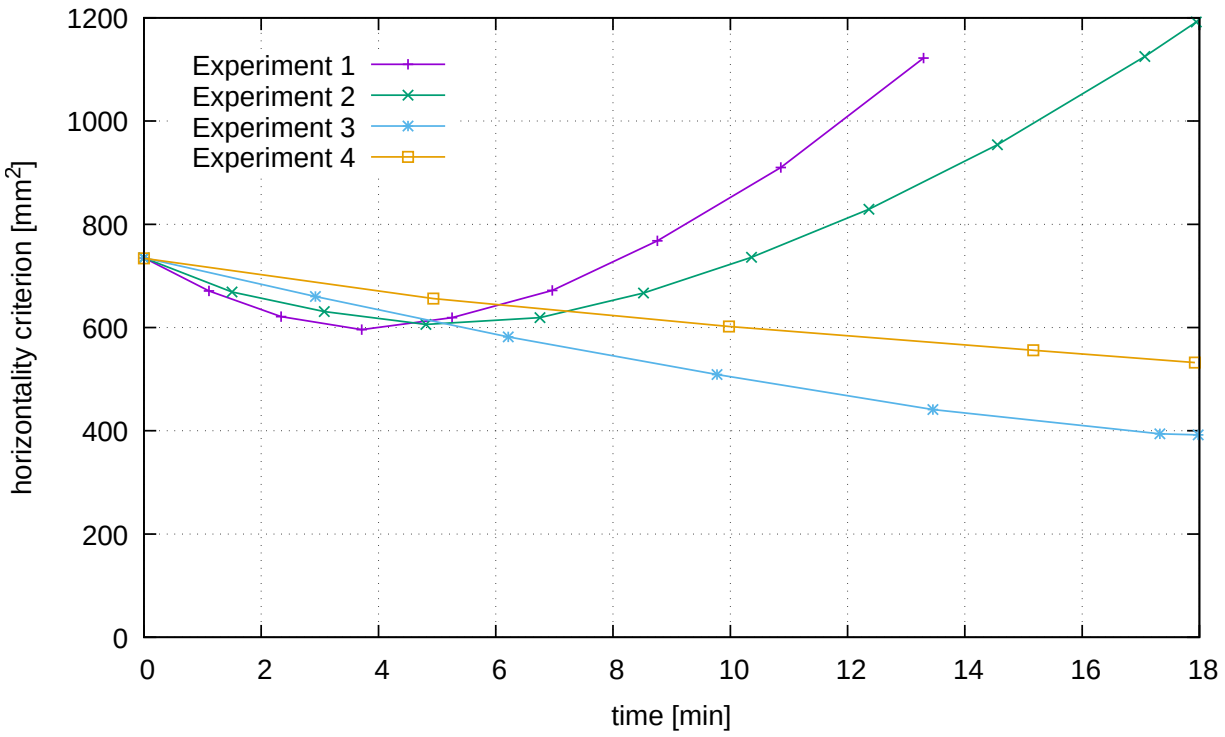

Figure 4.A.2: Values of the expected horizontality criterion throughout time for the simulations of the design of experiments (Fig. 4.12) with a Neumann traction on the right boundary using a Poisson coefficient of $\nu = 0.75$. Although this Poisson coefficient is unphysical, the model behavior is similar, but the 'best' material properties for its restoration are not the same. Because of the high Poisson coefficient, the model evolution is very slow, and the horizontality criterion in experiments 5 to 8 hardly changes, so it was not ploted here.

will only be faster or slower. As an effect, the restoration will still be possible, but with a different effective viscosity for the faults and the overburden.

General conclusions

Structural restoration methods first used kinematic or geometric rules to unfold and unfault geological models. In order to add more physics to the process, geomechanical restoration was developed as a mechanical simulation to compute the deformation inside the models. The method, however, considers elastic behavior despite the large deformations in the models, and uses mainly kinematic or geometric rules to drive the simulation. In a parallel field, creeping flow restoration was developed for models including salt structures, where geometric and kinematic restoration failed. The method, however, was only applied to models without faults and with a topography that was either flat or flattened by the erosion and deposition of sediments at each time step. The aim of my thesis was to add more physics to geomechanical restoration, by applying creeping flow restoration to structural models including faults and having a non-flat topography. In the following, I summarize the main contributions and results of my work, and point out the research perspectives that are most promising to me.

Main contributions

The use of creeping flow restoration was studied to remove kinematic conditions such as imposing the deformation on the faults and on the topography, and replace them with more physical assumptions. It is based on solving the Stokes equations to compute the velocity field inside a model, and then apply it with a backward advection scheme. A proof of concept was first done on synthetic models, and an analogue experiment model was then used to study the impact of the boundary conditions and effective material properties on the restoration simulations.

Application of the creeping flow restoration method

Numerical method

The first contribution of this thesis is the development of FAIStokes, a numerical solution to apply the creeping flow restoration method. While the concepts used in this software are not new, it showed that creeping flow restoration can be achieved with a method using particles and adaptive grid refinement. The method is well adapted: first, the absence of connectivity between the particles means they can move freely in the domain, allowing very large deformations with no need for meshing or remeshing the material model. Second, the adaptive refinement of the computation grid allows it to capture the small scale heterogeneities of the models, and achieve valuable precision while still having tractable computation time. Another advantage worth mentioning, although it

hasn't been used here, is the possibility to divide the particle swarm along with the computational grid. Blocks of cells and the particles they contain can then be used to parallelize the computation of the velocity field.

Applying the method to various structural models also showed its downfalls. First, the particle swarm needs to be large enough to provide a precise interpolation of the properties on the computation grid (usually at least a few hundred thousands of particles). In models where high precision is needed, it can mean very large swarms, introducing a proportional memory consumption. It also means that specific implementations to store or find easily the neighboring particles of a cell are necessary, increasing the memory consumption some more. Second, the topography is followed by the nodes at the top of the computational grid, which deforms the cells. In the case of a steep local topography, it means that the cells can be highly distorted, and that the grid may need to be refined under this steep change to retain its validity.

Proof of concept

The second contribution of this thesis is the proof of concept of the application of the creeping flow restoration method to structural models including faults and a non-flat topography. The method was first tested on synthetic models with simple boundary conditions, where it proved its potential for the restoration of models including salt (which can't be modeled with the elastic deformation of usual geomechanical restoration methods). A free surface condition on the topography was then added in the synthetic models. This condition, while more physical, brought instability issues when applying the backward advection scheme. I showed that these instabilities can be relaxed by introducing yet more physical assumptions in the simulation. This was done with the addition, first of faults modeled by a low viscosity shear band, and second, of lateral flow to simulate horizontal extension, which has been acknowledged to play a key role in salt tectonics (e.g., Brun and Fort 2011).

While the results were conclusive, it also showed that more tests would be needed, especially on non-synthetic models, where the input for the restoration does not come from a forward simulation.

Impact of the restoration parameters

The third contribution of this thesis is the application of the creeping flow restoration method to an analogue experiment model. The advantage, compared to previous models, is that the input model for the restoration comes from the deformation of real materials, but the deformation history is still known (and can be compared to simulation results). For simplification purposes and to keep as much raw data as possible (without having to scale it), the restoration simulation experiments were done on the model at the experiment size. The creeping flow restoration was first applied to this model with kinematic boundary conditions. In this test, only the consideration of the faults as shear bands of lower effective viscosity was more physical, compared to usual geomechanical restoration schemes. In these conditions, the model was well restored, which allowed to go further and do a sensitivity study on the different parameters of the restoration that did not come from the data. This study aimed first at finding more physical boundary

conditions, which it did for the two boundaries with the least-physical conditions. It then focused on finding the effective material properties inside the model, and showed that it was possible to narrow down their range of possible values.

Impact of the boundary conditions

In the analogue experiment model, the least physical boundary conditions used in the first test were the top and right boundaries, where the velocity was enforced to flatten the topography. The right boundary was first studied, as its kinematic description depended on the top surface condition. Neumann conditions were considered to relax the constant lateral flow condition. Different tests showed that the best results are obtained when using the 'natural' traction implied by the horizontal report of the lithostatic pressure. The flattening applied on the topography was then adressed, as the previous simulations in this analogue experiment model were mainly driven by this condition. This surface is in contact with air during the simulation, so the most natural way to consider it is with a free surface condition. Using this condition, the model deformation is driven only by its weight. This allowed to verify that a Neumann traction based on the horizontal report of the lithostatic pressure is necessary to balance the model properly. It also showed that the effective properties that had been used up to this point did not allow for flattening the topography in spite of the more physical boundary conditions. In particular, the viscosity set in the sand and pyrex layers of the analogue experiment model was too low, leading to deformation inconsistent with the previous states of the model available in the data.

This analysis showed that creeping flow restoration can be used with more natural boundary conditions than just kinematic ones. When using fully natural boundary conditions, the model deformation can easily be inconsistent if the effective properties are not right. This is both a downfall and an advantage: on the one hand, it can be considered as an issue because restoration then needs a precise account of unknown parameters to work with natural boundary conditions. On the other hand, it is an advantage because valuable information can then be obtained for unknown data in the model through sensitivity tests on the restoration.

Impact of the material properties

The boundary conditions assessed as the most physical ones (free surface condition on the topography, and Neumann traction based on the horizontal report of the lithostatic pressure on the right boundary) proved to be unable to restore the model without the right material properties inside the model. This was used to assess the 'best' material properties inside the model: if the restored model is closer to the previous states shown in the data, the properties are closer to the effective ones. As most parameters are given as data for the analogue experiment model, the unknown parameters were the effective viscosity in the brittle sand and pyrex layers and in the faults. A design of experiment was then set to test different values for these parameters. For a first analysis of the results, a criterion based on the distance to the altitude expected of the topography at the end of the restoration of each layer was used.

The results show that the material properties have a large impact on the restoration, and that the field in which to choose them can be narrowed down by such experiments.

Here, it also pointed out that some of the modeling assumptions oversimplified the model. For example, the comparison of fault throws in the different simulations showed that a different or time-varying viscosity has to be used inside each fault.

While this study only provides a rough idea of the material properties in the analogue experiment model, it can be used as a basis for more tests, and for finding a more precise range of values for these properties. The results can also be generalized: scaling the properties obtained with this method could also give an idea of those that should be used in models of the subsurface having an analogue deformation at geological timescales.

Perspectives

Several perspectives can be considered to continue this work. To show what they can each bring, I will divide them in two types here: developments of the numerical method, and new applications and tests of the method.

Upgrading the numerical method

The first perspective is a purely numerical consideration: code efficiency and CPU speed upgrades can only speed up the computations to a point, and to provide faster results for numerical simulations such as those presented here, the FAIStokes code must be parallelized, at least for the part of solving the Stokes equations on the FEM grid (Gassmöller et al. 2018). For lack of time, it was not done, but it may need to be the first step to do more tests with this code. Indeed, some of the restoration results shown on the synthetic and analogue experiment models took up to a week to achieve. While efficiency was not the aim of this thesis, to have tractable computation time for tests on a larger scale, and to even think about applying the method to 3D models, I believe upgrading the code on this point is the first step.

The method can also be upgraded on other less numerical notes, by adding more criteria for the analysis of the results obtained by the restoration simulations. In the synthetic models, the distance between the position of the particles at the beginning of the forward simulation and at the end of the restoration could be used, but in non-synthetic models this isn't possible. In the analogue experiment restoration, I showed a criterion based on the difference from the expected position after the restoration, which worked quite well, but a visual analysis of the results was still needed to truly understand them. In order to further analyze the restoration results, other global and local criteria would need to be implemented. Those I find the most relevant are: first, the computation of the fault throw, for example by using the position of the interfaces on each side of the faults. It could provide valuable information on how well each fault is restored, and guide the choice on their effective viscosity. Second, for the analogue model, the previous states in the history of the model were only used visually. Their numerization, however, would allow the numerical comparison of the position of the interfaces after the restoration and their real position in the history of the model. Third, computing the strain inside the model may allow further analysis of the results. Finally, the expected horizontality criterion could be generalized to measure global folding decrease. This list, however, is not exhaustive, and other models may need other criteria to analyze the results.

On another note, the interpolation methods to transfer information between the computation grid and the particle swarm containing the material properties were not discussed much here. It could be interesting, however, to work on different schemes for both the interpolation of the material properties on the computational grid and the interpolation of the velocity on the particle swarm. Some form of homogenization technique to find the effective local parameters, for example, may relax the high viscosity differences present in the models (e.g., Cupillard* and Botella 2015). This could, in turn, relax the strain put on the FE solver, and lead to smaller computation times.

Application of the method

The analogue experiment model was used for a first assessment of the impact of the boundary conditions and effective material properties on the restoration simulations. It allowed to narrow down the range of values for the effective parameters, and to detect some of the assumptions that over-simplified the model behavior. While the least-known parameters were tested, several others that may have an impact on the restoration can be considered in future tests.

First of all, the modeling of faults as shear bands of lower viscosity is quite new in restoration (to the best of my knowledge). Consequently, it still needs to be tested some more, and would benefit from taking into account previous works on the forward modeling of shear zones (e.g., Daudré and Cloetingh 1994; Kaus 2010; Duretz et al. 2019), to upgrade it on several points. For example, the distribution of viscosity inside the shear zone, between the fault core and the surrounding material, was chosen quite arbitrarily. More bibliography (e.g., Walton and Braun 1986) and a sensitivity study with different distributions might help improve this point. The results on the analogue experiment model also showed that a different viscosity has to be considered for each fault core to properly restore the model. In order to generalize this result, it could be interesting to test if the effective viscosity in the fault can be treated as a function of another parameter, such as the age or the size of the fault. One might also wonder, and then test, the effects of changing the viscosity inside the faults depending on the altitude, or on the time of the simulation (to account for fault softening for example). A last point that may need to be explored for the faults, is their density. In the simulations that have been run on the analogue experiment model, the density of the particles depended only on the layer in which they were, and not their position in a fault. The documentation (IFP and Reservoirs 2006), however, states a bulk density variation up to 30% in the faults, which may explain some of the results obtained and needs to be taken into account.

In the experiments that were led in the analogue experiment model, the viscosity is considered, for each experiment, as constant and the same in the sand and pyrex layers that form the stratigraphy growth. It could be interesting to challenge this assumption by testing the impact of a different viscosity in the sand layers than in the pyrex layers, or of a viscosity depending on the altitude, for example.

The model that was used in the last chapter was created from a 2D cross-section at the border of an analogue experiment. A last perspective on the application of the method to this experiment would be to take a cross-section at the middle of the experiment, or to construct a 3D particle swarm of the analogue experiment result and

apply the creeping flow restoration method to it. It would give valuable information on the ability of the method to handle out-of-plane deformation and restore 3D structural models.

Finally, it would be interesting to apply the creeping flow restoration method to other structural models.

The use of other analogue experiment setups, first, would allow to check to validity of the conditions that were found on this one. It would also provide the effective properties in a wider range of model deformation types. The comparison of the effective viscosity in different analogue models, for example, could provide interesting data when scaling the effective properties to apply the method on models of the subsurface at geological timescales.

While adding more physical conditions to geomechanical restoration is interesting in itself, the goal is also to provide a working method for the restoration of models describing the subsurface in real cases. The effective properties in these models could be determined from scaling the results obtained on analogue models, but other questions would also arise. For example, the boundary conditions may be more complicated, with the addition of continuous erosion and sedimentation on the topography (compared to punctual sedimentation in the analogue experiment). The forces at play several kilometers underground are also unknown, and the bottom boundary may prove to be more challenging than the free-slip and no-slip conditions applied here. For example, specific flow due to uplift or subsidence of the layers below the model may need to be taken into account. The pressure applied on the lateral boundaries may also prove to be more challenging than a Neumann traction based on the horizontal report of the lithostatic pressure (and the Poisson coefficient for this report may become a least-known parameter). Indeed, other sources may have an impact on the applied pressure, such as a higher altitude or denser material near the boundary. In those cases, however, creeping flow restoration could also be a useful tool to analyse the unknown parameters. The conditions that best balance the models could then be found, for example as the solution of an inverse problem on the restoration results.

Bibliography

M. M. Al-Fahmi, A. Plesch, J. H. Shaw, and J. C. Cole. Restorations of faulted domes. *AAPG Bulletin*, 100(2): 151–163, 2016. ISSN 0149-1423. doi: 10.1306/08171514211. (Cited p. xiii, 13)

P. A. Allen and J. R. Allen. *Basin analysis: Principles and application to petroleum play assessment*. John Wiley & Sons, 2013. (Cited p. xii, 10)

M. S. Alnæs, J. Blechta, J. Hake, A. Johansson, B. Kehlet, A. Logg, C. Richardson, J. Ring, M. E. Rognes, and G. N. Wells. The fenics project version 1.5. *Archive of Numerical Software*, 3(100), 2015. doi: 10.11588/ans.2015.100.20553. (Cited p. 34)

P. Anquez, J. Pellerin, and G. Caumon. 3D Geological Surface Model Repair: Application to Restored Models. In *RINGMeeting*, 2016. (Cited p. 15)

D. Arndt, W. Bangerth, T. C. Clevenger, D. Davydov, M. Fehling, D. Garcia-Sanchez, G. Harper, T. Heister, L. Heltai, M. Kronbichler, R. M. Kynch, M. Maier, J.-P. Pelteret, B. Turcksin, and D. Wells. The `deal.II` library, version 9.1. *Journal of Numerical Mathematics*, 2019. doi: 10.1515/jnma-2019-0064. (Cited p. xvi, 26, 34)

D. Arndt, W. Bangerth, D. Davydov, T. Heister, L. Heltai, M. Kronbichler, M. Maier, J.-P. Pelteret, B. Turcksin, and D. Wells. The deal. ii finite element library: Design, features, and insights. *Computers & Mathematics with Applications*, 2020. ISSN 0898-1221. doi: 10.1016/j.camwa.2020.02.022. (Cited p. xvi, 34)

A. Asgari and L. Moresi. Multiscale Particle-In-Cell Method: From Fluid to Solid Mechanics. In *Advanced Methods for Practical Applications in Fluid Mechanics*, chapter 9. IntechOpen, Rijeka, 2012. doi: 10.5772/26419. (Cited p. xv, 24, 34)

L. F. Athy. Density, porosity, and compaction of sedimentary rocks. *AAPG Bulletin*, 14(1): 1–24, 1930. ISSN 0149-1423. doi: 10.1306/3D93289E-16B1-11D7-8645000102C1865D. (Cited p. 10)

W. Bangerth, R. Hartmann, and G. Kanschat. deal.II – a general purpose object oriented finite element library. *ACM Trans. Math. Softw.*, 33(4): 24/1–24/27, 2007. doi: 10.1145/1268776.1268779. (Cited p. xvi, 26, 34)

W. Bangerth, J. Dannberg, R. Gassmoeller, T. Heister, et al. ASPECT v2.1.0 [software], 2019. (Cited p. 23, 31, 34)

A. Bouziat, N. Guy, J. Frey, D. Colombo, P. Colin, M.-C. Cacas-Stentz, and T. Cornu. An assessment of stress states in passive margin sediments: Iterative

hydro-mechanical simulations on basin models and implications for rock failure predictions. *Geosciences*, 9(11): 469, 2019. doi: 10.3390/geosciences9110469. (Cited p. 11)

S. E. Boyer and D. Elliott. Thrust Systems1. *AAPG Bulletin*, 66(9): 1196–1230, 1982. ISSN 0149-1423. doi: 10.1306/03B5A77D-16D1-11D7-8645000102C1865D. (Cited p. 2)

J. Braun. Pecube: A new finite-element code to solve the 3D heat transport equation including the effects of a time-varying, finite amplitude surface topography. *Computers & Geosciences*, 29(6): 787–794, 2003. doi: 10.1016/S0098-3004(03)00052-9. (Cited p. 23)

J. Braun and M. Sambridge. Dynamical Lagrangian Remeshing (DLR): A new algorithm for solving large strain deformation problems and its application to fault-propagation folding. *Earth and Planetary Science Letters*, 124(1): 211–220, 1994. ISSN 0012-821X. doi: 10.1016/0012-821X(94)00093-X. (Cited p. 22)

J. Braun and M. Sambridge. A numerical method for solving partial differential equations on highly irregular evolving grids. *Nature*, 376(6542): 655–660, 1995. ISSN 1476-4687. doi: 10.1038/376655a0. (Cited p. 22)

J. Braun and P. Yamato. Structural evolution of a three-dimensional, finite-width crustal wedge. *Tectonophysics*, 484(1): 181–192, 2010. ISSN 0040-1951. doi: 10.1016/j.tecto.2009.08.032. (Cited p. 23)

J. Braun, C. Thieulot, P. Fullsack, M. DeKool, C. Beaumont, and R. Huismans. DOUAR: A new three-dimensional creeping flow numerical model for the solution of geological problems. *Physics of the Earth and Planetary Interiors*, 171(1): 76–91, 2008. ISSN 0031-9201. doi: 10.1016/j.pepi.2008.05.003. (Cited p. 22, 23)

J. Brown, L. L. Pourhiet, D. A. May, and P. Sanan. pTatin3D [software], 2018. (Cited p. 34)

J.-P. Brun and X. Fort. Salt tectonics at passive margins: Geology versus models. *Marine and Petroleum Geology*, 28(6): 1123 – 1145, 2011. ISSN 0264-8172. doi: 10.1016/j.marpetgeo.2011.03.004. (Cited p. 63, 98)

R. T. Chamberlin. The Appalachian folds of central Pennsylvania. *The Journal of Geology*, 18(3): 228–251, 1910. doi: 10.1086/621722. (Cited p. xii, 2, 11)

B. Chauvin. *Applicability of the mechanics-based restoration: boundary conditions, fault network and comparison with a geometrical method.* PhD thesis, Université de Lorraine, 2017. (Cited p. 5, 10, 11, 14, 78)

B. P. Chauvin, P. J. Lovely, J. M. Stockmeyer, A. Plesch, G. Caumon, and J. H. Shaw. Validating novel boundary conditions for three-dimensional mechanics-based restoration: An extensional sandbox model example. *AAPG Bulletin*, 102(2): 245–266, 2018. ISSN 0149-1423. doi: 10.1306/0504171620817154. (Cited p. 3, 13, 60)

U. R. Christensen and A. W. Hofmann. Segregation of subducted oceanic crust in the convecting mantle. *Journal of Geophysical Research: Solid Earth*, 99(B10): 19867–19884, 1994. doi: 10.1029/93JB03403. (Cited p. 24)

N. Clausolles. *Stochastic seismic interpretation of salt bodies: detection, sampling and impact on seismic imaging*. PhD thesis, Université de Lorraine, 2020. (Cited p. 4)

N. Clausolles, P. Collon, and G. Caumon. Generating variable shapes of salt geobodies from seismic images and prior geological knowledge. *Interpretation*, 7(4): T829–T841, 2019. doi: 10.1190/INT-2019-0032.1. (Cited p. xviii, 68, 69)

P. Cobbold, E. Rossello, and B. Vendeville. Some experiments on interacting sedimentation and deformation above salt horizons. *Bulletin de la Société Géologique de France*, (3): 453–460, 1989. (Cited p. 74)

P. R. Cobbold and M.-N. Percevault. Spatial integration of strains using finite elements. In *Strain Patterns in Rocks*, p. 299–305. Pergamon, 1983. doi: 10.1016/B978-0-08-030273-7.50010-0. (Cited p. 11)

F. H. Cornet. *Elements of crustal geomechanics*. Cambridge University Press, 2015. doi: 10.1017/CBO9781139034050. (Cited p. xiii, xv, 16, 21, 35)

R. Courant, K. Friedrichs, and H. Lewy. Über die partiellen differenzengleichungen der mathematischen physik. *Mathematische annalen*, 100(1): 32–74, 1928. doi: 10.1007/BF01448839. (Cited p. 18)

F. Crameri, H. Schmeling, G. Golabek, T. Duretz, R. Orendt, S. Buiter, D. May, B. Kaus, T. Gerya, and P. Tackley. A comparison of numerical surface topography calculations in geodynamic modelling: an evaluation of the 'sticky air' method. *Geophysical Journal International*, 189(1): 38–54, 2012. doi: 10.1111/j.1365-246X.2012.05388.x. (Cited p. 39, 45, 47)

P. Cupillard* and A. Botella. Homogenization of 3d geological models for seismic wave propagation. In *SEG Technical Program Expanded Abstracts 2015*, p. 3656–3660. Society of Exploration Geophysicists, 2015. (Cited p. 101)

C. Dahlstrom. Balanced cross sections. *Canadian Journal of Earth Sciences*, 6(4): 743–757, 1969. doi: 10.1139/e69-069. (Cited p. xii, 2, 11)

B. Daudré and S. Cloetingh. Numerical modelling of salt diapirism: influence of the tectonic regime. *Tectonophysics*, 240(1): 59–79, 1994. ISSN 0040-1951. doi: 10.1016/0040-1951(94)90264-X. (Cited p. 63, 101)

M. R. De Santi, J. L. E. Campos, and L. F. Martha. A Finite Element approach for geological section reconstruction. In *Proceedings of the 22th Gocad Meeting, Nancy, France*, p. 1–13, 2002. (Cited p. xiii, 13)

Y. Deubelbeiss and B. Kaus. Comparison of Eulerian and Lagrangian numerical techniques for the Stokes equations in the presence of strongly varying viscosity. *Physics of the Earth and Planetary Interiors*, 171(1-4): 92–111, 2008. doi: 10.1016/j.pepi.2008.06.023. (Cited p. 22, 26, 37, 40)

P. Dimakis, B. I. Braathen, J. I. Faleide, A. Elverhøi, and S. T. Gudlaugsson. Cenozoic erosion and the preglacial uplift of the Svalbard–Barents Sea region. *Tectonophysics*, 300(1-4): 311–327, 1998. doi: 10.1016/S0040-1951(98)00245-5. (Cited p. xii, 2, 10)

J. Donea, A. Huerta, J.-P. Ponthot, and A. Rodriguez-Ferran. Arbitrary lagrangian-eulerian methods, volume 1 of encyclopedia of computational mechanics, chapter 14. *John Wiley & Sons Ltd*, 3: 1–25, 2004. doi: 10.1002/9781119176817.ecm2009. (Cited p. 28, 35, 37)

P. Durand-Riard. *Gestion de la complexité géologique en restauration géomécanique 3D*. PhD thesis, Vandoeuvre-les-Nancy, INPL, 2010. (Cited p. xiii, 5, 13)

P. Durand-Riard, G. Caumon, and P. Muron. Balanced restoration of geological volumes with relaxed meshing constraints. *Computers & Geosciences*, 36(4): 441–452, 2010. doi: 10.1016/j.cageo.2009.07.007. (Cited p. 13, 15)

P. Durand-Riard, L. Salles, M. Ford, G. Caumon, and J. Pellerin. Understanding the evolution of syn-depositional folds: Coupling decompaction and 3d sequential restoration. *Marine and Petroleum Geology*, 28(8): 1530–1539, 2011. doi: 10.1016/j.marpetgeo.2011.04.001. (Cited p. xii, 10)

P. Durand-Riard, C. Guzofski, G. Caumon, and M.-O. Titeux. Handling natural complexity in three-dimensional geomechanical restoration, with application to the recent evolution of the outer fold and thrust belt, deep-water niger delta. *AAPG bulletin*, 97(1): 87–102, 2013a. doi: 10.1306/06121211136. (Cited p. 14)

P. Durand-Riard, J. H. Shaw, A. Plesch, and G. Lufadeju. Enabling 3D geomechanical restoration of strike-and oblique-slip faults using geological constraints, with applications to the deep-water Niger Delta. *Journal of Structural Geology*, 48: 33–44, 2013b. doi: 10.1016/j.jsg.2012.12.009. (Cited p. 3, 13, 14)

T. Duretz, R. de Borst, and L. Le Pourhiet. Finite thickness of shear bands in frictional viscoplasticity and implications for lithosphere dynamics. *Geochemistry, Geophysics, Geosystems*, 20(11): 5598–5616, 2019. doi: 10.1029/2019GC008531. (Cited p. 101)

J.-L. Epard and J. Groshong, Richard H. Excess Area and Depth to Detachment1. *AAPG Bulletin*, 77(8): 1291–1302, 1993. ISSN 0149-1423. doi: 10.1306/BDFF8E66-1718-11D7-8645000102C1865D. (Cited p. 2)

N. Fernandez. *2D and 3D numerical modelling of multilayer detachment folding and salt tectonics*. PhD thesis, Mainz University, 2014. (Cited p. 4, 19, 21)

C. Fillon, R. S. Huismans, and P. van der Beek. Syntectonic sedimentation effects on the growth of fold-and-thrust belts. *Geology*, 41(1): 83–86, 2013. ISSN 1943-2682, 0091-7613. doi: 10.1130/G33531.1. (Cited p. 23)

R. C. Fletcher and D. D. Pollard. Can we understand structural and tectonic processes and their products without appeal to a complete mechanics? *Journal of Structural Geology*, 21(8-9): 1071–1088, 1999. doi: 10.1016/S0191-8141(99)00056-5. (Cited p. xiii, 13)

S. Fomel and E. Landa. Structural uncertainty of time-migrated seismic images. *Journal of Applied Geophysics*, 101: 27 – 30, 2014. ISSN 0926-9851. doi: 10.1016/j.jappgeo.2013.11.010. (Cited p. 1)

H. Fossen. *Structural geology*. Cambridge University Press, second edition, 2016. (Cited p. 1, 4, 11)

P. Fullsack. An arbitrary Lagrangian-Eulerian formulation for creeping flows and its application in tectonic models. *Geophysical Journal International*, 120(1): 1–23, 1995. doi: 10.1111/j.1365-246X.1995.tb05908.x. (Cited p. xiv, xv, 23, 35)

R. Gassmöller, H. Lokavarapu, E. Heien, E. G. Puckett, and W. Bangerth. Flexible and scalable particle-in-cell methods with adaptive mesh refinement for geodynamic computations. *Geochemistry, Geophysics, Geosystems*, 19(9): 3596–3604, 2018. doi: 10.1029/2018GC007508. (Cited p. xv, 24, 25, 34, 100)

R. Gassmöller, H. Lokavarapu, W. Bangerth, and E. G. Puckett. Evaluating the accuracy of hybrid finite element/particle-in-cell methods for modelling incompressible stokes flow. *Geophysical Journal International*, 219(3): 1915–1938, 2019. doi: 10.1093/gji/ggz405. (Cited p. 34)

L. Gemmer, S. J. Ings, S. Medvedev, and C. Beaumont. Salt tectonics driven by differential sediment loading: stability analysis and finite-element experiments. *Basin Research*, 16(2): 199–218, 2004. ISSN 1365-2117. doi: 10.1111/j.1365-2117.2004.00229.x. (Cited p. 23)

M. Gerbault, A. N. Poliakov, and M. Daignieres. Prediction of faulting from the theories of elasticity and plasticity: what are the limits? *Journal of Structural Geology*, 20 (2-3): 301–320, 1998. doi: 10.1016/S0191-8141(97)00089-8. (Cited p. 14)

T. Gerya. *Introduction to numerical geodynamic modelling*. Cambridge University Press, 2019. doi: 10.1017/9781316534243. (Cited p. 43, 44)

K. A. Giles and T. F. Lawton. Attributes and evolution of an exhumed salt weld, la popa basin, northeastern mexico. *Geology*, 27(4): 323–326, 1999. doi: 10.1130/0091-7613(1999)027<0323:AAEOAE>2.3.CO;2. (Cited p. 69)

J.-P. Gratier. *L'équilibrage des coupes géologiques. Buts, méthodes et applications*. Géosciences-Rennes, 1988. (Cited p. xii, 2, 11)

J.-P. Gratier and B. Guillier. Compatibility constraints on folded and faulted strata and calculation of total displacement using computational restoration (unfold program). *Journal of Structural Geology*, 15(3): 391 – 402, 1993. ISSN 0191-8141. doi: 10.1016/0191-8141(93)90135-W. (Cited p. 3)

J.-P. Gratier, B. Guillier, A. Delorme, and F. Odonne. Restoration and balance of a folded and faulted surface by best-fitting of finite elements: Principle and applications. *Journal of Structural Geology*, 13(1): 111–115, 1991. doi: 10.1016/0191-8141(91)90107-T. (Cited p. 11)

R. Groshong. *3-D structural geology*. Springer, Berlin, Heidelberg, 2006. doi: 10.1007/978-3-540-31055-6. (Cited p. 1, 11)

C. A. Guzofski, J. P. Mueller, J. H. Shaw, P. Muron, D. A. Medwedeff, F. Bilotti, and C. Rivero. Insights into the mechanisms of fault-related folding provided by volumetric structural restorations using spatially varying mechanical constraints. *AAPG bulletin*, 93(4): 479–502, 2009. doi: 10.1306/11250807130. (Cited p. xiii, 13, 15)

J. Hall. Ii. on the vertical position and convolutions of certain strata, and their relation with granite. *Transactions of the Royal Society of Edinburgh*, 7(1): 79–108, 1815. doi: 10.1017/S0080456800019268. (Cited p. 74)

P. Hatcher, E. Spiker, N. Szeverenyi, and G. Maciel. Selective preservation and origin of petroleum-forming aquatic kerogen. *Nature*, 305: 498–501, 1983. doi: 10.1038/305498a0. (Cited p. 2)

T. Heister, J. Dannberg, R. Gassmöller, and W. Bangerth. High accuracy mantle convection simulation through modern numerical methods–ii: realistic models and problems. *Geophysical Journal International*, 210(2): 833–851, 2017. doi: 10.1093/gji/ggx195. (Cited p. 26, 37)

M. R. Hudec and M. P. Jackson. Terra infirma: Understanding salt tectonics. *Earth-Science Reviews*, 82(1-2): 1–28, 2007. doi: 10.1016/j.earscirev.2007.01.001. (Cited p. 16, 70)

T. J. Hughes. *The finite element method: linear static and dynamic finite element analysis*. Dover Publications, inc., Mineola, New York, 2012. (Cited p. xv, 26)

T. J. Hughes, W. K. Liu, and T. K. Zimmermann. Lagrangian-Eulerian finite element formulation for incompressible viscous flows. *Computer methods in applied mechanics and engineering*, 29(3): 329–349, 1981. doi: 10.1016/0045-7825(81)90049-9. (Cited p. xv, 23)

T. J. Hughes, L. P. Franca, and M. Balestra. A new finite element formulation for computational fluid dynamics: V. circumventing the babuška-brezzi condition: a stable petrov-galerkin formulation of the stokes problem accommodating equal-order interpolations. *Computer Methods in Applied Mechanics and Engineering*, 59(1): 85 – 99, 1986. ISSN 0045-7825. doi: 10.1016/0045-7825(86)90025-3. (Cited p. 28)

IFP and C. & . C. Reservoirs. Principles of digital structural analog modeling. Technical report, 2006. (Cited p. 76, 101)

A. Ismail-Zadeh and P. Tackley. *Computational methods for geodynamics*. Cambridge University Press, 2010. doi: 10.1017/CBO9780511780820. (Cited p. 18)

A. Ismail-Zadeh, B. Naimark, and C. Talbot. Reconstruction of the history of the movement of layered geostructures: Inverse problem of gravitational stability. *Comput. Seism. Geodyn*, 6: 27, 2004a. doi: 10.1002/9781118669853.ch4. (Cited p. 18)

A. Ismail-Zadeh, G. Schubert, I. Tsepelev, and A. Korotkii. Inverse problem of thermal convection: numerical approach and application to mantle plume restoration. *Physics of the Earth and Planetary Interiors*, 145(1-4): 99–114, 2004b. doi: 10.1016/j.pepi.2004.03.006. (Cited p. 4, 19)

A. Ismail-Zadeh, I. Tsepelev, C. Talbot, and A. Korotkii. Three-dimensional forward and backward modelling of diapirism: numerical approach and its applicability to the evolution of salt structures in the pricaspian basin. *Tectonophysics*, 387(1-4): 81–103, 2004c. doi: 10.1016/j.tecto.2004.06.006. (Cited p. 19, 23)

A. Ismail-Zadeh, A. Korotkii, and I. Tsepelev. Data-driven numerical modelling in geodynamics and tectonophysics. In , p. 216–221, 2016. (Cited p. 19)

A. T. Ismail-Zadeh, C. J. Talbot, and Y. A. Volozh. Dynamic restoration of profiles across diapiric salt structures: numerical approach and its applications. *Tectonophysics*, 337(1-2): 23–38, 2001. doi: 10.1016/S0040-1951(01)00111-1. (Cited p. xiv, xvii, 4, 19, 20, 22, 57)

M. P. Jackson and M. R. Hudec. *Salt tectonics: Principles and practice*. Cambridge University Press, 2017. (Cited p. 18)

P. Jenny, S. Pope, M. Muradoglu, and D. Caughey. A hybrid algorithm for the joint pdf equation of turbulent reactive flows. *Journal of Computational Physics*, 166(2): 218 – 252, 2001. ISSN 0021-9991. doi: 10.1006/jcph.2000.6646. (Cited p. 38)

B. J. Kaus. Factors that control the angle of shear bands in geodynamic numerical models of brittle deformation. *Tectonophysics*, 484(1): 36–47, 2010. ISSN 0040-1951. doi: 10.1016/j.tecto.2009.08.042. (Cited p. 101)

B. J. Kaus and Y. Y. Podladchikov. Forward and reverse modeling of the three-dimensional viscous rayleigh-taylor instability. *Geophysical Research Letters*, 28(6): 1095–1098, 2001. doi: 10.1029/2000GL011789. (Cited p. 4, 19)

B. J. Kaus, H. Mühlhaus, and D. A. May. A stabilization algorithm for geodynamic numerical simulations with a free surface. *Physics of the Earth and Planetary Interiors*, 181(1-2): 12–20, 2010. doi: 10.1016/j.pepi.2010.04.007. (Cited p. xvi, 40, 47, 48)

T. Kocher and N. S. Mancktelow. Dynamic reverse modelling of flanking structures: a source of quantitative kinematic information. *Journal of Structural Geology*, 27(8): 1346–1354, 2005. doi: 10.1016/j.jsg.2005.05.007. (Cited p. 19)

A. I. Korotkii and I. Tsepelev. Direct and inverse problems of high-viscosity fluid dynamics. *Automation and Remote Control*, 68(5): 822–833, 2007. doi: 10.1134/S0005117907050098. (Cited p. 19)

M. Kronbichler, T. Heister, and W. Bangerth. High accuracy mantle convection simulation through modern numerical methods. *Geophysical Journal International*, 191 (1): 12–29, 2012. doi: 10.1111/j.1365-246X.2012.05609.x. (Cited p. 29, 38, 71)

O. A. Ladyzhenskaya. *The mathematical theory of viscous incompressible flow*, vol. 2. Gordon and Breach New York, 1969. (Cited p. 28)

P. Landais, R. Michels, and M. Elie. Are time and temperature the only constraints to the simulation of organic matter maturation? *Organic Geochemistry*, 22(3): 617 – 630, 1994. ISSN 0146-6380. doi: 10.1016/0146-6380(94)90128-7. (Cited p. 2)

S. M. Lechmann, S. M. Schmalholz, J.-P. Burg, and F. Marques. Dynamic unfolding of multilayers: 2d numerical approach and application to turbidites in sw portugal. *Tectonophysics*, 494(1-2): 64–74, 2010. doi: 10.1016/j.tecto.2010.08.009. (Cited p. 19, 71)

Q. Liao and D. Silvester. Robust stabilized Stokes approximation methods for highly stretched grids. *IMA Journal of Numerical Analysis*, 33(2): 413–431, 2012. ISSN 0272-4979. doi: 10.1093/imanum/drs012. (Cited p. 29)

W. K. Liu, E. Karpov, S. Zhang, and H. Park. An introduction to computational nanomechanics and materials. *Computer methods in applied mechanics and engineering*, 193(17-20): 1529–1578, 2004. doi: 10.1016/j.cma.2003.12.008. (Cited p. 25)

P. Lovely, E. Flodin, C. Guzofski, F. Maerten, and D. D. Pollard. Pitfalls among the promises of mechanics-based restoration: Addressing implications of unphysical boundary conditions. *Journal of Structural Geology*, 41: 47–63, 2012. doi: 10.1016/j.jsg.2012.02.020. (Cited p. 13, 14, 71)

P. J. Lovely, S. N. Jayr, and D. A. Medwedeff. Practical and efficient three-dimensional structural restoration using an adaptation of the GeoChron model. *AAPG Bulletin*, 102(10): 1985–2016, 2018. doi: 10.1306/03291817191. (Cited p. 3, 11)

F. Maerten and L. Maerten. Unfolding and Restoring Complex Geological Structures Using Linear Elasticity Theory. In *AGU Fall Meeting Abstracts*, vol. 2001, p. T22C–0940, 2001. (Cited p. xiii, 2, 3, 13)

L. Maerten and F. Maerten. Chronologic modeling of faulted and fractured reservoirs using geomechanically based restoration: Technique and industry applications. *AAPG bulletin*, 90(8): 1201–1226, 2006. doi: 10.1306/02240605116. (Cited p. xiii, 13, 15)

J.-L. Mallet. Discrete smooth interpolation. *ACM Transactions on Graphics (TOG)*, 8 (2): 121–144, 1989. doi: 10.1145/62054.62057. (Cited p. 11)

J.-L. Mallet. Discrete smooth interpolation in geometric modelling. *Computer-aided design*, 24(4): 178–191, 1992. doi: 10.1016/0010-4485(92)90054-E. (Cited p. 11)

J.-L. Mallet. Discrete modeling for natural objects. *Mathematical geology*, 29(2): 199–219, 1997. doi: 10.1007/BF02769628. (Cited p. 11)

J.-L. Mallet. *Geomodeling*. Oxford University Press, 2002. (Cited p. 3)

J.-L. Mallet. Space–time mathematical framework for sedimentary geology. *Mathematical geology*, 36(1): 1–32, 2004. doi: 10.1023/B:MATG.0000016228.75495.7c. (Cited p. 11)

J. Mansour, J. Giordani, L. Moresi, R. Beucher, O. Kaluza, M. Velic, R. Farrington, S. Quenette, and A. Beall. Underworld2 [software], 2020. (Cited p. 34)

P. Massimi, A. Quarteroni, and G. Scrofani. An adaptive finite element method for modeling salt diapirism. *Mathematical Models and Methods in Applied Sciences*, 16 (04): 587–614, 2006. doi: 10.1142/S0218202506001273. (Cited p. xiii, 2, 16, 22, 71)

P. Massimi, A. Quarteroni, F. Saleri, and G. Scrofani. Modeling of salt tectonics. *Computer methods in applied mechanics and engineering*, 197(1): 281–293, 2007. doi: 10.1016/j.cma.2007.08.004. (Cited p. 23)

J. Massot. *Implémentation de méthodes de restauration équilibrée 3D*. PhD thesis, Institut National Polytechnique de Lorraine, 2002. (Cited p. 11)

D. A. May, J. Brown, and L. Le Pourhiet. pTatin3D: High-performance methods for long-term lithospheric dynamics. In *High Performance Computing, Networking, Storage and Analysis, SC14: International Conference for*, p. 274–284, 2014. (Cited p. xiii, 16, 34)

D. A. May, J. Brown, and L. Le Pourhiet. A scalable, matrix-free multigrid preconditioner for finite element discretizations of heterogeneous Stokes flow. *Computer Methods in Applied Mechanics and Engineering*, 290: 496–523, 2015. doi: 10.1016/j.cma.2015.03.014. (Cited p. xiii, 16)

A. Mazuyer. *Estimation de l'état de contrainte initial in situ dans les réservoirs par approche inverse*. Theses, Université de Lorraine, 2018. (Cited p. 5)

D. A. Medwedeff and J. Suppe. Multibend fault-bend folding. *Journal of Structural Geology*, 19(3): 279 – 292, 1997. ISSN 0191-8141. doi: 10.1016/S0191-8141(97)83026-X. (Cited p. 2)

D. A. Medwedeff, S. N. Jayr, and P. J. Lovely. Practical and Efficient Three Dimensional Structural Restoration Using "Geological Knowledge-Oriented" Earth Models. In *AAPG Annual Convention and Exhibition*, 2016. (Cited p. 2, 11)

U. T. Mello and M. E. Henderson. Techniques for including large deformations associated with salt and fault motion in basin modeling. *Marine and Petroleum Geology*, 14(5): 551–564, 1997. doi: 10.1016/S0264-8172(97)00015-9. (Cited p. 22)

U. T. Mello, G. D. Karner, and R. N. Anderson. Role of salt in restraining the maturation of subsalt source rocks. *Marine and Petroleum Geology*, 12(7): 697–716, 1995. doi: 10.1016/0264-8172(95)93596-V. (Cited p. 2)

D. W. Meyer and P. Jenny. Conservative velocity interpolation for pdf methods. *Proceedings in Applied Mathematics and Mechanics*, 4(1): 466–467, 2004. doi: 10.1002/pamm.200410214. (Cited p. 38)

L. Moresi, F. Dufour, and H.-B. Mühlhaus. A Lagrangian integration point finite element method for large deformation modeling of viscoelastic geomaterials. *Journal of Computational Physics*, 184(2): 476–497, 2003. doi: 10.1016/S0021-9991(02)00031-1. (Cited p. 24, 31, 32, 34)

I. Moretti. Working in complex areas: New restoration workflow based on quality control, 2d and 3d restorations. *Marine and Petroleum Geology*, 25(3): 205–218, 2008. doi: 10.1016/j.marpetgeo.2007.07.001. (Cited p. xiii)

I. Moretti and C. Froidevaux. Thermomechanical models of active rifting. *Tectonics*, 5 (4): 501–511, 1986. ISSN 1944-9194. doi: 10.1029/TC005i004p00501. (Cited p. xiii, 16)

I. Moretti, F. Lepage, and M. Guiton. KINE3D: a new 3D restoration method based on a mixed approach linking geometry and geomechanics. *Oil & Gas Science and Technology*, 61(2): 277–289, 2006. doi: 10.2516/ogst:2006021. (Cited p. xiii, 3, 13)

R. Moyen. *Paramétrisation 3D de l'espace en Géologie sédimentaire: Le modèle Geochron*. PhD thesis, Atelier national de reproduction des thèses, 2005. (Cited p. 11)

P. Muron. *Méthodes numériques 3-D de restauration des structures géologiques faillées*. PhD thesis, INPL, 2005. (Cited p. xiii, 3, 5, 11, 13, 15, 78)

T. Nalpas and J.-P. Brun. Salt flow and diapirism related to extension at crustal scale. *Tectonophysics*, 228(3-4): 349–362, 1993. doi: 10.1016/0040-1951(93)90348-N. (Cited p. xiii, 16)

L. L. Nettleton. Fluid mechanics of salt domes. *AAPG Bulletin*, 18(9): 1175–1204, 1934. doi: 10.1306/3D932C74-16B1-11D7-8645000102C1865D. (Cited p. 18)

M. N. Parquer, P. Collon, and G. Caumon. Reconstruction of Channelized Systems Through a Conditioned Reverse Migration Method. *Mathematical Geosciences*, 49 (8): 965–994, 2017. doi: 10.1007/s11004-017-9700-3. (Cited p. xii, 10)

J. Pellerin, B. Lévy, G. Caumon, and A. Botella. Automatic surface remeshing of 3D structural models at specified resolution: A method based on Voronoi diagrams. *Computers & Geosciences*, 62: 103–116, 2014. doi: 10.1016/j.cageo.2013.09.008. (Cited p. 15)

Y. Podladchikov, C. Talbot, and A. Poliakov. Numerical models of complex diapirs. *Tectonophysics*, 228(3-4): 189–198, 1993. doi: 10.1016/0040-1951(93)90340-P. (Cited p. 18, 22)

A. N. Poliakov, Y. Y. Podladchikov, E. C. Dawson, and C. J. Talbot. Salt diapirism with simultaneous brittle faulting and viscous flow. *Geological Society, London, Special Publications*, 100(1): 291–302, 1996. doi: 10.1144/GSL.SP.1996.100.01.19. (Cited p. 18, 23, 31)

A. Popov, B. Kaus, T. Baumann, G. Reuber, A. Puesoek, N. Fernandez, A. Bauville, A. Piccolo, B. Montesinos, M. Kottwitz, and A. Spang. LaMEM [software], 2020. (Cited p. 34)

J. Qin and S. Zhang. On the selective local stabilization of the mixed q1–p0 element. *International Journal for Numerical Methods in Fluids*, 55(12): 1121–1141, 2007. doi: 10.1002/fld.1505. (Cited p. 29)

M. E. Quinquis, S. J. Buiter, and S. Ellis. The role of boundary conditions in numerical models of subduction zone dynamics. *Tectonophysics*, 497: 57–70, 2011. doi: 10.1016/j.tecto.2010.11.001. (Cited p. 40)

H. Ramberg. Instability of layered systems in the field of gravity. *Physics of the Earth and Planetary Interiors*, 1(7): 427–447, 1968. doi: 10.1016/0031-9201(68)90014-9. (Cited p. 40)

H. Ramberg. *Gravity, deformation and the earth's crust: in theory, experiments and geological application.* London ; New York : Academic Press, 2d ed edition, 1981. ISBN 978-0-12-576860-3. (Cited p. 45, 74)

M. J. Ramón, E. L. Pueyo, G. Caumon, and J. L. Briz. Parametric unfolding of flexural folds using palaeomagnetic vectors. *Geological Society, London, Special Publications*, 425(1): 247–258, 2016. doi: 10.1144/SP425.6. (Cited p. 11)

J. Renaudeau, M. Irakarama, G. Laurent, F. Maerten, and G. CAUMON. Implicit modelling of geological structures: A cartesian grid method handling discontinuities with ghost points. *WIT Transactions on Engineering Sciences*, 122: 189–199, 2019. doi: 10.2495/be410171. (Cited p. 24, 25)

D. Rouby. *Restauration en carte des domaines faillés en extension. Méthode et applications.* PhD thesis, Université Rennes 1, 1994. (Cited p. xii, 2, 11)

M. G. Rowan, T. F. Lawton, and K. A. Giles. Anatomy of an exposed vertical salt weld and flanking strata, la popa basin, mexico. *Geological Society, London, Special Publications*, 363(1): 33–57, 2012. doi: 10.1144/SP363.3. (Cited p. 70)

L. Royden and C. Keen. Rifting process and thermal evolution of the continental margin of eastern Canada determined from subsidence curves. *Earth and Planetary Science Letters*, 51(2): 343–361, 1980. doi: 10.1016/0012-821X(80)90216-2. (Cited p. xii, 10)

H. Sato, M. C. Fehler, and T. Maeda. *Seismic wave propagation and scattering in the heterogeneous earth.* Springer Science & Business Media, 2012. (Cited p. 1)

S. M. Schmalholz. 3d numerical modeling of forward folding and reverse unfolding of a viscous single-layer: Implications for the formation of folds and fold patterns. *Tectonophysics*, 446(1-4): 31–41, 2008. doi: 10.1016/j.tecto.2007.09.005. (Cited p. 19)

M. Schuh-Senlis, C. Thieulot, P. Cupillard, and G. Caumon. Towards the application of stokes flow equations to structural restoration simulations. *Solid Earth*, 11(5): 1909–1930, 2020. doi: 10.5194/se-11-1909-2020. (Cited p. 40, 54)

D. Silvester and N. Kechkar. Stabilised bilinear-constant velocity-pressure finite elements for the conjugate gradient solution of the stokes problem. *Computer Methods in Applied Mechanics and Engineering*, 79(1): 71 – 86, 1990. ISSN 0045-7825. doi: 10.1016/0045-7825(90)90095-4. (Cited p. 29)

J. M. Stockmeyer and C. Guzofski. Interplay between extension, salt and pre-existing structure, offshore angola. In *AAPG Annual Convention and Exhibition*, 2014. (Cited p. 78)

R. P. Suggate. Relations between depth of burial, vitrinite reflectance and geothermal gradient. *Journal of Petroleum Geology*, 21(1): 5–32, 1998. doi: 10.1111/j.1747-5457.1998.tb00644.x. (Cited p. 2)

D. Sulsky, Z. Chen, and H. L. Schreyer. A particle method for history-dependent materials. *Computer methods in applied mechanics and engineering*, 118(1-2): 179–196, 1994. doi: 10.1016/0045-7825(94)90112-0. (Cited p. 24)

J. Suppe. Geometry and kinematics of fault-bend folding. *American Journal of science*, 283(7): 684–721, 1983. (Cited p. 2)

P. Tang, C. Wang, and X. Dai. A majorized Newton-CG augmented Lagrangian-based finite element method for 3D restoration of geological models. *Computers & Geosciences*, 89: 200–206, 2016. doi: 10.1016/j.cageo.2016.01.013. (Cited p. xiii, 13)

M. Thielmann, D. May, and B. Kaus. Discretization errors in the hybrid finite element particle-in-cell method. *Pure and Applied Geophysics*, 171(9): 2165–2184, 2014. doi: 10.1007/s00024-014-0808-9. (Cited p. 26, 34, 37)

C. Thieulot. FANTOM: Two-and three-dimensional numerical modelling of creeping flows for the solution of geological problems. *Physics of the Earth and Planetary Interiors*, 188(1-2): 47–68, 2011. doi: 10.1016/j.pepi.2011.06.011. (Cited p. xiv, 23, 40, 43, 44)

C. Thieulot. Elefant: a user-friendly multipurpose geodynamics code. *Solid Earth Discussions*, 6: 1949–2096, 2014. doi: 10.5194/sed-6-1949-2014. (Cited p. 34)

C. Thieulot, P. Steer, and R. Huismans. Three-dimensional numerical simulations of crustal systems undergoing orogeny and subjected to surface processes. *Geochemistry, Geophysics, Geosystems*, 15(12): 4936–4957, 2014. doi: 10.1002/2014GC005490. (Cited p. 23, 25)

C. C. Thieulot. Fieldstone: The Finite Element Method in Computational Geodynamics. 2019. doi: 10.23644/uu.9209393.v1. (Cited p. 26, 29, 48)

S. Trim, J. Lowman, and S. Butler. Improving mass conservation with the tracer ratio method: application to thermochemical mantle flows. *Geochemistry, Geophysics, Geosystems*, 21(2): e2019GC008799, 2020. doi: 10.1029/2019GC008799. (Cited p. 34)

G. I. Tripp and J. R. Vearncombe. Fault/fracture density and mineralization: a contouring method for targeting in gold exploration. *Journal of Structural Geology*, 26 (6): 1087 – 1108, 2004. ISSN 0191-8141. doi: 10.1016/j.jsg.2003.11.002. (Cited p. 2)

P. van Keken, S. King, H. Schmeling, U. Christensen, D. Neumeister, and M.-P. Doin. A comparison of methods for the modeling of thermochemical convection. *Journal of Geophysical Research: Solid Earth*, 102(B10): 22477–22495, 1997. doi: 10.1029/97JB01353. (Cited p. iii, xv, 24, 55)

O. R. Walton and R. L. Braun. Viscosity, granular-temperature, and stress calculations for shearing assemblies of inelastic, frictional disks. *Journal of Rheology*, 30(5): 949–980, 1986. doi: 10.1122/1.549893. (Cited p. 101)

H. Wang, R. Agrusta, and J. van Hunen. Advantages of a conservative velocity interpolation (cvi) scheme for particle-in-cell methods with application in geodynamic modeling. *Geochemistry, Geophysics, Geosystems*, 16(6): 2015–2023, 2015. doi: 10.1002/2015GC005824. (Cited p. 38)

R. Weijermars, M. t. Jackson, and B. Vendeville. Rheological and tectonic modeling of salt provinces. *Tectonophysics*, 217(1-2): 143–174, 1993. doi: 10.1016/0040-1951(93)90208-2. (Cited p. xiv, 16)

S. Willett, C. Beaumont, and P. Fullsack. Mechanical model for the tectonics of doubly vergent compressional orogens. *Geology*, 21(4): 371–374, 1993. ISSN 0091-7613. doi: 10.1130/0091-7613(1993)021<0371:MMFTTO>2.3.CO;2. (Cited p. 23)

B. Willis. *The mechanics of Appalachian structure*, vol. 13. US Government Printing Office, 1894. (Cited p. 74)

W.-D. Woidt. Finite element calculations applied to salt dome analysis. *Tectonophysics*, 50(2-3): 369–386, 1978. doi: 10.1016/0040-1951(78)90143-9. (Cited p. 18, 24)

S. Zaleski and P. Julien. Numerical simulation of rayleigh-taylor instability for single and multiple salt diapirs. *Tectonophysics*, 206(1-2): 55–69, 1992. doi: 10.1016/0040-1951(92)90367-F. (Cited p. 18)

J. Zhou, F. Xu, T. Wang, A. Cao, and C. Yin. Cenozoic deformation history of the qaidam basin, nw china: Results from cross-section restoration and implications for qinghai–tibet plateau tectonics. *Earth and Planetary Science Letters*, 243(1-2): 195–210, 2006. doi: 10.1016/j.epsl.2005.11.033. (Cited p. 12)

Applicabilité des équations de Stokes pour la gestion des grandes déformations en restauration de modèles géologiques

Résumé : Afin d'étudier les roches du sous-sol, il est nécessaire de comprendre les déformations qu'elles ont subi depuis leur création. Les données disponibles n'étant souvent pas suffisantes pour déterminer de manière exacte ces déformations, les géologues font un certain nombre d'hypothèses par rapport à leurs connaissances et à des cas analogues. Celles-ci, en s'ajoutant aux données, permettent la création de modèles structuraux, somme des données et connaissances sur une zone. La restauration structurale a été développée pour essayer de faire remonter le temps à ces modèles géologiques. L'objectif est double: tout d'abord vérifier si le modèle structural permet la restauration vers un état géologique raisonnable, et donc limiter les incertitudes sur celui-ci. Ensuite, étudier la rétro-déformation des roches peut permettre d'en apprendre plus sur leur histoire (ainsi que vérifier les hypothèses faites sur celle-ci). Dans les contextes de bassins sédimentaires faillés, les méthodes de restauration utilisent des notions mécaniques pour calculer la déformation des roches, mais les conditions permettant d'appliquer un mouvement en temps inverse aux modèles étudiés sont encore principalement géométriques. Dans les contextes de bassins évaporitiques, une méthode de restauration a été développée en utilisant les équations de fluides visqueux, mais néglige le comportement des failles et les mouvements de la topographie.

La principale contribution de cette thèse est l'ajout de conditions plus physiques à la restauration de bassins sédimentaires faillés, et d'une méthode numérique pour l'appliquer. Cette méthode de restauration s'appuie sur des simulations mécaniques du sous-sol afin de calculer la rétro-déformation. Dans ces simulations, les roches sont considérées comme des fluides ayant une très grande viscosité, et la rétro-déformation s'appuie sur une advection du modèle en temps négatif. Les failles, elles, sont considérées comme des zones de cisaillement où les roches ont une viscosité plus faible. Cette méthode de restauration offre des résultats concluants sur des modèles simplifiés du sous-sol.

La seconde contribution de cette thèse est une évaluation de l'influence des différents paramètres de simulation sur le modèle restauré. Cette évaluation s'appuie sur la restauration d'un modèle analogique de laboratoire. Dans un premier temps, l'influence des conditions aux limites est étudiée, afin de déterminer les conditions les plus naturelles possibles permettant une restauration du modèle. Dans un second temps, l'influence des paramètres mécaniques à l'intérieur du modèle est étudiée, afin de déterminer les paramètres effectifs les plus proches de ceux des roches.

Ces contributions ouvrent une nouvelle perspective sur la manière d'introduire des conditions plus physiques dans la restauration mécanique du sous-sol.

Mots-clés : modèle structural, restauration structurale, restauration géomécanique, conditions aux limites, bassin sédimentaire

---

Using Stokes flow equations for the geomechanical restoration of geological structural models

Abstract: In order to study the subsurface, one must first understand its deformation through time. As the available data coverage is not sufficient to determine these deformations precisely, geologists make hypotheses to link them depending on their knowledge. This allows them to create structural models, which can be seen as the sum of all the data and knowledge on a specific area. Structural restoration was developped to try and make a model go back in time. The advantages are dual: first, it allows the validation of the structural model by checking if the restored model has a reasonable geometry. Second, the history and retro-deformation of the rock layers can be studied from the path they take during the restoration process (which also allows checking the hypotheses that were made on the history of the area). In the context of faulted and folded sedimentary basins, mechanics have been incorporated in the restoration process to compute the deformation of the rock layers inside the models, but the time reversal is still driven mainly by geometric conditions. In the context of basins incorporating salt tectonics, creeping flow restoration was developped by considering the rocks as highly viscous fluids, but neglects faults and non-flat topography.

The main contribution of this thesis is to provide an approach to add more physical conditions to the restoration of faulted sedimentary basins. This approach relies on mechanical simulations of the subsurface. The rock layers are treated as highly viscous fluids, and the restoration is driven by a negative time-step advection. The faults are considered as shear zones with an effective viscosity lower than the surrounding sediments. This methods allowed the restoration of several simplified models of the subsurface.

The second contribution of this thesis is an assessment of the choice of the parameters for the restoration simulations. This assessment is based on the restoration of a laboratory analogue model. The boundary conditions are first studied, to determine how to provide an adequate choice of conditions that still allow the restoration of the model. The material properties and their influence are then looked upon, to determine the effective parameters that are closest to those of the rocks inside the model.

These contributions offer a new perspective on how to add more physical conditions to the geomechanical restoration of structural models of the subsurface.

Keywords: structural model, structural restoration, geomechanical restoration, boundary conditions, sedimentary basins